State-resolved Reactivity and Bond-selective Control of Methane Dissociation on Ni(111)

A dissertation

submitted by

Nan Chen

In partial fulfillment of the requirements for the degree of

Doctor of Philosophy

in

Chemistry

Tufts University

February 2013

© 2013, Nan Chen

Advisor: Dr. Arthur L. Utz

State-resolved Reactivity and Bond-selective Control of Methane Dissociation on Ni(111)

By

Nan Chen

Submitted to Department of Chemistry on January 25th, 2013 in partial fulfillment of the requirements for the degree of Doctor of Philosophy in Chemistry

ABSTRACT

State-resolved reactivity is particularly useful to uncover the energy flow details in gas-surface reactions. Here, we combine supersonic molecular beam techniques and laser excitation to characterize the mode- and bond-specific reactivity of methane on a Ni(111) surface. Our results reveal important details about the effect of vibrational mode and symmetry on the reactivity of this benchmark gas-surface reaction.

We first introduce a theoretical model of the state-resolved reactivity of methane on a Ni(111) surface. This model provides a theoretical approach to understanding the reactivity of selected vibrational states. More importantly, it can provide an accurate

approach to measure the reactivity of methane in vibrational ground state. This approach relies on a detailed knowledge of the vibrational structure of methane, its vibrational cooling dynamics in a supersonic expansion, and understanding of how individual vibrational states contribute to the overall reactivity.

In Chapter IV, we introduce a new scheme to measure the state-resolved reactivity based on the 'King and Wells' method. With the new detection scheme, we are able to measure reactivity with and without laser excitation simultaneously. In addition, we are able to probe real-time reactivity during the reaction. This method will not only largely reduce the experimental time, but also extend our measurements of state-resolved reactivity to a wider range, which is impossible to measure by post-dose methods.

In Chapter V, we explore the state-resolved reactivity of CH_4 prepared in a combined bending state ($\nu_2 + \nu_4$) on Ni(111). Our results provide the first comparison between a bend and stretch vibrational state in the same polyad. By this comparison, we confirm the trend that stretching vibrations have better efficiency in promoting reactivity than bending vibrations. In addition, comparing with the $3\nu_4$ state, we provide experimental evidence supporting the theoretical calculation that the ν_2 bend state is less efficient than the ν_4 bend state in promoting CH_4 activation on Ni(111).

In the last chapter, we explore the bond- and mode-selectivity of CH_2D_2 dissociation

on Ni(111). Unlike CH_4 on Ni(100), our results show that different C-H vibrations bring almost identical enhancement to the overall reactivity of CH_2D_2 on Ni(111). Through comparisons, we also find surface temperature is more important in a energy-starving region than vibrational modes or symmetries in promoting CH_2D_2 activation. In addition, we compare our results with the overtone stretching excitation of CH_2D_2 in gas-phase and gas-surface reactions. The results show that ν_1 and ν_6 C-H vibrations are less localized than their overtone states in CH_2D_2 molecules. Our results further uncover details of the role that vibrations play in the bond-selective dissociation of CH_2D_2 on Ni(111).

ACKNOWLEDGEMENTS

Many times in the past, I had thought about what I should write in this acknowledgement since there are so many unforgettable things happened during the past years. But I am certain none of these works would be possible if I do not have the supports from people around me.

My parents and grandparents have been my greatest source of supports since I was born. They never gave up on me and were always there to give me help without hesitating. Leaving homeland and studying aboard is a big challenge. But everything becomes a fortune since I had met my wife, Wenwen, who gave me her love and sacrifice in supporting me during the past years. As well, I have to thank my son Alex for providing me the great motivation to pass through the last barriers toward the Ph.D. degree.

The person who helped me most in the past seven years is my advisor, Arthur L. Utz. Art is one of the smartest people I have ever met, and he is so knowledgeable on many subjects. He is always nice to people and willing to share what he know. No matter how bad it seemed, he was always able to help me out through tough times on my path.

This document would not have been written without the assistance, and friendship of my colleagues in Utz lab. Dr. Victoria Campbell trained me how to use the equipment before I started my own projects. Previous graduates, Dr. Daniel Killelea, Dr. Deno DelSesto helped many of my academic questions. Yongli Huang is thanked for helping out collecting large amount of data and machine repairs in the past three years. Eric Peterson and Eric Dombrowski were always helpful hands. I am thankful for their efforts in proofreading this dissertation. I have to mention people in the department that I have been lucky to get to know over past years. Zhao Liu, He Meng, Chris Thomas, Zhen Liu, and Shuai Nie have all been fantastic friends.

I must also thank other members in my graduate committee, Prof. Mary Shultz, Prof. Charles Sykes, and the newest member, Prof. Ricardo Metz for serving as mentors of my academic progress.

The experiments performed to produce this thesis are complex and expensive. I am thankful for the funding provided by National Science Foundation and Graduate School of Art and Sciences at Tufts University.

I cannot image how I could come to this stage without the supports I have received from people in both United States and China. I thank you all.

TABLE OF CONTENTS

LIST OF TABLES

LIST OF FIGURES

Chapter I - Introduction

Bond formation and bond breaking are the essence of chemistry. Studying the dynamics and energy flow in such processes is always the key to understanding the nature of a chemistry reaction. Energy flow dynamics play a pivotal role in determining the rates and pathways of catalysis. Heterogeneous catalysis, which is of central importance to chemical industry, impacts wide areas of the economy. Experimental and theoretical studies of gas-surface reaction dynamics have advanced significantly in the past decade and are now providing detailed molecular-level insight into key rate-limiting steps in heterogeneous catalysis. Nowadays, people are able to precisely measure state-resolved reactivities in gas-surface reactions. Particularly, their results show that vibrational energy flow dynamics play an important role in determining the rates and pathways of gas-surface reaction.[1]

Methane dissociation on transition metal surfaces is a benchmark among these studies. This reaction is the rate-limiting step in the steam reforming process shown in Equation 1.1,

$$CH_4 + H_2O \rightarrow 3H_2 + CO \qquad \text{Eq 1.1}$$

which is the principal route for industrial production of H_2. Additionally, as a

prototype for C–H bond activation, the vibrational structure of methane is complicated enough to study many dynamical processes while having a large density of low-energy states and a high cross section for infrared (IR) and Raman excitation, making it a good choice for measuring state-resolved reactivity. Thus, investigations of dynamics and energy flow in methane dissociation has both fundamental and practical significance.

Many studies have been published to better understand the mechanism of methane dissociation on a catalytically active metal surface.[2-12] These studies indicate that cleavage of a single C-H bond is the first and rate-limiting step in the reaction, and both translational and vibrational energy are effective to overcome the barrier. We can draw this process in a 1-D potential energy surface (PES) as shown in Figure 1.1. From the diagram, we can see that if the energy of the incident molecule is low enough, it can be trapped on the surface as shown in route I; if its energy is high enough to pass the barrier, the bond will break and form a chemisorbed methyl group as shown in route III; if the energy is between I and III, it will scatter from the surface.

Based on the 1-D PES, there are two possible mechanisms for a dissociation reaction on the surface. Molecules incident on the surface with low kinetic energy can lose a fraction of their incident energy and become molecularly trapped on the surface, which is known as physisorption. Physisorbed molecules can exchange energy with the surface. If the physisorbed molecule can obtain enough energy to overcome the

barrier of dissociation, it will react via a so-called precursor-mediated mechanism. Reaction competes kinetically with desorption into the gas phase. Molecules with a higher incident kinetic energy will have less chance to trap, and thus less chance to react via precursor-mediated mechanism. Alternately, these high-energy molecules may overcome the activation barrier during their first encounter with the surface in a direct mechanism. The reaction probability for direct reaction increases with increasing kinetic energy.

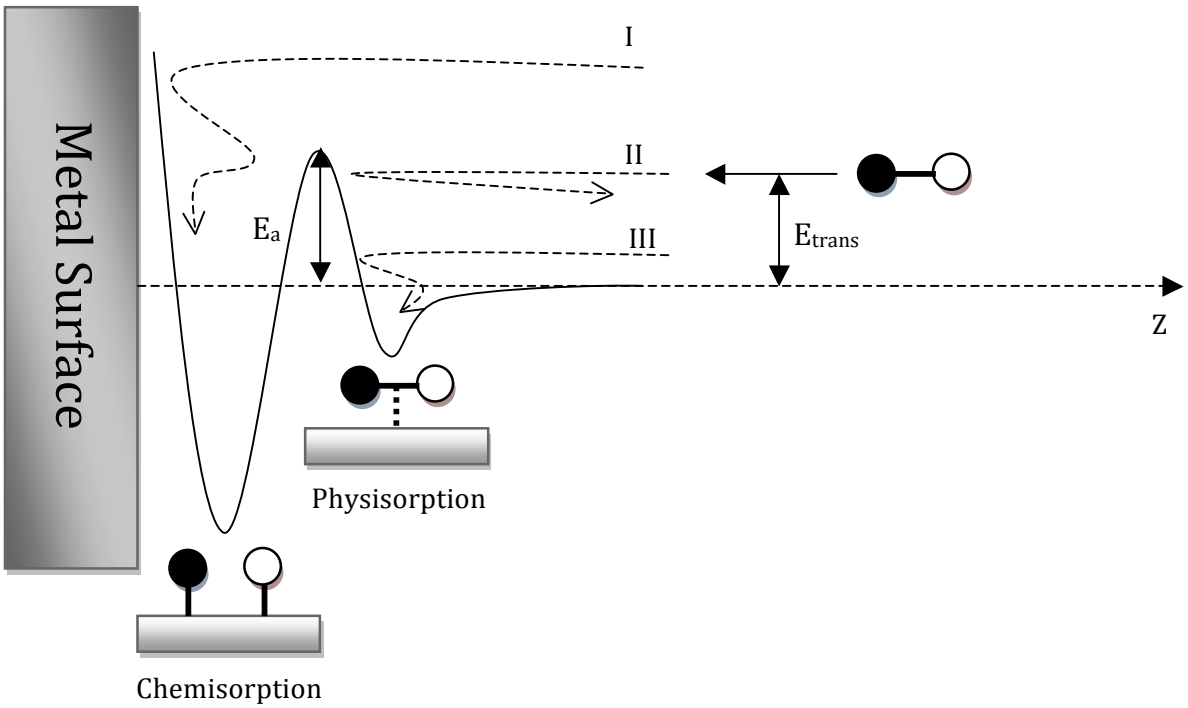

Figure 1.1 Diagram of 1-D potential energy surface. *Z* represents the distance between molecule and the surface. If $E_{trans} > E_a$, molecule *AB* reacts with surface via route I and is chemisorbed on the surface; If $E_{trans} < E_a$, molecule *AB* can physisorb to the surface as route III if it can dissipate sufficient E_{trans} during its first encounter with the surface. Otherwise, *AB* will scatter from surface as route II.

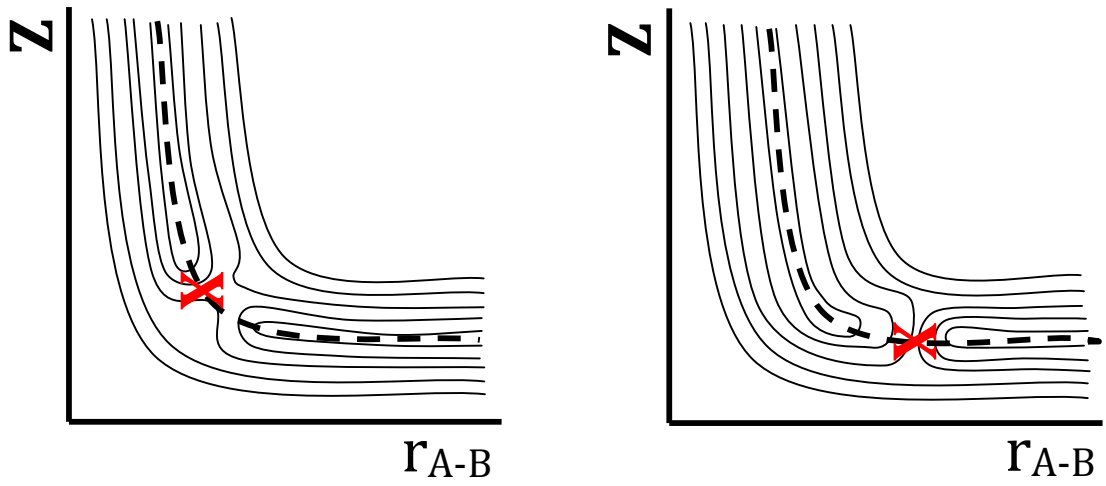

Figure 1.2 Diagram of 2-D potential energy surface.

A) 'Early barrier' and B) 'late barrier'. Contour lines represent potentials. Transition states are marked by the cross. Dashed line represents the reaction coordinate.

For methane dissociation on metal surfaces, the role of different dissociation mechanisms is highly dependent on the identity of the surface. Up to now, published results indicated that methane dissociates directly on Pt(111)[13], Ni(111)[14, 15], and Ni(100)[10], but undergoes both precursor-mediated and direct pathways on Ir(110) and Ir(111),[16-19] with the dominant pathway depending on incident kinetic energy.

The 1-D PES only shows potential energy along the one coordinate - typically the distance from the surface. It is inadequate to model the reaction since it doesn't include the role of vibrational energy. Polanyi noted that a 2-D PES that can better represent the importance of both dynamics and energetics in this surface reaction system.[20] A contour plot shows potential energy as a function of nuclear distance inside the molecule (r_{AB}) and the molecule-surface distance (z). As shown in Figure 1.2, contour lines in the diagram show regions of constant potential, and the dashed line shows the minimum energy path. There are two limiting cases for a 2-D PES, one of which is called 'early barrier', and the other case is called 'late barrier'. For the former, translational energy is most effective in activating the reaction since the transition state, which is represented by the saddle point on the graph, is in the entrance channel. Motion along the z coordinate best overcomes the barrier. In the 'late barrier' case, there is a preference for vibrational energy rather than kinetic energy since the transition state is in the exit channel and the molecular distortion caused by vibrations makes it easier to access the transition state.

As the late barrier is present for methane activation on nickel surface,[21, 22] vibrational energy plays an important role in this particular reaction. Bulb and prior beam-surface experiments have validated the importance of vibrational energy in this reaction.[3-5, 10, 15] However, the vibrational energy contribution calculated in these experiments arises from a thermal distribution of hundreds of vibrational states. The role of specific vibrational states or modes is hidden in these thermally averaged experiments. In order to fully understand the role vibrational energy plays in the process, we need to know the impact from individual vibrational modes. By combining beam-surface scattering with optical excitation of reactants prior to surface impact, state-resolved experiments can probe the role of specific vibrational modes in methane activation on metal surfaces. The first state-resolved measurements of methane activation was done by L. Juurlink et al. on Ni(100).[23] In their work, excitation of CH_4 to v=1 in the antisymmetric stretch vibration (ν_3) promotes CH_4 activation significantly. A few years later, R. Smith et al. reported the reactivity of CH_4 for the similar vibrational state on Ni(111).[24] They found that only ~36 kJ/mol vibrational energy (E_{vib}) in the anti-symmetric stretch (ν_3, v=1) state can promote the CH_4 activation as much as ~45kJ/mol in translational energy (E_{trans}), which suggests the vibrational energy in an anti-symmetric stretch is more efficient than kinetic energy to promote CH_4 activation on Ni(111). The difference between similar CH_4 excitation on different surfaces offers evidence for the role of vibrational symmetry of gas-phase CH_4 in accessing the transition state. To date, many state-resolved studies have been done for IR excited CH_4 activation on different surfaces.[25-28]

In order to compare the roles different vibrational modes play in the overall reactivity, we use a term, η_{vib}, which is expressed by Equation 1.2 and represents the efficacy of a particular vibrational mode.

$$\eta_{vib} = \frac{E_{trans}^{v=0} - E_{trans}^{v=1}}{E_{vib}} \qquad \text{Eq 1.2}$$

As a summary of published results, we have summarized efficacies of various vibrational modes on both Ni(111) and Ni(100) as shown in Table 1.1.

Table 1.1 Efficacies of different vibrational modes of CH_4 activation on nickel surfaces

State	E_{vib}	Surface	ΔE_{trans}	η_{vib}
ν_1	35 kJ/mol	Ni(100)	50 kJ/mol	1.4[25]
ν_3	36 kJ/mol	Ni(111)	45 kJ/mol	1.25[24]
ν_3	36 kJ/mol	Ni(100)	34 kJ/mol	0.94[23]
$2\nu_3$	71 kJ/mol	Ni(111)	65 kJ/mol	0.90[26]
$3\nu_4$	45 kJ/mol	Ni(111)	34 kJ/mol	0.72[27]
$3\nu_4$	45 kJ/mol	Ni(100)	-	≤ 0.5[27]
$\nu_2 + \nu_4$	34 kJ/mol	Ni(111)	15 kJ/mol	0.44[28]

It is worth mentioning that most studies have focused on stretching modes of CH_4 rather than bending modes. There are two reasons. First, bending states in methane have about half the vibrational frequency of stretching states. As a result, fundamentals of stretching vibrations are accessible to convenient IR laser sources,

but studies of bending states require use of weaker overtone transitions. Combination vibrations containing the doubly degenerate ν_2 bend have particularly poor infrared absorption cross sections. Second, bending states are often found to couple more poorly to the reaction coordinate, resulting in less enhancement to the overall reactivity than stretching states. Thus, it is hard to extract the state-resolved reaction probabilities. However, bending states are important potential contributors to CH_4 activation under thermal conditions, as they dominate the population of thermally excited vibrations. We need to clarify their roles in the overall reactivity no matter the difficulty. In Chapter V of this thesis, we present state-resolved reactivity measurements of the $\nu_2 + \nu_4$ bending vibration of CH_4 on Ni(111). This state is a member of the pentad polyad of vibrational states that play an important role in the thermal activation of methane. We quantify the state-resolved reactivity of methane in this particular vibrational state over a wide range of translational energies, and compare the efficacy for the $\nu_2 + \nu_4$ bend with that of the ν_3 stretching and $3\nu_4$ bending states to gain insight into the ability of ν_2 excitation to promote dissociative chemisorption. The result permits a detailed comparison of the role of stretch and bend excitation of methane dissociative chemisorption on Ni(111).[28]

In addition to vibrational mode selectivity, we are able to selectively control the bond cleavage during the methane activation on the surface. Isotopic substitution can tune the vibrational character of molecules, and excitation of localized vibrations can lead leading to bond selectivity. Killelea et al. reported the bond

selectivity of CHD_3 activation on Ni(111).[29] They use IR laser excitation to achieve the preferential cleaving of the C-H bond (the experimental details are introduced in Chapter II). This experiment demonstrated bond selectivity in a gas-surface reaction and indicated the lack of energy redistribution between C-H and C–D bonds. More recently, the Beck group has used IR absorption to show bond selectivity in the dissociation of partially deuterated methanes on Pt(111).[30] We selectively excite the C-H bond in CH_2D_2, and compare state-resolved reactivities of symmetric stretch (ν_1) and anti-symmetric stretch (ν_6) for CH_2D_2 dissociation on Ni(111). Details of this project are introduced in Chapter VI.

Besides the effect of vibrational energy in the methane reagent, people investigated the role of surface vibrations as well. D. Killelea et al. reported a strong surface temperature effect on reactivity of CH_4 on Ni(111), and theoretical calculations are consistent with this observation.[31] Campbell et al. compared the sticking curves for state-resolved reactivity of CH_4 in the ν_3 excitation state on Ni(111) at 475K and 90K.[32] From the sticking curve of this work in Figure 1.3, at low kinetic energies, there is a near 8-fold increase in reactivity from a 90K surface to a 475K surface. The reactivity enhancement decreases from 8-fold to 2-fold increase as the kinetic energy increases. This verified the theoretical prediction of surface temperature effects on the reactivity of CH_4 activation, especially in an energy-starved regime. In Figure 1.3, S_0 data at T_S = 90K show an inflection point, which makes the 90K data different from 475K and 550K data. This can be explained as a combination of a variation of the barrier height due to lattice motion, and a shift of the location of the

barrier height with respect to the PES as a function of atom displacement.[21, 22, 33] If this explanation is true, we would predict all C-H cleavage on Ni(111) surface will have same threshold energies since the effect wholly depends on the surface lattice structure and its temperature. Our results of the selective CH_2D_2 dissociation on Ni(111) provide further evidence to this argument. We will introduce more details in Chapter VI.

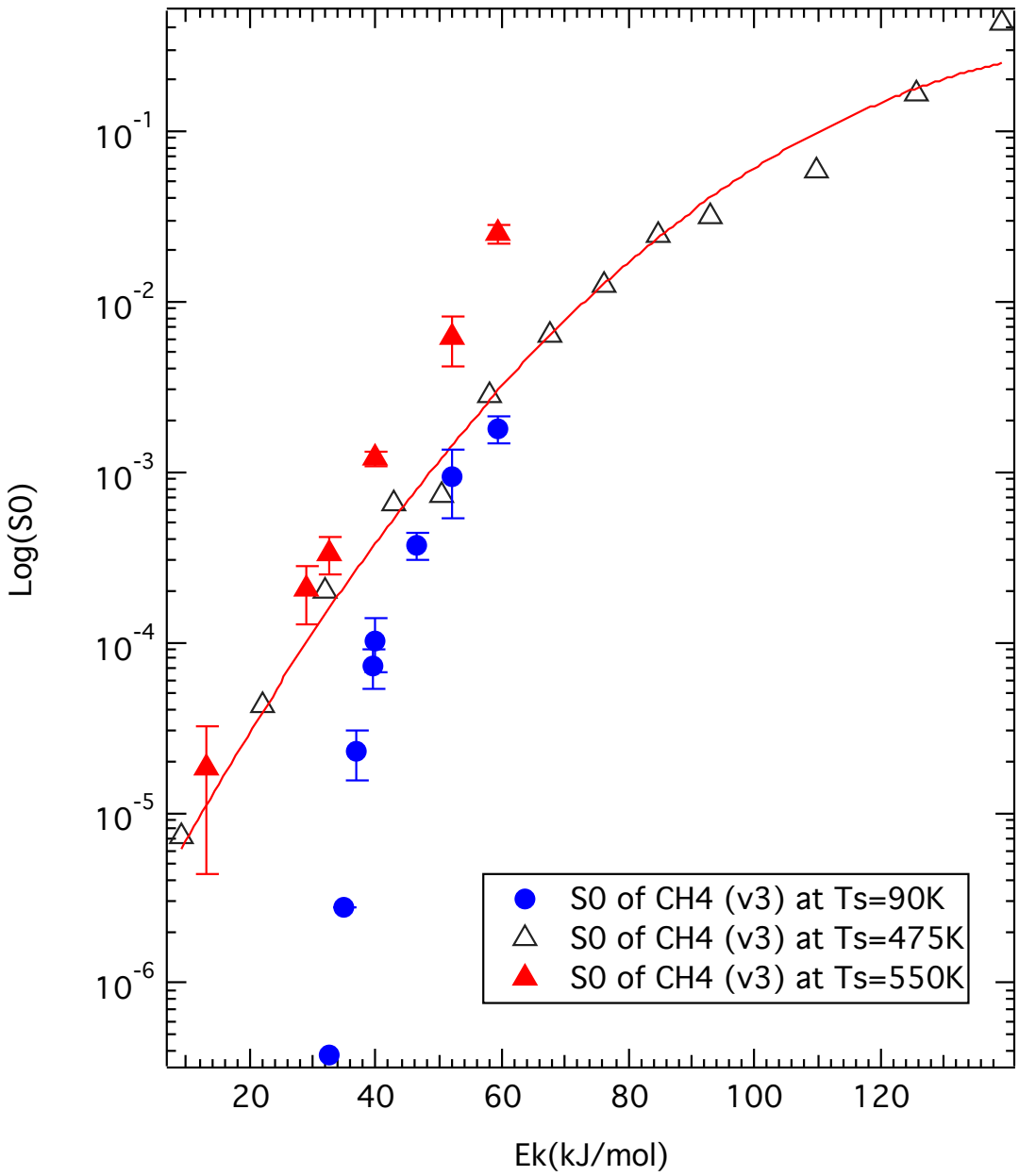

Figure 1.3 State-resolved reactivities of CH_4 (ν_3) dissociation on Ni(111) at different T_s across a range of E_{trans}. S_0 data at T_S = 90 K and 550 K are from Ref. 33 (Campbell et al.), and S_0 data at T_S = 475 K are from Ref. 24 (Smith et al.).

The state-resolved measurements of CH_4 reactivity on metal surfaces have yielded detailed insights into how methane's vibrational energy promotes reactivity. To date, such measurements have relied on post-dose quantification of reaction products in order to obtain reactivity as a function of methane's translational energy, internal vibrational and rotational state, and surface temperature. In Chapter IV of this thesis, we introduce a new detection scheme for measuring state-resolved reactivity based on the 'King and Wells' method[34]. This molecular beam reflectivity method can improve reproducibility of reactivity and significantly decrease the experimental time for state-resolved measurements. Rather than modulate the flux of molecules incident on the surface, we modulate laser excitation. By doing so, the partial pressure change due to laser modulation reveals the difference in sticking probability with and without laser excitation, which is the key quantity needed to obtain state-resolved reactivity. We demonstrate the method works well for methane (ν_3, v=1) incident on Ni(111) and show that it provides real-time coverage dependent reaction probabilities while decreasing data acquisition time and permitting a more expansive exploration of how energy and chemical identity influences reactivity at the gas-surface interface. This experimental method can extend state-resolved study of CH_4 activation to a wider range of experimental conditions and chemical systems.

Beside experimental chapters in this thesis, we also introduce an improved model of the state-resolved CH_4 reactivity on Ni(111) in Chapter III. The method relies on a detailed knowledge of the vibrational structure and vibrational energy transfer

dynamics of methane in a supersonic expansion. Non-equilibrium cooling of vibrational states within polyads leads to the population of a single vibrationally excited state under easily obtained expansion conditions, even though several excited vibrational states would contain significant population under the normal thermal conditions of the nozzle source. Not only can we predict the state-resolved reactivity, we can also apply this model to extract the reactivity of methane in the rovibrational ground state, which will make the state-resolved reactivity results free from small, but significant contributions from vibrationally excited states existing in the supersonic beam.

References

1. Crim, F. F., Bond-selected chemistry: vibrational state control of photodissociation and bimolecular reaction. *J. Phys. Chem.* **1996,** *100*, 12725-12734.

2. Winters, H. F., KINETIC ISOTOPE-EFFECT IN DISSOCIATIVE CHEMISORPTION OF METHANE. *Bulletin of the American Physical Society* **1975,** *20* (7), 861-861.

3. Winters, H. F., ACTIVATED, DISSOCIATIVE CHEMISORPTION OF METHANE ON TUNGSTEN. *Journal of Chemical Physics* **1975,** *62* (6), 2454-2460.

4. Yates, J. T.; Zinck, J. J.; Sheard, S.; Weinberg, W. H., SEARCH FOR VIBRATIONAL ACTIVATION IN THE CHEMISORPTION OF METHANE. *Journal of Chemical Physics* **1979,** *70* (5), 2266-2272.

5. Luntz, A. C.; Bethune, D. S., ACTIVATION OF METHANE DISSOCIATION ON A PT(111) SURFACE. *Journal of Chemical Physics* **1989,** *90* (2), 1274-1280.

6. Harris, J.; Simon, J.; Luntz, A. C.; Mullins, C. B.; Rettner, C. T., THERMALLY ASSISTED TUNNELING - CH4 DISSOCIATION ON PT(111). *Physical Review Letters* **1991,** *67* (5), 652-655.

7. Campbell, R. A.; Szanyi, J.; Lenz, P.; Goodman, D. W., METHANE ACTIVATION ON CLEAN AND OXIDIZED NI(100). *Catalysis Letters* **1993,** *17* (1-2), 39-46.

8. Weinberg, W. H., ALKANE ACTIVATION ON TRANSITION-METAL SURFACES - BEAMS, BULBS, AND NEW INSIGHTS. *Langmuir* **1993,** *9* (3), 655-662.

9. Luntz, A. C.; Winters, H. F., DISSOCIATION OF METHANE AND ETHANE ON PT(110) - EVIDENCE FOR A DIRECT MECHANISM UNDER THERMAL CONDITIONS. *Journal of Chemical Physics* **1994,** *101* (12), 10980-10989.

10. Holmblad, P. M.; Wambach, J.; Chorkendorff, I., MOLECULAR-BEAM STUDY OF DISSOCIATIVE STICKING OF METHANE ON NI(100). *Journal of Chemical Physics* **1995,** *102* (20), 8255-8263.

11. Egeberg, R. C.; Ullmann, S.; Alstrup, I.; Mullins, C. B.; Chorkendoff, I., Dissociation of CH4 on Ni(111) and Ru(0001). *Surface Science* **2002,** *497* (1-3), 183-193.

12. Mortensen, H.; Diekhoner, L.; Baurichter, A.; Luntz, A. C., CH4 dissociation on Ru(0001): A view from both sides of the barrier. *Journal of Chemical Physics* **2002,** *116* (13), 5781-5794.

13. Beckerle, J. D.; Johnson, A. D.; Yang, Q. Y.; Ceyer, S. T., COLLISION-INDUCED DISSOCIATIVE CHEMISORPTION OF CH4 ON NI(111) BY INERT-GAS ATOMS - THE MECHANISM FOR CHEMISTRY WITH A HAMMER. *Journal of Chemical Physics* **1989,** *91* (9), 5756-5777.

14. Lee, M. B.; Yang, Q. Y.; Tang, S. L.; Ceyer, S. T., ACTIVATED DISSOCIATIVE CHEMISORPTION OF CH4 ON NI(111) - OBSERVATION OF A METHYL RADICAL

AND IMPLICATION FOR THE PRESSURE GAP IN CATALYSIS. *Journal of Chemical Physics* **1986,** *85* (3), 1693-1694.

15. Lee, M. B.; Yang, Q. Y.; Ceyer, S. T., DYNAMICS OF THE ACTIVATED DISSOCIATIVE CHEMISORPTION OF CH4 AND IMPLICATION FOR THE PRESSURE GAP IN CATALYSIS - A MOLECULAR-BEAM HIGH-RESOLUTION ELECTRON-ENERGY LOSS STUDY. *Journal of Chemical Physics* **1987,** *87* (5), 2724-2741.

16. Seets, D. C.; Reeves, C. T.; Ferguson, B. A.; Wheeler, M. C.; Mullins, C. B., Dissociative chemisorption of methane on Ir(111): Evidence for direct and trapping-mediated mechanisms. *Journal of Chemical Physics* **1997,** *107* (23), 10229-10241.

17. Seets, D. C.; Wheeler, M. C.; Mullins, C. B., Trapping-mediated and direct dissociative chemisorption of methane on Ir(110): A comparison of molecular beam and bulb experiments. *Journal of Chemical Physics* **1997,** *107* (10), 3986-3998.

18. Seets, D. C.; Wheeler, M. C.; Mullins, C. B., Mechanism of the dissociative chemisorption of methane over Ir(110): Trapping-mediated or direct? *Chemical Physics Letters* **1997,** *266* (5-6), 431-436.

19. Reeves, C. T.; Seets, D. C.; Mullins, C. B., Low translational energy mechanisms in the dissociative chemisorption of methane on iridium and platinum surfaces. *Journal of Molecular Catalysis a-Chemical* **2001,** *167* (1-2), 207-215.

20. Polanyi, J. C., SOME CONCEPTS IN REACTION DYNAMICS. *Accounts of Chemical Research* **1972,** *5* (5), 161-&.

21. Nave, S.; Jackson, B., Methane dissociation on Ni(111): The effects of lattice motion and relaxation on reactivity. *Journal of Chemical Physics* **2007,** *127* (22).

22. Nave, S.; Jackson, B., Methane dissociation on Ni(111): The role of lattice reconstruction. *Physical Review Letters* **2007,** *98* (17).

23. Juurlink, L. B. F.; McCabe, P. R.; Smith, R. R.; DiCologero, C. L.; Utz, A. L., Eigenstate-resolved studies of gas-surface reactivity: CH4 (nu(3)) dissociation on Ni(100). *Physical Review Letters* **1999,** *83* (4), 868-871.

24. Smith, R. R.; Killelea, D. R.; DelSesto, D. F.; Utz, A. L., Preference for vibrational over translational energy in a gas-surface reaction. *Science* **2004,** *304* (5673), 992-995.

25. Maroni, P.; Papageorgopoulos, D. C.; Sacchi, M.; Dang, T. T.; Beck, R. D.; Rizzo, T. R., State-resolved gas-surface reactivity of methane in the symmetric C-H stretch vibration on Ni(100). *Physical Review Letters* **2005,** *94* (24).

26. Bisson, R.; Sacchi, M.; Dang, T. T.; Yoder, B.; Maroni, P.; Beck, R. D., State-resolved reactivity of CH4(2 nu(3)) on Pt(111) and Ni(111): Effects of barrier height and transition state location. *Journal of Physical Chemistry A* **2007,** *111* (49), 12679-12683.

27. Juurlink, L. B. F.; Smith, R. R.; Killelea, D. R.; Utz, A. L., Comparative study of C-H stretch and bend vibrations in methane activation on Ni(100) and Ni(111). *Physical Review Letters* **2005,** *94* (20).

28. Chen, N.; Huang, Y.; Utz, A., State-resolved reactivity of methane (ν 2 + ν 4) on Ni(111). *In preparation* **2013**.

29. Killelea, D. R.; Campbell, V. L.; Shuman, N. S.; Utz, A. L., Bond-selective control of a heterogeneously catalyzed reaction. *Science* **2008,** *319* (5864), 790-793.

30. Chen, L.; Ueta, H.; Bisson, R.; Beck, R. D., Vibrationally bond-selected chemisorption of methane isotopologues on Pt(111) studied by reflection absorption infrared spectroscopy. *Faraday discussions 157*, 285-295.

31. Henkelman, G.; Arnaldsson, A.; Jonsson, H., Theoretical calculations of CH4 and H-2 associative desorption from Ni(111): Could subsurface hydrogen play an important role? *Journal of Chemical Physics* **2006,** *124* (4).

32. Campbell, V.; Chen, N.; Utz, A., State Resolved Measurements of Surface Temperature Dependence in Methane Reactivity on Ni(111). *in preparation* **2013**.

33. Nave, S.; Jackson, B., Methane dissociation on Ni(111) and Pt(111): Energetic and dynamical studies. *Journal of Chemical Physics* **2009,** *130* (5).

34. King, D. A.; Wells, M. G., Molecular beam investigation of adsorption kinetics on bulk metal targets: Nitrogen on tungsten. *Surface Science* **1972,** *29* (2).

Chapter II – Experimental Methods

Section 2.1 - Overview of Beam-surface Scattering Chamber

Our ultra-high vacuum (UHV) beam-surface scattering chamber has been previously explained in detail.[1-5] In this section, we will only briefly introduce the system and address modifications on the existing setup.

This UHV apparatus consists of four stages pumped individually, including the source chamber (SC), first differential chamber (FDC), second differential chamber (SDC), and the main chamber (MC), where the base pressure can reach 6×10^{-11} Torr. In the SC, a supersonic molecular beam is formed by expanding a high-pressure (pressure ≥ 20 PSI) gas through a tiny hole on a nozzle, which is housed on a two-dimensional translation stage. This adjustable stage is an improvement of the original nozzle holder[4], so we can finely adjust the beam position without venting the chamber. Besides the first skimmer between the SC and the FDC, there is a second skimmer separating the FDC and the SDC in order to further collimate the molecular beam to crystal in MC. A sliding beam valve with three different size holes separates the SDC and the MC while modifying the size of the molecular beam. The three different sizes are called small beam valve hole (SBVH), medium beam valve

hole (MBVH), and large beam valve hole (LBVH), respectively. A schematic view of the chamber is shown in Figure 2.1.

In the FDC, there is an optical set-up, which is composed by two nearly-parallel gold plated mirrors to maximize the IR excitation of molecules in the molecular beam. The IR Laser, which is orthogonal to the molecular beam, passes through a sapphire window and enters the FDC. Photons pass through the molecular beam and reflect between the two gold mirrors, which form a multiple-pass cell. Besides the adjustable screws on one of the mirrors, the second mirror can be adjusted from outside the chamber, which is used to optimize alignment of the multipass cell and maximize excitation of molecules in the beam.[6] The SDC houses a pyroelectric detector (PED) and a chopper wheel with LED timing electronics. The PED that is precision aligned along the beam line is used to monitor the photon absorbance and determine the fraction of excited CH_4 in the molecular beam. The chopper wheel is used for time-of-flight (TOF) measurements, and LED is used to identify the position of slots on the chopper wheel from outside the chamber.

The MC houses the metal single crystal (crystal from FOM Surface Preparation Laboratory, Zaandam, Netherlands) and tools for analysis, including Auger Electron Spectrometer (AES; made by VG Microtech, Model: LEG63 electron gun and VG-100AX hemispherical analyzer), Quadruple Mass Spectrometer (QMS; made by UTI, Model: 100-C) and Sputtering Gun (made by PHI, Model 04-191). The crystal setup includes a nickel single crystal mounted onto a four-dimensional (x, y, z and θ)

manipulator (made by McAllister Technical Services). We use a single-wall cryostat (made by McAllister, Part Number: LN_2-HAT) assembled with the manipulator. Liquid nitrogen cools the crystal to a temperature of 90K. A thoriated iridium filament mounted behind the crystal (rear filament) provides radiative or e-beam heating to warm the crystal. We use a proportional–integral–derivative (PID) control unit to precisely control the temperature of the crystal and generate the ramp used in Temperature Programmed Desorption (TPD) experiments. A sliding front filament made by tungsten is placed in front of the crystal thermally cracks H_2 or D_2 and produces H or D atoms that we use to perform the bulk H/D titration, which we will introduce in Section 2.4. We use AES to verify the cleanness of the surface as well as measuring absolute carbon coverage, which is achieved by comparing the integrated signal from carbon KLL (252 eV) and nickel LMM (848 eV) features to the calibrated saturation dose.[7] We use QMS for multiple measurements, including beam fluxes, TOF, residual gas analysis (RGA), King and Wells (K&W), TPD, and O_2 titration experiments.

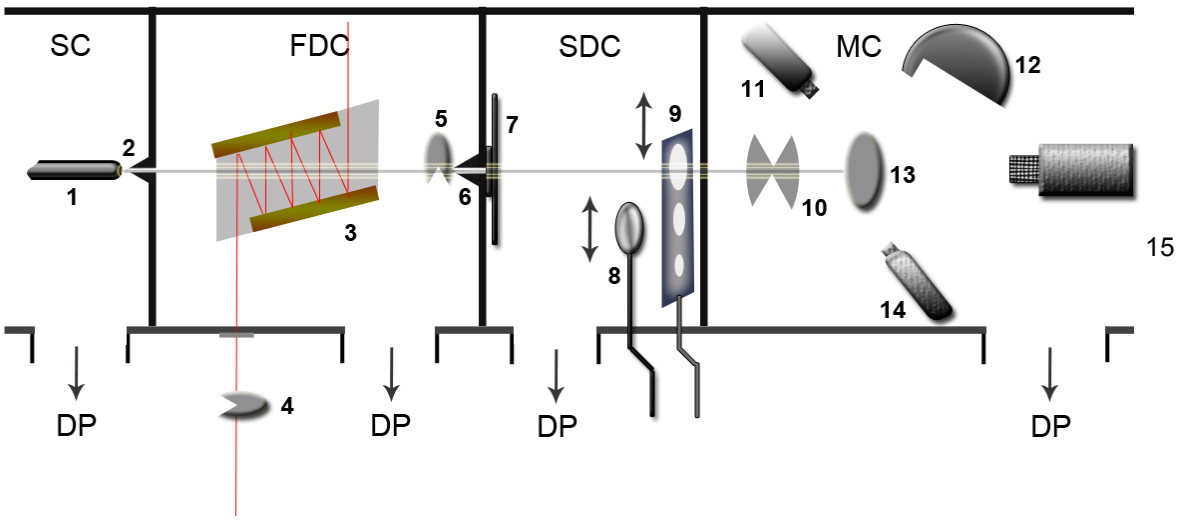

Figure 2.1. Schematic view of the current UHV system: 1) Molecular beam nozzle; 2) and 6) Skimmers; 3) Multiple-pass cell for IR excitation; 4) Shutter used in King and Wells modulation for laser chopping; 5) Molecular beam shutter with time controller; 7) Chopper wheel with LED indicator for TOF; 8) PED for the detection of IR absorbance; 9) Sliding beam valve with different size holes; 10) Rotatable beam flag; 11) LEG-63 electron gun of AES system; 12) VG-100AX hemispherical analyzer of AES system; 13) Ni(111) single crystal; 14) PHI 04-191 sputtering gun; 15) UTI 100-C QMS.

Section 2.2 - O_2 Titration

Previous projects in our group primarily used AES as their way to find the carbon coverage on the surface. In such a method, the coverage of carbons on surface is determined by the ratio of the integration of the carbon (252 eV) and nickel (848 eV) AES features to a well-known saturation measurements, which is verified as 0.43 monolayer (ML) for Ni(111).[7-9] The AES calibration of C coverage has two shortcomings. First,slight changes in the lineshape of the C or Ni features made it difficult to reproducibly measure small differences in C coverage when the contrast between laser-on and laser off doses is small. Second, AES is incapable of distinguishing isotopes, which make it impossible to perform isotope specific experiments.

Another method we used in determining coverage of carbons is known as O_2 titration. This method has been well established as a valid way to measure reactivity in various reaction systems.[10-13] In general, it uses a molecular oxygen beam to titrate the adsorbed carbons on surface by forming CO that desorbs from the surface. We have modified the conventional O_2 titration slightly to make it suitable for our setup.[1]

In the beginning of experiments, we use AES to check the cleanness of surface. If there is sulfur on the surface, which is quite common for Ni crystal, a five minutes

sputtering process is performed by a sputtering gun that is angled 45° off the surface normal with a 1×10^{-4} Torr background pressure of Ar. Then the crystal is annealed to 1050K for 15 minutes to anneal sputter-induced defects and restore a smooth (111) surface. If residual carbon is found, it can be removed by flashing the crystal to 1000K. In a rare case that oxygen features appear in AES, we warm the crystal to 1000 K in the presence of 2×10^{-6} Torr of H_2 to reduce the oxygen contaminants on surface.

Once the surface is clean, a CH_4 beam is dosed on the crystal surface. For molecular beams, we can use a variety of gas mixtures of CH_4 seeded with either He or H_2 as a carrier gas across a wide range of nozzle temperatures and surface temperatures. Doses are performed with our without laser excitation. After the dose completed, remaining gas in the manifold is pumped out through a roots blower and a mechanical pump in the fore-line of SC while the QMS is warming up.

The surface temperature has to be 475K or higher for the O_2 titration in order to make the oxygen react with absorbed C atom and desorb as CO molecules.[1] In our setup, we use a supersonically expanded molecular oxygen beam that is generated by the same nozzle as carbon dose at room temperature and introduced into MC through MBVH. The Ni(111) surface is initially blocked by the MC beam flag in order to generate a baseline for the integration afterwards. After the trace of *m/z=28* signal in the MS spectrum became flat, we remove the flag and expose the surface to the oxygen beam. The oxygen dissociates rapidly on the surface providing O atoms,

which react with adsorbed C atoms and immediately desorb as CO. This process can be expressed as equation 2.1.

$$O_2(g) + 2C(ad) \rightarrow 2O(ad) + 2C(ad) \rightarrow 2CO(g) \qquad \textbf{Eq. 2.1}$$

Typically we monitor signals from *m/z=16, 18, 28* and *44*. Some publications reported a secondary CO_2 product besides desorbed CO,[11] but we did not see any changes in the *m/z=44* signal during our O_2 titration experiments. This is consistent with Abild-Pederson et al. in their work of the same reaction system.[12] In order to ensure no residual oxide layer on the crystal or filaments after O_2 titration, we use a reduction cycle following every O_2 titration. In such reduction cycle, the MC is backfilled with 2×10^{-6} Torr H_2 through a leak valve. During the H_2 treatment, the crystal temperature is brought to 1000K and the ionization filament in MS is turned on. After the H_2 treatment, the crystal is annealed for ~5 minutes. Based our AES check afterwards, this reduction process is sufficient to keep the surface clean for the next experiment. A typical CO desorption spectrum from our LabVIEW based MS interface program is shown in Figure 2.2 for a 475K Ni(111) surface dosed with 0.25% CH_4/H_2 beam at T_{nozzle} = 1000K. The peak in the trace of *m/z*=28 is the feature of CO desorption, starting immediately from the exposure of O_2 molecular beam to the surface. Correspondingly, we can see a slight dip in the trace of *m/z=16* at the same time of O_2 exposure, indicating the uptake of oxygen by surface as forming CO.

In order to use this technique as a quantitative method to determine sticking probabilities, we need a calibration method to analyze the CO desorption feature. In

order to maintain a single layer structure of absorbed carbon atoms, we limit the coverage of every dose in the range of 0.05~0.10 ML. The area under the *m/z=28* peak can be integrated to give a value of counts for the CO desorption. There are two ways to convert this value into the ML coverage of carbon. Previous projects in our group used a calibration curve generated by saturation doses. It consisted of a series of methane doses performed under well-established experimental conditions, that have documented sticking probabilities and produce a known coverage.[1] By systematically changing dose-time, a linear relationship can be established between value of counts and ML coverages of carbon (ML ≤ 0.15). Using a calibration curve prevents repeated saturation measurements from day to day once the curve is established. However, it has a large reliance on the chamber conditions and settings in MS, and any attenuations or amplifications in detectable signal levels require a new calibration curve. Another issue about using calibration curves generated by methane doses is that the saturation coverage of C can depend on the energy of the beam. In order to make coverages more accurate in a long-period project, we use daily C_2H_4 saturation dose instead of calibration curves to relate the integrated area of the CO feature into ML coverage, especially in the project of CH_4 reactivity at $\nu_2+\nu_4$ excitation. C_2H_4 does not form multiple absorption layers on the surface, so it provides a more reliable value of integrated counts corresponding to the saturation C coverage than CH_4. Also we reduced the impact from chamber and MS conditions by performing the CH_4 and C_2H_4 doses on the same day. In our experiments, the difference of integrated counts from day to day C_2H_4 saturation doses is within 4%.

We convert the integrated value of counts (*Counts*) to ML coverage of carbon by Equation 2.2.

$$ML_{carbon} = \frac{Counts_{CH_4}}{Counts_{C_2H_4}} \times 0.43ML \qquad \textbf{Eq. 2.2}$$

Figure 2.3 shows a sample spectrum of C_2H_4 saturation dose from a 4% C_2H_4/He beam at room temperature nozzle with $T_{surface}$ = 475K.

On a low temperature surface, dissociated H atoms may stay on the surface and block reaction sites from the CH_4 dissociation.[14, 15] Thus, the saturation coverage of C decreases. In our experiments, the saturation coverage of C on Ni(111) is ~0.20 ML at $T_{surface}$ = 95K, but 0.43 ML at $T_{surface}$ = 475K. Besides H blocking, we also need to exclude the impact of residual carbons, which are accumulated on other components inside the MC, from our O_2 titration results. We measured the amount of CO desorbed after a background dose, which is a dose performed under exactly the same experimental conditions but with a non-reactive room temperature beam. By subtracting the integrated counts of background dose, we can eliminate the impact of residual carbons from our O_2 titration results. In our experiments, the background dose usually generates a C coverage between 0.005 to 0.01 ML.

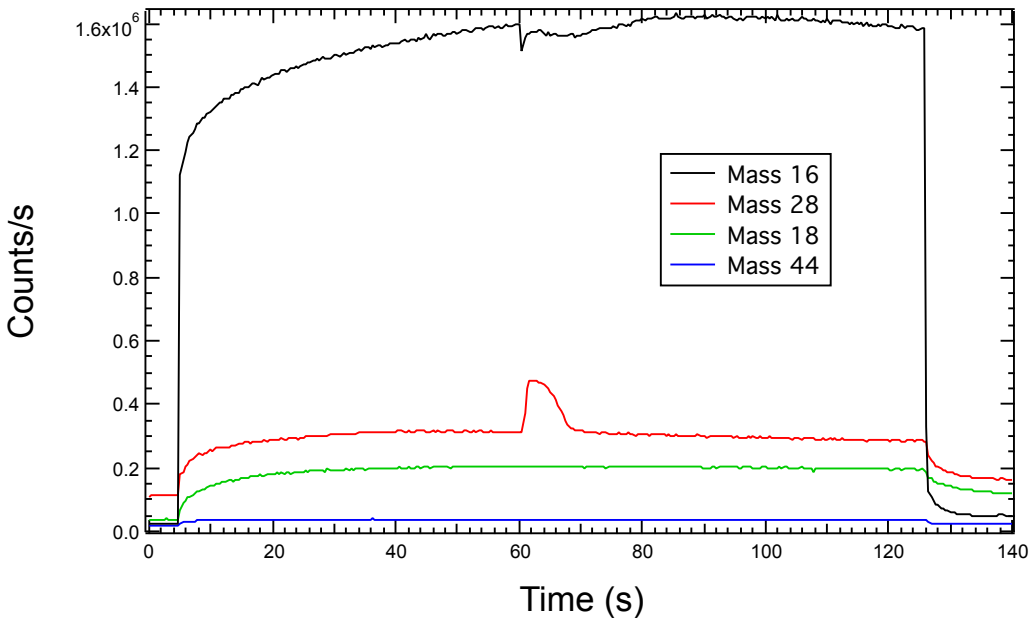

Figure 2.2 CO desorption feature from a CH_4 dose after O_2 titration. Masses 16, 18, 28 and 44 were monitored after the surface exposed to a molecular oxygen beam at 60 sec while the surface temperature was held at 475K.

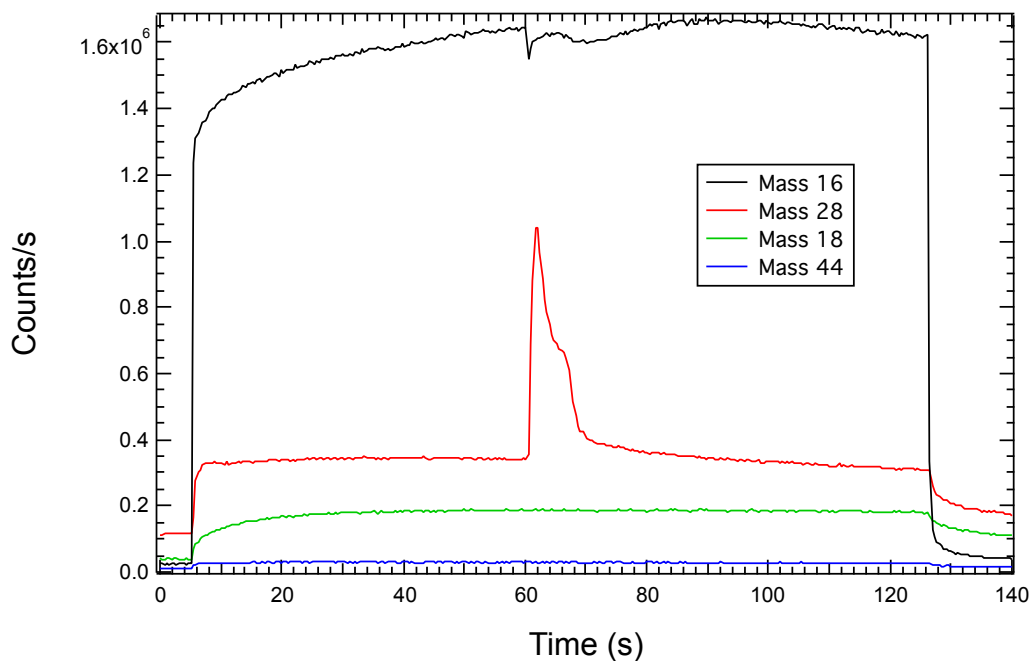

Figure 2.3 CO desorption feature from a typical C_2H_4 saturation dose. Mass 16, 18, 28 and 44 were monitored after the surface exposed to a molecular oxygen beam at 60 sec while the surface temperature was held at 475K.

Section 2.3 - King and Wells Modulation

King and Wells (K&W) measurements of surface reactivity were first reported by D. A. King and M. Wells in 1972 for the absorption of N_2 on tungsten.[16] In K&W experiments, surface reaction is detected from the reduction in partial pressure of the reagent, as monitored by MS signals. Unlike AES or O_2 titration, K&W provides a real-time detection of reactivity in gas-surface reactions. This unique feature brings two advantages. First, it can reduce the experimental time as no post-dose measurements or calibrations needed, which sometimes takes even longer than dosing itself. Second, it is able to measure reactivity when the product is unstable on the surface. This is impossible in post-dose methods like AES or O_2 titration. For example, when the surface temperature is high (≥ 600K), carbon atoms from chemisorbed CH_4 will "dissolve" into the bulk of the Ni crystal and no longer be "visible" in AES or O_2 titration. In such cases, there is no way to measure the reactivity except using real-time methods like K&W.

Based on K&W, we have developed a modified scheme to measure the state-resolved reactivity of CH_4 dissociation on Ni(111) with high efficiency.[17] It is suitable for measurement at $T_{surface} \geq 600K$ where C atoms no longer exist on the surface. It can save a lot of experimental time since reactivity with and without laser are measured at the same time and no further post-dose measurements or calibrations are required. Compared to AES, K&W methods typically have a high detection limit. This is because they detect reflectivity as a reduction in the total

partial pressure of the reagent. When reactivity is low, the depletion is a small fraction of a large signal. Accordingly, this scheme requires that the sticking probability (S_0) to be measured be higher than about 0.01. We choose a high-reactivity beam of 1% CH_4 in H_2 expanded continuously at T_{nozzle} = 800K to demonstrate the approach.

A continuous wave (CW) and single frequency IR laser, which will be introduced in section 2.5, excites a fraction of CH_4 molecules to J=1 of ν_3 C-H vibration state via the R(1) transition at 3038.50 cm^{-1}. A stable frequency generator drives a shutter that chops the laser before it enters the chamber, providing laser modulation in a square-wave form as shown in the top panel of Figure 2.4. We use the PED in the SDC to quantify the IR absorption of molecules (f_{exc} = 11~18% depends on T_N). Methane's long IR radiative lifetime and collision-free conditions in the supersonic beam ensured that the optically excited molecules impinged on the nickel surface in their initially excited state prepared by the IR laser. After entering the MC, the molecular beam is initially blocked from the crystal by a rotatable beam flag, so the partial pressure of CH_4 can reach equilibrium and produce a baseline in the K&W spectrum. When the flag is removed after ~60 seconds, CH_4 molecules dissociate and form C and H atoms on the surface. At $T_{surface}$ = 800K, dissociated H atoms recombine and desorb as H_2 promptly while C atoms diffuse into the bulk of crystal. As the laser is chopped, CH_4 molecules with and without laser excitation impinge the surface alternatively. This results a high-low-high trace of CH_4 partial pressure (*m/z=15*) in the K&W spectrum, which is shown in the bottom panel of Figure 2.4.

The difference between high and low levels on the partial pressure trace represents different reactivity of CH_4 with and without laser excitation. Thus, the ratio of modulation height to the initial rise of CH_4 partial pressure before the reaction gives the key quantity ($S_0^{LaserOn} - S_0^{LaserOff}$) in state-resolved reactivity measurements.

Like other diffusion processes, the absorption rate of C atoms into the bulk of the Ni crystal depends on surface temperature. For surface temperatures of 800K or higher, the absorption rate is faster than the dissociation rate of the high-energy CH_4 whether it is IR excited or not. Thus, there are no reaction sites blocked on the surface and the modulation feature remains a shape of square wave as shown in Figure 2.5 a). If the surface temperature is less than 800K, the absorption rate is reduced, so C atoms will accumulate on the surface and block reaction sites. This causes the CH_4 partial pressure to increase as site blocking reduces reactivity. In the mean time, the modulation feature becomes smaller and smaller as reactivity decreases, which is shown in Figure 2.5 b). Since all surface temperatures used in the K&W studies reported in this thesis are higher than 600K, where H atoms recombine and desorb as H_2 promptly on Ni(111), there is no concern of H site-blocking. More details of this project are explained in Chapter III.

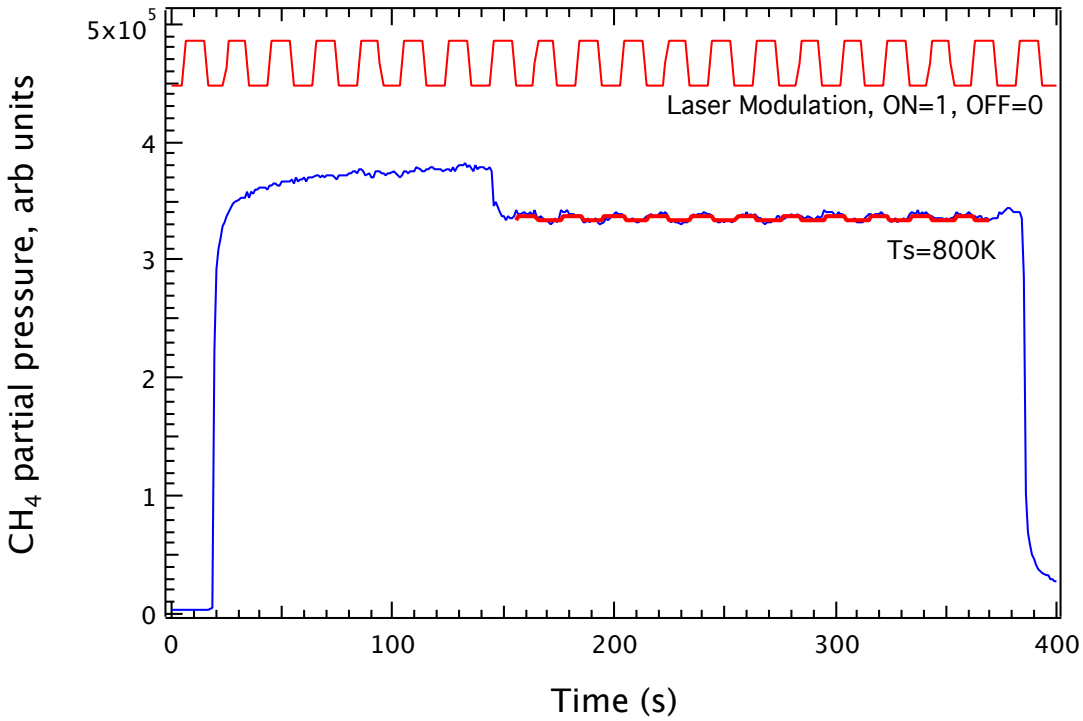

Figure 2.4 A sample spectrum from the K&W laser modulation. The top square wave in red is from the frequency generator that controls the laser shutter. The red fitting curve on the high-low-high trace of CH_4 partial pressure shows the same frequency as the top wave, but with its amplitude adjusted to fit the data. The height of the square wave fitting, divided by the magnitude of the initial rise in the CH_4 partial pressure signal, gives $S_0^{Laseron} - S_0^{Laseroff}$.

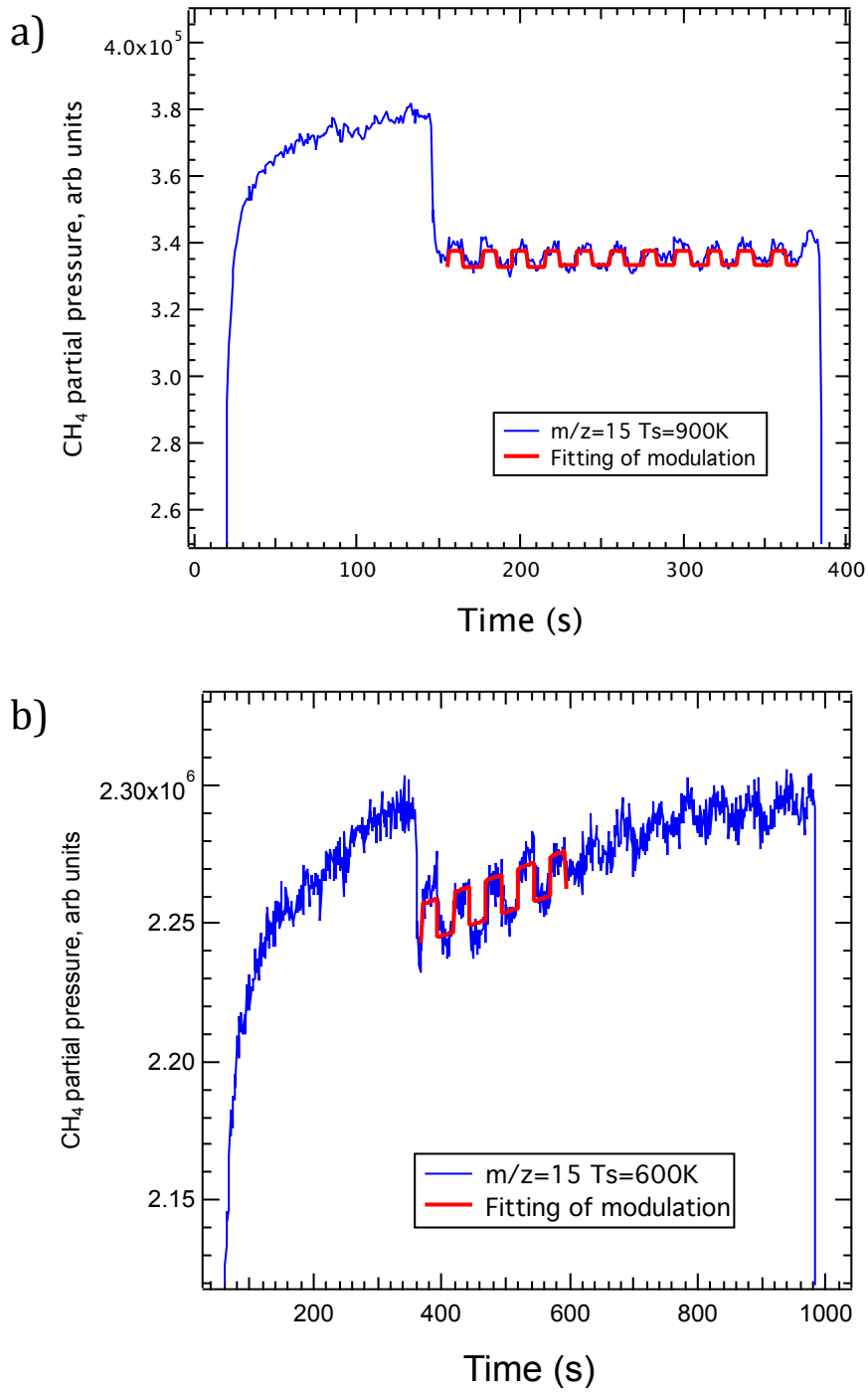

Figure 2.5 K&W laser modulation spectra at a) $T_{surface}$ = 900K and b) $T_{surface}$ = 600K. Dose condition: 1% CH_4 in H_2 at T_{nozzle} = 800K with IR excitation of the ν_3 (J=1) C-H vibration state.

Section 2.4 - Bulk H/D Titration

We use a special experimental method called bulk H/D titration to probe vibrational bond-selectivity in the dissociation of deuterated methane on Ni(111). This technique was initially developed by Ceyer group[18-21]. It employs subsurface H/D atoms (bulk H/D) as a reactant to provide isotope-specific detection. Bulk H/D atoms emerged from the bulk of crystal to the surface between 150K and 250K when the surface-bond methyl groups have not dissociated yet. Previous reports indicated that emerged bulk H atoms have more energy (~48 kJ/mol) than surface-bond H atoms due to the surface/bulk barrier.[22-24] The bulk H/D atoms emerge onto the surface with extra energy and can recombine with surface bond methyl groups to form methane, which desorbs after formation. This process can be expressed as Equation 2.3.

$$CH_3(ad) + H_{bulk} \rightarrow CH_4(g) \qquad \textbf{Eq. 2.3}$$

Surface-bond H/D atoms do not recombine with methyl groups on the surface since dehydrogenation is energetically preferred to the recombination with surface methyl.[21, 25, 26] Therefore, bulk H or D provides a clean method for tagging the methyl reaction products with an H atom (or D atom). Mass spectral analysis of the desorbing methyls permits an unambiguous identification and quantification of the isotopic identity of the methyl reaction products.

In experiments, bulk H/D titration requires a clean surface with sufficient bulk H/D underneath. We use a standard procedure to prepare such a surface.[2] In brief, we

use a hot filament to first dose H or D atoms on the Ni surface at $T_{surface} \leq 140K$. The atoms both adsorb to the surface and absorb into the subsurface region of the Ni crystal to produce bulk H/D in the crystal. Then we treat the surface with a process called collision-induced recombinative desorption (CIRD) to remove excessive H/D atoms on the surface. CIRD is a process using a high-energy Xe beam (0.25% Xe in He with T_{nozzle}=1040K). The beam impinges on the surface at 45° from surface normal. The impact of Xe atoms induces the surface-bond H/D atoms to recombine and desorb as H_2 or D_2,[27] which results in a clean surface for the subsequent methane dose.

As the setup was reassembled recently including a new home-made front filament, we did a series of diagnostic experiments to find the optimized conditions for the experiment. First, we examined voltage applied on the front filament, which produces energetic H/D atoms from backfilled 4×10^{-5} Torr H_2 or D_2 to the surface. The voltage across the filament has to be high enough to heat the filament to break H-H or D-D bonds but not so hot that it warms the crystal above 140K where subsurface H/D begins to diffuse to the surface. A comparison of different voltages is shown in Figure 2.6 a). Second, the dose-time of H_2/D_2 needs to be calibrated in order to make enough bulk H/D without affecting the efficiency of experiments. Through the comparison as shown in Figure 2.6 b), we choose 10 minutes as the optimized dosing time for H_2/D_2 doses.

Conditions of the CIRD process also affect the experiment. It is important that CIRD removes the full ML of surface-bound H or D from the surface so there is minimal H or D remaining on the surface to block CH_4 dissociation. Figure 2.7 a) shows H_2 TPD spectra with different lengths of CIRD. We find no obvious change in the H_2 TPD spectra after the length of CIRD increased to 40 minutes. That indicates that 40 minutes of CIRD under these conditions is sufficient to remove the full surface-bound ML. We also changed the nozzle temperature used in the CIRD to 1040K. Figure 2.7 b) shows that this higher temperature, which increases the energy of the Xe atoms, is more efficient at removing H than the previously used 1000K beam. Last, the crystal temperature has to below 140K in order to keep the H/D atoms kinetically trapped in the crystal bulk.[21] This requires an optimized distance between the front filament and the crystal corresponding to the filament used and the voltage applied on the filament. For current setup, the distance between filament and crystal is 0.6 inch.

After the methane dose, we use TPD to distinguish C-H or C-D cleavage on the surface. As shown in Equation 2.4 and 2.5, different types of cleavage result in different desorption channels.

$$CH_2D(ad) + D_{bulk} \rightarrow CH_2D_2(g) \qquad \textbf{Eq. 2.4}$$

$$CHD_2(ad) + D_{bulk} \rightarrow CHD_3(g) \qquad \textbf{Eq. 2.5}$$

Figure 2.8 shows a sample TPD spectrum from the dissociation of CH_2D_2 on Ni(111) with bulk D titration. In this experiment, a clean surface ($T_{surface}$ = 95K) with bulk D

was dosed with 3% CH_2D_2/He at T_{nozzle} = 675K for 300 seconds. There are two desorption features on *m/z=4* (D_2) trace in Figure 2.6. A peak centered at 210K is from the bulk D emerging onto the surface and recombinatively desorbing after saturating the surface with D atoms. Once all bulk D is depleted, this peak decreases toward baseline. The other peak at 350K is due to the recombinatively desorption of the remaining surface-bond D. As shown in Figure 2.8, CHD_3 desorbs around 185K as a sharp peak on the trace of *m/z=19*, correspondingly, peaks at same temperature on *m/z=16* to 18 traces are ionization fragments of *m/z=19*. More details of the bulk H/D titration will be explained in Chapter VI.

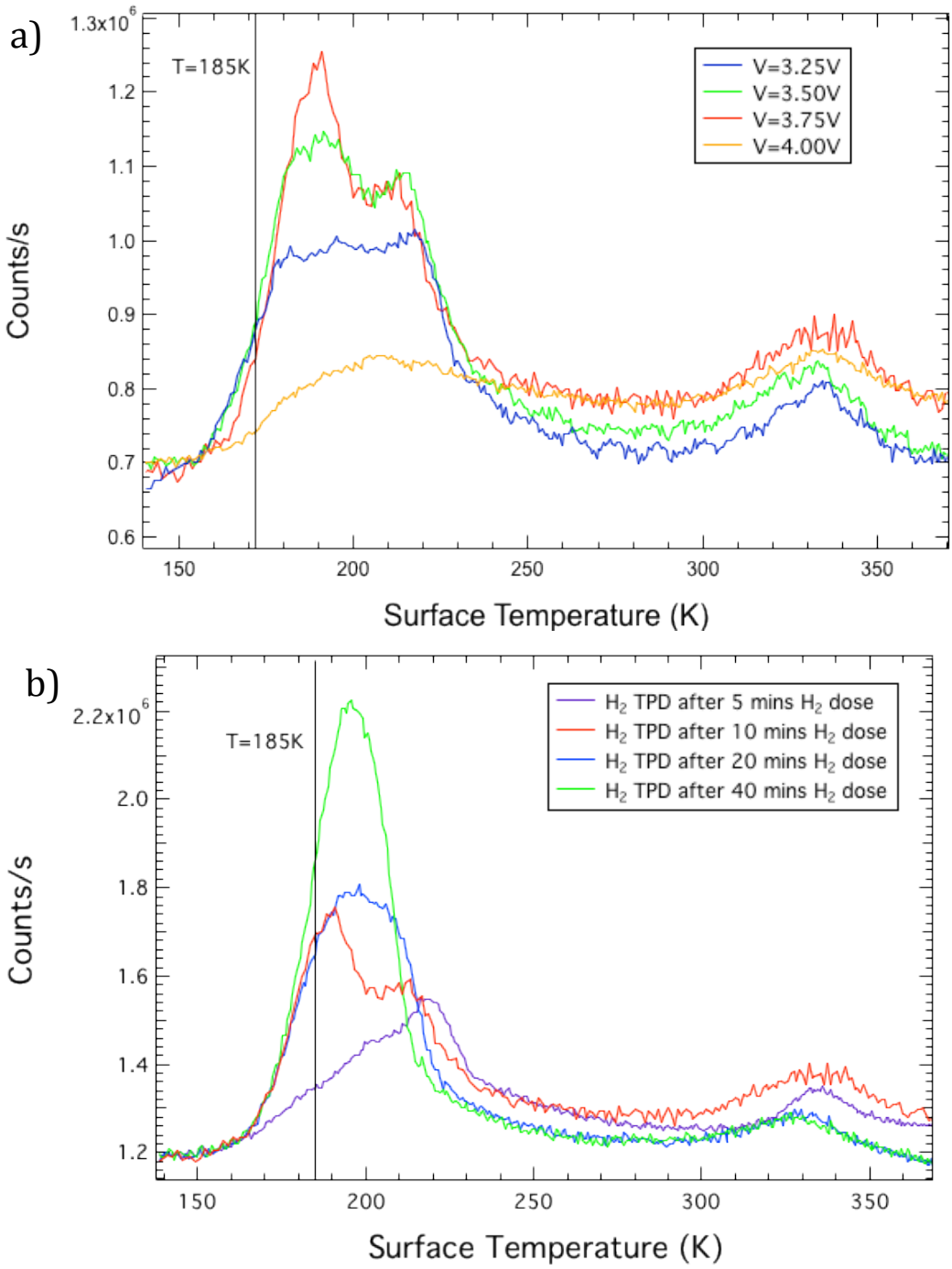

Figure 2.6 a) H_2 TPD spectra after H_2 doses with different voltage applied on the filament; b) H_2 TPD spectra after H_2 doses with different dosing time. There is no obvious increase of H_2 desorption at 185K (the temperature for recombinative desorption of surface methyl and H) for H_2 doses more than 10 minutes.

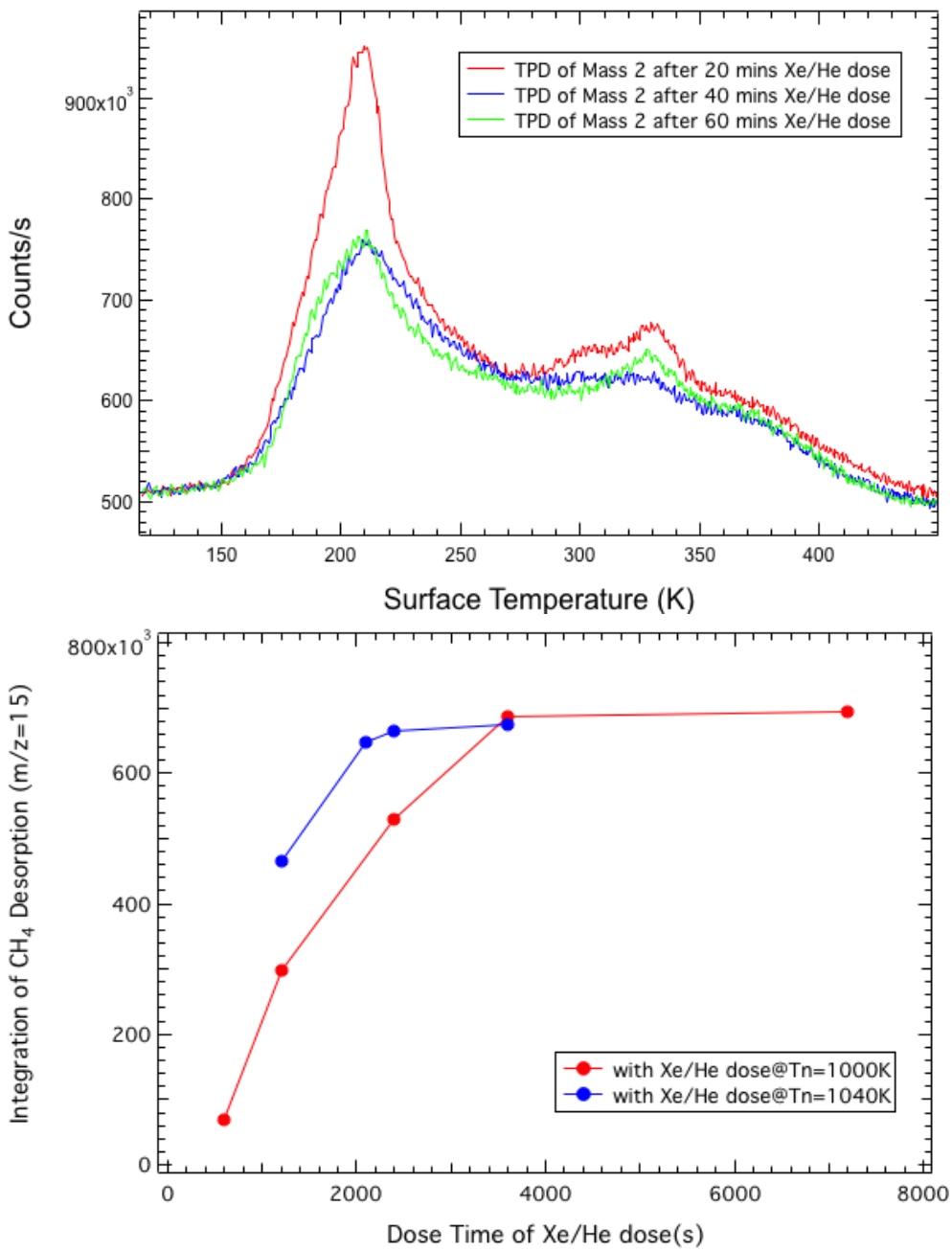

Figure 2.7 a) TPD spectra of mass 2 (H_2) after different length of CIRD. The comparison indicates the surface bond H atoms were removed completely after 40 minutes of CIRD; b) Comparison shows using 1040K nozzle is more efficient for CIRD process than the 1000K nozzle used before.

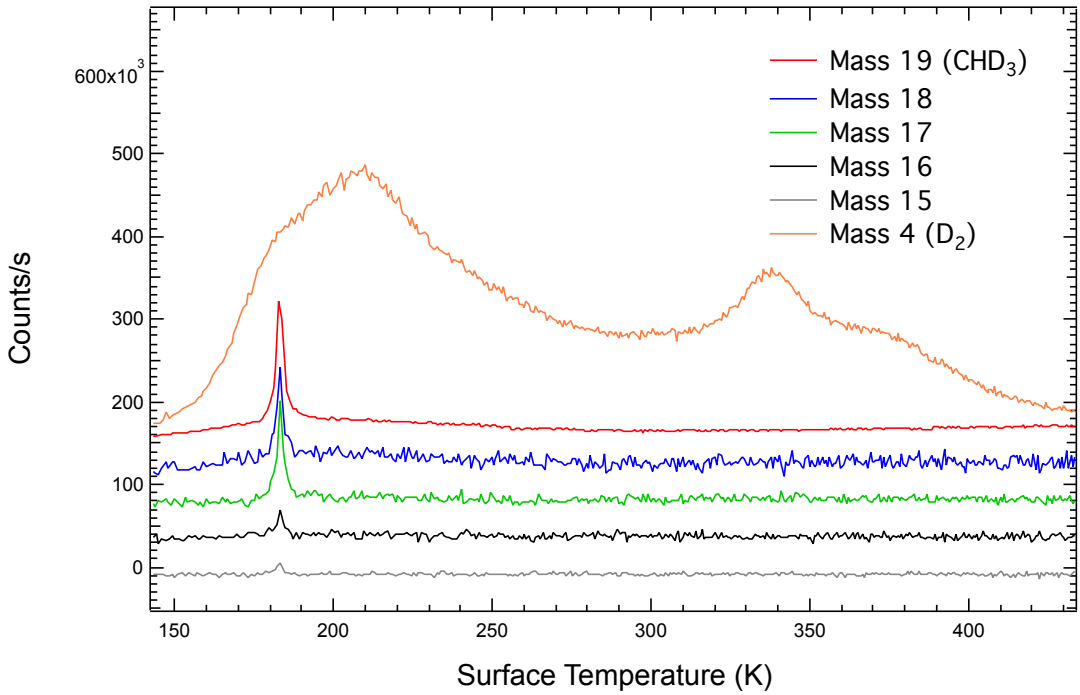

Figure 2.8 TPD spectrum of CH_2D_2 dissociation on Ni(111) with bulk D titration.

Section 2.5 - Overview of Laser System

The new laser system in our group was introduced before[1]. Compare to the old color-center laser system in our group,[2-4] the new system has a much larger power output and a improved stability. The central unit of this laser system is an Optical Parametric Oscillator (OPO) module and its control unit (made by Aculight, Model: 2400C). It produces widely tunable CW IR output (from 2500nm to 3300nm) with a significant amount of power (> 1W).

Optical Parametric Oscillation is a non-linear process in which a single laser beam ("pump" beam) is transformed into two lower-energy beams ("signal" and "idler" beam), which are both tunable. Equation 2.6 expresses the relationship between wavelengths of the three beams.[28]

$$\frac{1}{\lambda_{pump}} = \frac{1}{\lambda_{signal}} + \frac{1}{\lambda_{idler}} \qquad \textbf{Eq. 2.6}$$

Wavelengths generated by normal OPO devices are limited by the availability of non-linear materials that simultaneously satisfy energy conservation, phase matching, and optical transmission conditions. The wavelengths of such device are adjusted by angle or temperature tuning of refractive indices. This brings angular restrictions and walkoff, restricting the interaction length and reduces the efficiency of converting small pulse energy beams.[28] The OPO in our system uses Periodically-Poled Lithium Niobate (PPLN) that implements a nonlinear conversion process known as "quasi-phase matching", which does not rely on inherent material characteristics, to transform the signal and idler beams.[28] This technique eliminates

problems found in conventional techniques. The pump source in this OPO system is a CW Yb-doped fiber laser, operating at 1064nm wavelength with a bandwidth of <100kHz.[28] Its major advantage is the light entirely contained within the fiber and there is no chance to misalign the pump source. Thus, it can provide high power CW IR output with high reliability.

Tuning the wavelength of the OPO system can be achieved in three levels, coarse (10 to 20 nm), intermediate (~10 nm) and fine tuning (2~4 nm). Coarse control of the wavelength is performed using a fine-pitch screw accessed through crystal adjustment access hole on top of OPO module that adjusts the position of the OPO crystal, and thus the poling period, with respect to the pump beam. Changing crystal temperature can also be used to coarsely adjust the wavelength since it can modify the refractive indices of the material. But this adjustment also brings instability of the output wavelength, so it is rarely used. Intermediate tuning can be achieved by tuning the etalon, which is mounted on top of a galvanometer. Varying the applied voltage can vary the angle of the galvanometer, which allows the OPO output wavelengths to be varied over the free spectral range (FSR) of the etalon. From our experiences, improper angle of the galvanometer may result heating of the system, which brings instability and possible damage. Finest tuning of the wavelength is accomplished by tuning the wavelength of the pump source.[28] A piezo flexes the pump laser fiber and provides fine control over the pump laser frequency. In our set-up, this tuning process is controlled by LabVIEW based software, by which a 0~90V variable voltage is applied to the pump source seed PZT. Since the signal

beam frequency is resonant with a stabilized cavity in our laser, tuning the pump laser tunes the non-resonant idler beam, which we use in our experiments.

Figure 2.9 shows a schematic view of the updated assembly of the laser system including the OPO units. Comparing to the old color-center laser system[4], the laser diagnostics for the new system have been simplified because the Aculight etalon does not need to be synchronously tuned with the output frequency. This makes a lock-in feedback loop unnecessary for the intracavity etalon. As the assembly has been introduced before,[1] we only address changes made recently. First, a removable station with mirrors (as F in Figure 2.9) has been added into the laser path that can reproducibly introduce the laser to the other UHV chamber in our group without affecting the existing alignment. Second, a tunable wave plate (as E in Figure 2.9) has been added to the laser path. This provides a convenient means of varying laser power and permits more accurate and efficient measurements of the laser saturation curve. As the wave plate splits lights with different frequencies, the visible tracer beam provided by the OPO module is no longer overlapped with the invisible IR beam. This complicates IR laser alignment. In order to solve this problem, we use a visible He/Ne laser (as I in Figure 2.9) and finely adjusted its position to let it overlap with the IR beam in order to indicate the position of IR beam during the alignment. Besides these modifications, we also added small optics like focusing lens and irises to optimize the diameter and focusing properties of laser beam.

Our experiments require the IR laser to be single-frequency and stabilized for hours. It means we have to "lock" the laser to the frequency of the desired transition. Similar to the previous color-center laser system, the new laser system is frequency stabilized by a home-built, computer (via LabVIEW) controlled servo-loop with a temperature and pressure stabilized Fabry-Perot etalon as reference.[1-3] A beam splitter in the laser path splits a small portion of laser and directs it into the Fabry-Perot etalon, whose vacuum is maintained by a 20 L/s ion pump. Once the laser frequency is manually parked at the peak of an absorption feature in the controlling software, the Fabry-Perot's cavity length is tuned to cause constructive interference for transmission through the etalon. We put a small dither on the laser frequency, and use Lock-in amplifier (made by Stanford Research Systems, Model: SE530) to detect the derivative of the transmission signal. The servo-loop controlled by computer with a non-inverting operational amplifier tunes the voltage applied to the pump source PZT, so the output wavelength is finely tuned and keeps stable for a long time. Figure 2.11 shows a schematic view of the assembly of electronics used in this scheme. The home built non-inverting operational amplifier is capable of summing together the oscillating sine wave output from the lock-in (OSC), the digital-to-analog output (DAC) from the LabVIEW program and the 0~30V variable voltage (bias) to drive the pump source PZT. Figure 2.10 shows the design of the circuit.

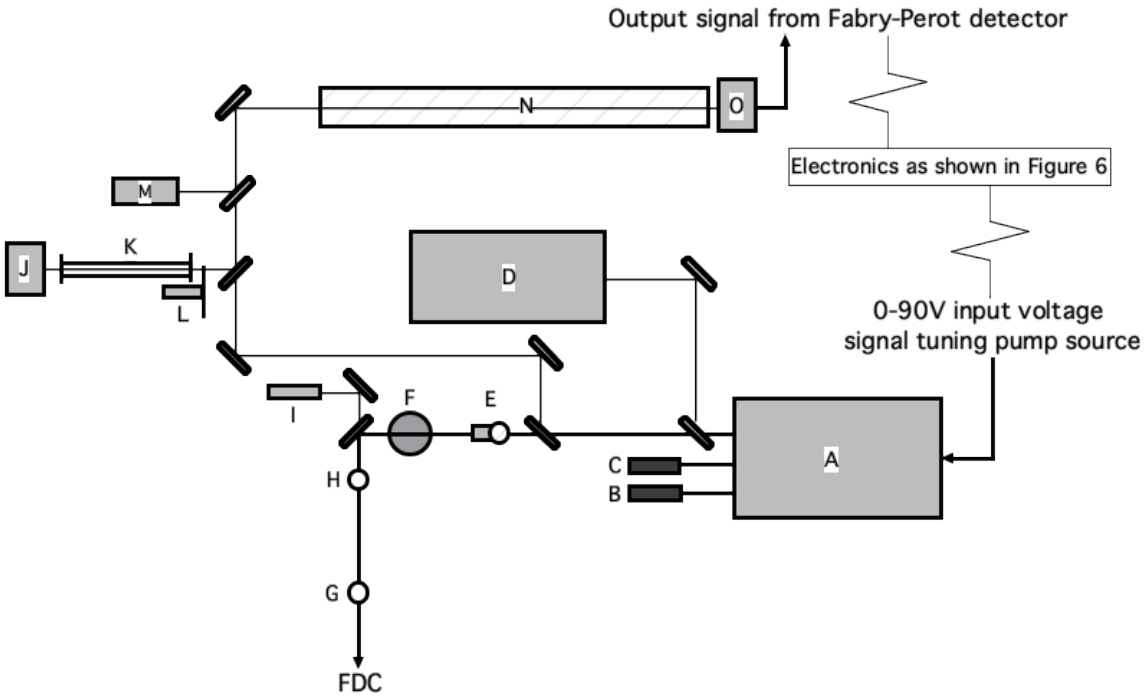

Figure 2.9 Schematic view of updated laser system: A) Aculight laser (OPO module and control unit); B) Beam dump for signal beam output; C) Beam dump for pump output; D) Wavemeter (Burleigh WA-10); E) Tunable wave plate; F) Movable station for introducing laser to another UHV chamber; G) and H) Irises; I) He/Ne laser; J) Reference cell detector; K) Reference cell; L) Beam chopper with tunable frequency; M) Spectrum analyzer; N) Fabry-Perot etalon; O) Fabry-Perot detector.

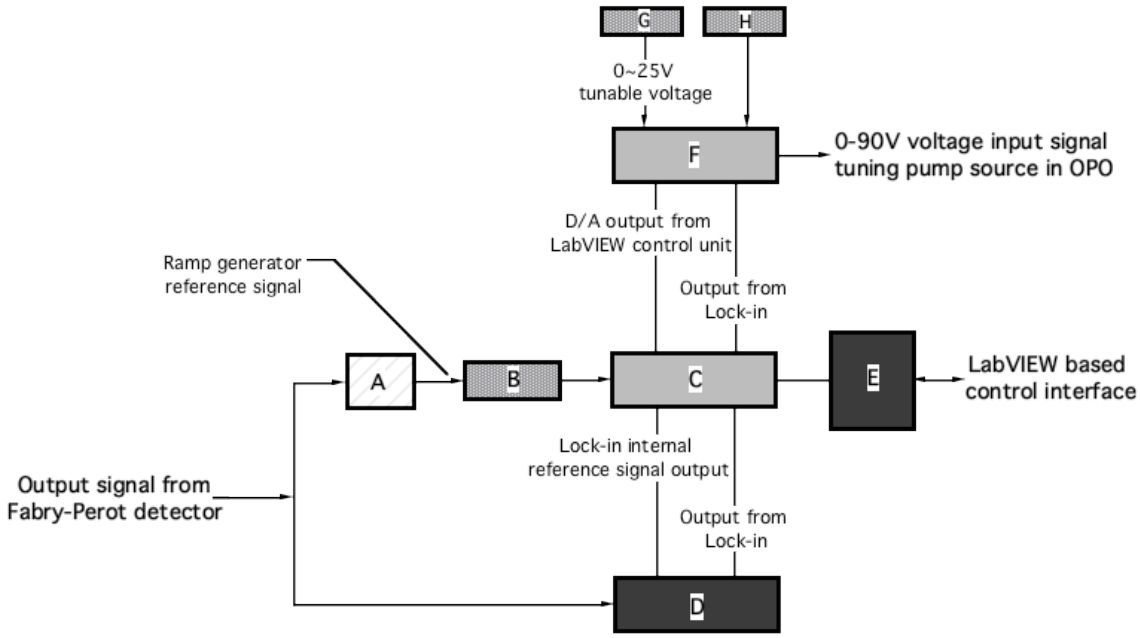

Figure 2.10 Schematic view of electronics used to lock the laser frequency: A) Oscilliscope; B) Ramp generator; C) Lock-in amplifier (Stanford Research Systems SE530); D) A/D converter (in computer); E) LabVIEW laser diagnose control unit (in computer); F) Non-inverting operational amplifier; G) Power supply (0-25 V tunable voltage); H) 15 V power supply.

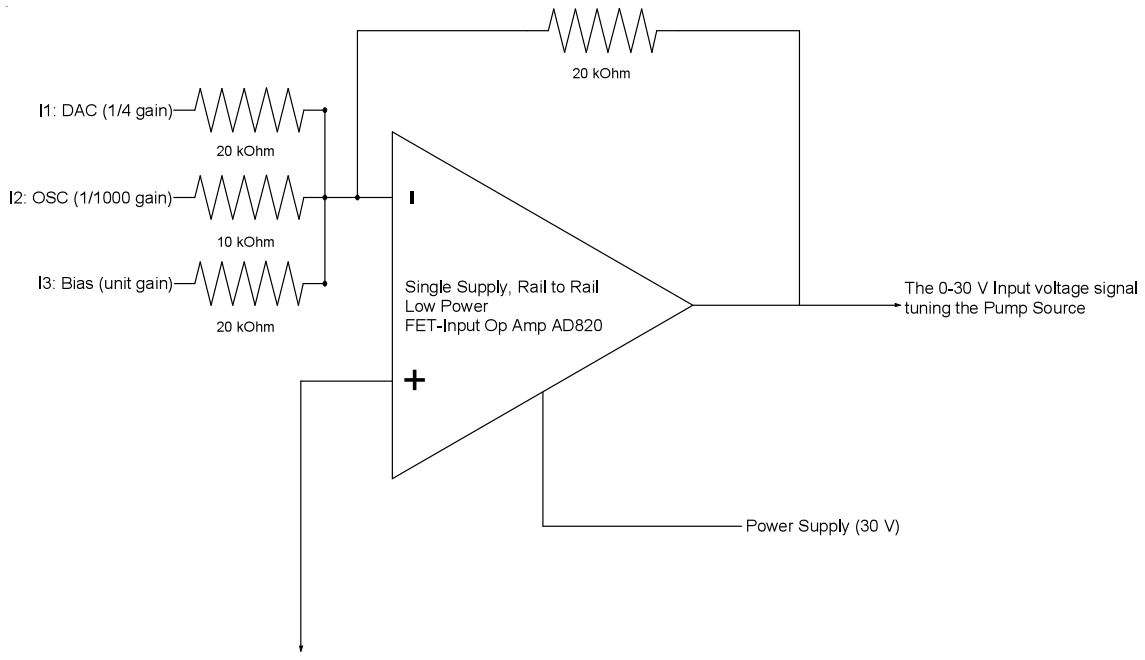

Figure 2.11 Schematic view of the non-inverting operational amplifier circuit.[1]

References

1. Campbell, V. L. State Resolved Measurements of Surface Temperature Dependence and Isotopically Selective Reactivity of Methane on Ni(111). Tufts University, Medford, 2011.

2. Killelea, D. R. Bond-Selective Control of a Gas-Surface Reaction. Tufts University, Medford, 2007.

3. Smith, R. R. Rovibrational State-Resolved Studies of Methane Dissociation on Ni(111). Tufts University, Medford, 2003.

4. Juurlink, L. B. F. Eigenstate-Resolved Measurements of Methane Dissociation on Ni(100). Tufts University, Medford, 2000.

5. P. R. McCabe, L. B. F. J., A. L. Utz, A Molecular Beam Apparatus for Eigenstate-Resolved Studies of Gas-Surface Reactivity. *Rev. Sci. Instruments* **2000,** *71*.

6. T. E. Gough, D. G., R. E. Miller, Multiple Crossing Devices for Laser-MOlecular Beam Spectroscopy *Rev. Sci. Instruments* **1981,** *52* (6).

7. J. C. Shelton, H. R. P., J. M. Blakely, Equilibrium Segregation of Carbon to a Nickel (111) Surface. Surface Phase Transition. *Surf. Sci.* **1974,** *43* (2).

8. J. H. Larsen, I. C., From fundamental studies of reactivity on single crystals to the design of catalysts. *Surface Science Reports* **1999,** *35*.

9. P. M. Holmblad, J. H. L., I. Chorkendorff, Modification of Ni(111) reactivity toward CH_4, CO and D_2 by two-dimensional alloying. *J. Chem. Phys.* **1996,** *104* (18).

10. G. Krishnan, H. W., INteraction of methane and carbon monoxide with oxygen adspecies on NI(111). *Appl. Surface Sci.* **1989,** *37*.

11. M. Valden, J. P., N. Xiang, M. Pessa, Influence of preadsorbed oxygen on activated chemisorption of methane on Pd(110). *Chem. Phys. Letters* **1996,** *257*.

12. F. Abild-Pedersen, O. L., J. Engbaek, G. Nielsen, I. Chorkendorff, J. K. Norskov, Methane activation on Ni(111): Effects of poisons and step defects. *Surf. Sci.* **2005,** *590*.

13. R. C. Egeberg, S. U., I. Alstrup, C. B. Mullins, I. Chorkendorff, Disscociation of CH_4 on Ni(111) and Ru(0001). *Surf. Sci.* **2002,** *497*.

14. Killelea, D. R. Bond-Selective Control of a Gas-Surface Reaction. Tufts University, Medford, 2007.

15. D. R. Killelea, V. L. C., N. S. Shuman, R. R. Smith, A. L. Utz, Surface Temperature Dependece of Methand Activation in Ni(111). *J. Phys. Chem. C* **2009,** *113*.

16. King, D. A.; Wells, M. G., Molecular beam investigation of adsorption kinetics on bulk metal targets: Nitrogen on tungsten. *Surface Science* **1972,** *29* (2).

17. Chen, N.; Huang, Y.; Utz, A. L., State-Resolved Molecular Beam Reflectivity Measurements of Methane Activation on Ni(111). *in preparation* **2013**.

18. A. D. Johnson, K. J. M., S. P. Daley, Q. Y. Yang, S. T. Ceyer, Hydrogen Embedded in Ni: Production by Incident Atomic Hydrogen and Detection by High-Resolution Electron Energy Loss. *Phys. Rev. Lett.* **1991,** *67* (7), 927-930.

19. Ceyer, S. T., The unique chemistry of hydrogen beneath the surface: Catalytic hydrogenation of hydrocarbons. *Accounts of Chemical Research* **2001,** *34* (9).

20. S. P. Daley, A. L. U., T. R. Trautman, S. T. Ceyer, Ethylene Hydrogenation on Ni(111) by Bulk Hydrogen. *J. Am. Chem. Soc.* **1994,** *116* (13).

21. A. D. Johnson, S. P. D., A. L. Utz, S. T. Ceyer, The Chemistry of Bulk Hydrogen-Reaction of Hydrogen Embedded in Nickel with Adsorbed CH_3. *Science* **1992,** *257* (5067).

22. Ceyer, S. T., New Mechanisms for Chemistry at Surfaces. *Science* **1990,** *249*.

23. Ceyer, S. T., The unique chemistry of hydroggen beneath the surface: Catalytic hydrogenation of hydrocarbons. *Accounts of Chemical Research* **2001,** *34* (9).

24. Sha, X. W.; Jackson, B., Ab initio and transition state theory studies of the energetics of H atom resurfaceing on Ni(111). *Chem. Phys. Lett.* **2002,** *357* (5-6).

25. Q. Y. Yang, J. K. M., A. D. Johnson, S. T. Ceyer, The structure and Chemistry of CH_3 and CH Radicals Adsorbed on Ni(111). *J. Chem. Phys.* **1995,** *109* (1), 7734-7749.

26. M. B. Lee, Q. Y. Y., S. L. Tang, S. T. Ceyer, Activated Dissociative Chemisorption of CH_4 on Ni(111): Observation of a methyl radical and implication for the pressure gap in catalysis. *J. Chem. Phys.* **1986,** *85* (3).

27. Johnson, A. D.; Daley, S. P.; Utz, A. L.; Ceyer, S. T., The chemistry of bulk hydrogen - Reaction of hydrogen embedded in Nickel with absorbed CH3. *Science* **1992,** *257* (5067).

28. *Argos Model 2400 CW OPO User Manual*. Aculight Corporation: Bothell.

Chapter III – Ground State Reactivity Modeling of CH_4 on Ni(111)

Section 3.1 - Introduction

In conventional beam–surface scattering techniques, gas-phase reagents have a well-defined translational energy and a narrow distribution of rotational states, but their vibrational state distribution remains nearly thermalized based on the nozzle temperature. This situation arises because collisional relaxation of vibrational states is typically much less efficient than rotational or translational relaxation.[1] There are too few collisions during supersonic expansion to support the extensive vibrational to translational energy transfer required for vibrational cooling. In the absence of vibrational cooling, the high vibrational state density of polyatomic molecules can result in hundreds, or even thousands of vibrational states contributing to the measured reactivity in beam-surface scattering measurements.

In this chapter, we explore how vibrational state averaging impacts conventional beam-surface scattering measurements of methane's dissociative chemisorption. Our approach relies on a detailed knowledge of the vibrational structure of methane, its vibrational cooling dynamics in a supersonic expansion, and an understanding of how individual vibrational states contribute to the state-averaged

reactivity. We obtain a much tighter upper limit for the state-resolved reactivity of the v=0 vibrational ground state. This state is the point of comparison we use to assess efficacy in all state-resolved beam-surface scattering measurements, and it is also the most common state modeled in computational studies. By examining the relative contribution of individual vibrational states to the thermal average, we also gain insight into the role that thermally excited vibrational states play in methane activation.

M. Lee et al.[2] from MIT first demonstrated that nozzle temperature can strongly affect methane reactivity on Ni(111). By varying the nozzle temperature and seed ratio of methane-helium gas mixes, they were able to prepare methane beams with the matching translational energy, but different vibrational temperatures. They used reactivity data from these beams to obtain an average value for vibrational enhancement based on the beam's calculated average E_{vib} content over the E_{trans} range of 58-69 kJ/mol. Expressed as a multiplicative enhancement, they predicted that S_0 would increase by a factor of 2.6 for every kJ/mol of E_{vib} present in the molecule. They then used this enhancement factor to adjust S_0 values measured with different T_{nozzle} and obtained a reaction probability curve more representative of a single nozzle temperature of 640K. Thus, data from Lee et al.[2] are not representative of ground state (v=0) methane.

In order to more accurately determine the ground state reactivity of methane and include contributions from individual quantum states, R. Smith[3] explored a

theoretical model including all vibrational states with energies below 16,000 cm^{-1}. State-resolved measurements of ν_3 dissociation on Ni(111) provided a characteristic shape for the sticking curve of an individual state, and the contribution of each state to the thermal average was obtained by first shifting the state's S_0 curve by an E_{trans} offset defined by its efficacy and then weighting that curve by its fractional population. The thermally averaged reactivity was obtained by summing the population-weighted sticking curves over all states. If one assumes same efficacy for all the states (statistical theory expectation), this model overestimates reactivity significantly, particularly at lower E_{trans}.

In this chapter, we will introduce the theoretical approach of this model and the new modification of using different offset for different vibrational modes. As well, our recently measurements of methane dissociative reactivity on Ni(111) with different seeding gas and nozzle temperatures allow us to model the vibrational-state-averaged beam-surface data to gain insight into how reactivity scales with increasing vibrational excitation.

Section 3.2 - Thermal distribution of vibrational states

Initially proposed by Lee et al.[2], people use four fundamentals (ν_1, ν_2, ν_3, ν_4) to account CH_4 vibrational states. Two of them are stretch vibrations (symmetric stretch, ν_1 and anti-symmetric stretch, ν_3), and the other two are bend vibrations (doubly-degenerate bend, ν_2 and triply-degenerate bend, ν_4). In supersonic expansion, vibrational cooling is not as efficient as rotational cooling. Thus, the vibrational-state distribution of CH_4 in a supersonic beam is nearly thermalized, and the population for each vibrational state can be estimated by its Boltzmann factor.[3] Our model describes the thermal distribution of CH_4 vibrations in supersonic expansion at certain nozzle temperature.

Lee et al. revealed an exponential dependence of CH_4 reactivity on vibrational energy.[4] By using a harmonic approximation, we can calculate the vibrational energy at certain nozzle temperature via Equation 3.1,

$$E_i = N_{i,\nu_1}E_{\nu_1} + N_{i,\nu_2}E_{\nu_2} + N_{i,\nu_3}E_{\nu_3} + N_{i,\nu_4}E_{\nu_4} \qquad \textbf{Eq. 3.1}$$

where E_{vi} is the vibrational energy of each fundamental mode,[5] and N_i are number of quanta in the particular state. In order to determine the average vibrational content (E_{vib}), we need to find the population-weighted contribution from every vibrational state. We first determine the degeneracy (g_i) of each vibrational state as described by Dennison[6] through Equation 3.2 to 3.5.

$$g_{v1} = 1 \qquad \textbf{Eq. 3.2}$$

$$g_{v2} = N_{v2} + 1 \qquad \textbf{Eq. 3.3}$$

$$g_{v3} = 1/2 \times (N_{v3}+1)(N_{v3}+2) \qquad \textbf{Eq. 3.4}$$

$$g_{v4} = 1/2 \times (N_{v4}+1)(N_{v4}+2) \qquad \textbf{Eq. 3.5}$$

Then, the total degeneracy for a particular vibrational state is given in Equation 3.6

$$g_i = g_{v1} \times g_{v2} \times g_{v3} \times g_{v4} \qquad \textbf{Eq. 3.6}$$

With its degeneracy, we can calculate the Boltzmann factor for the vibrational state (n_i) via Equation 3.7,

$$n_i = g_i \times \exp\left(\frac{-E_i}{kT_N}\right) \qquad \textbf{Eq. 3.7}$$

where E_i is the vibrational energy of the particular state, k is the Boltzmann constant, and T_N is the nozzle temperature (assume $T_{vib} \approx T_N$).

The partition function for all vibrational states (N_{total}) is the product of the partition functions of each normal mode (N_i) as shown in Equation 3.8.

$$N_{total} = N_{v_1} \times N_{v_2} \times N_{v_3} \times N_{v_4} \qquad \textbf{Eq. 3.8}$$

Smith found N_{total} could be estimated by the sum of Boltzmann factors for each state below 16,000 cm^{-1}, and the estimation shows an excellent agreement with a more complicated calculation via infinite series in harmonic approximation.[3] Thus, E_{vib} can be calculated via Equation 3.9,

$$E_{vib} = \sum_{i=0}^{i,16000cm^{-1}} \frac{n_i}{N_{total}} \times E_i \qquad \textbf{Eq. 3.9}$$

where n_i/N_{total} is the ratio of Boltzmann factor from the particular state to the sum of Boltzmann factors from all states below 16,000 cm^{-1}. Smith found 390 vibrational

levels, which, when accounting for degeneracies, corresponds to 23,884 distinct vibrational quantum states, below 16,000 cm^{-1}. We list the predominately populated states at T_N = 550K and 1050K in Table 3.1, and show the distribution in Figure 3.1.

In Figure 3.1, each line represents the population of a CH_4 vibrational state, and lines with similar energy cluster into groups with a significant energy gap from one to another. This is an important feature of methane's vibrational structure, which is called a polyad. The first polyad is composed of the two bending fundamentals ν_2 and ν_4, and is called the dyad near 1400 cm^{-1}. Bending overtones ($2\nu_4$, $2\nu_2$, and $\nu_2 + \nu_4$), and stretching fundamentals (ν_1 and ν_3) compose the second polyad, which is called the pentad near 2800 cm^{-1}. The pentad is the polyad that attracts most attention in the state-resolved reactivity studies of CH_4 on transition metal surfaces as its states contain significant E_{vib}, but also have appreciable population in beams with a mild T_N. Higher polyads appear above 4000 cm^{-1}.

There is a simple rule to predict which polyad a vibrational state belongs to. If the vibrational state has *b* bending quanta and *s* stretch quanta, then it belongs to the $(b+2s)^{th}$ polyad. In polyatomic molecules, when the energy gap between vibrational levels is larger than collision energies (ca. kT), the probability of vibrational-to-translational (V-T) energy transfer is quite low during supersonic expansion. [7] When the energy gap between states is smaller than kT, the probability of V-T energy transfer increases. This prediction is verified by Bronnikov et al., who qualified the vibrational state populations of CH_4 in supersonic beam via IR

absorption.[1] Within each polyad, the energy gaps between vibrational states are small and comparable to collision energies. So the interpolyad vibrational-to-translational energy transfer is quite possible. As a result, populations of individual states in the beam can be different from the prediction based on Boltzmann distribution at the nozzle temperature, but the overall population of each polyad remains same as the large energy gap between polyads results in minimal vibrational relaxation between states in different polyads. It is important to note that the model described above assumes a thermal distribution of vibrational states and ignores vibrational cooling within polyads, although the intrapolyad cooling observed by Bronnikov et al. could be included in subsequent models.[1]

Table 3.1 Fractional population of predominant states of CH_4 at 298K, 550K and 1050K

Vibrational states	**Fractional population (T_N = 298K)**	**Fractional population (T_N = 550K)**	**Fractional population (T_N = 1050K)**
v=0	9.93E-01	8.72E-01	4.19E-01
ν_4	5.38E-03	8.53E-02	2.09E-01
ν_2	1.20E-03	3.14E-02	1.02E-01
$2\nu_4$	1.94E-05	5.56E-03	6.97E-02
$\nu_2 + \nu_4$	6.47E-06	3.07E-03	5.11E-02
ν_1	7.51E-07	4.20E-04	7.68E-03
ν_3	1.35E-06	9.55E-04	1.99E-02
$2\nu_2$	1.08E-06	8.46E-04	1.87E-02
$3\nu_4$	5.84E-08	3.02E-04	1.93E-02
$\nu_2 + 2\nu_4$	2.33E-08	2.00E-04	1.70E-02
$\nu_1 + \nu_4$	4.07E-09	4.11E-05	3.84E-03
$\nu_3 + \nu_4$	7.30E-09	9.35E-05	9.95E-03
$2\nu_2 + \nu_4$	5.84E-09	8.28E-05	9.34E-03
$\nu_1 + \nu_2$	9.04E-10	1.51E-05	1.87E-03
$\nu_2 + \nu_3$	1.62E-09	3.44E-05	4.86E-03
$3\nu_2$	8.65E-10	2.03E-05	3.04E-03
$4\nu_4$	1.58E-10	1.48E-05	4.83E-03
$\nu_2 + 3\nu_4$	7.02E-11	1.09E-05	4.72E-03
$\nu_1 + 2\nu_4$	1.47E-11	2.68E-06	1.28E-03
$\nu_3 + 2\nu_4$	2.64E-11	6.10E-06	3.31E-03
$2\nu_2 + 2\nu_4$	2.11E-11	5.40E-06	3.11E-03
$\nu_1 + \nu_2 + \nu_4$	4.89E-12	1.48E-06	9.35E-04
$2\nu_1$	5.68E-13	2.03E-07	1.41E-04
$\nu_2 + \nu_3 + \nu_4$	8.79E-12	3.36E-06	2.42E-03

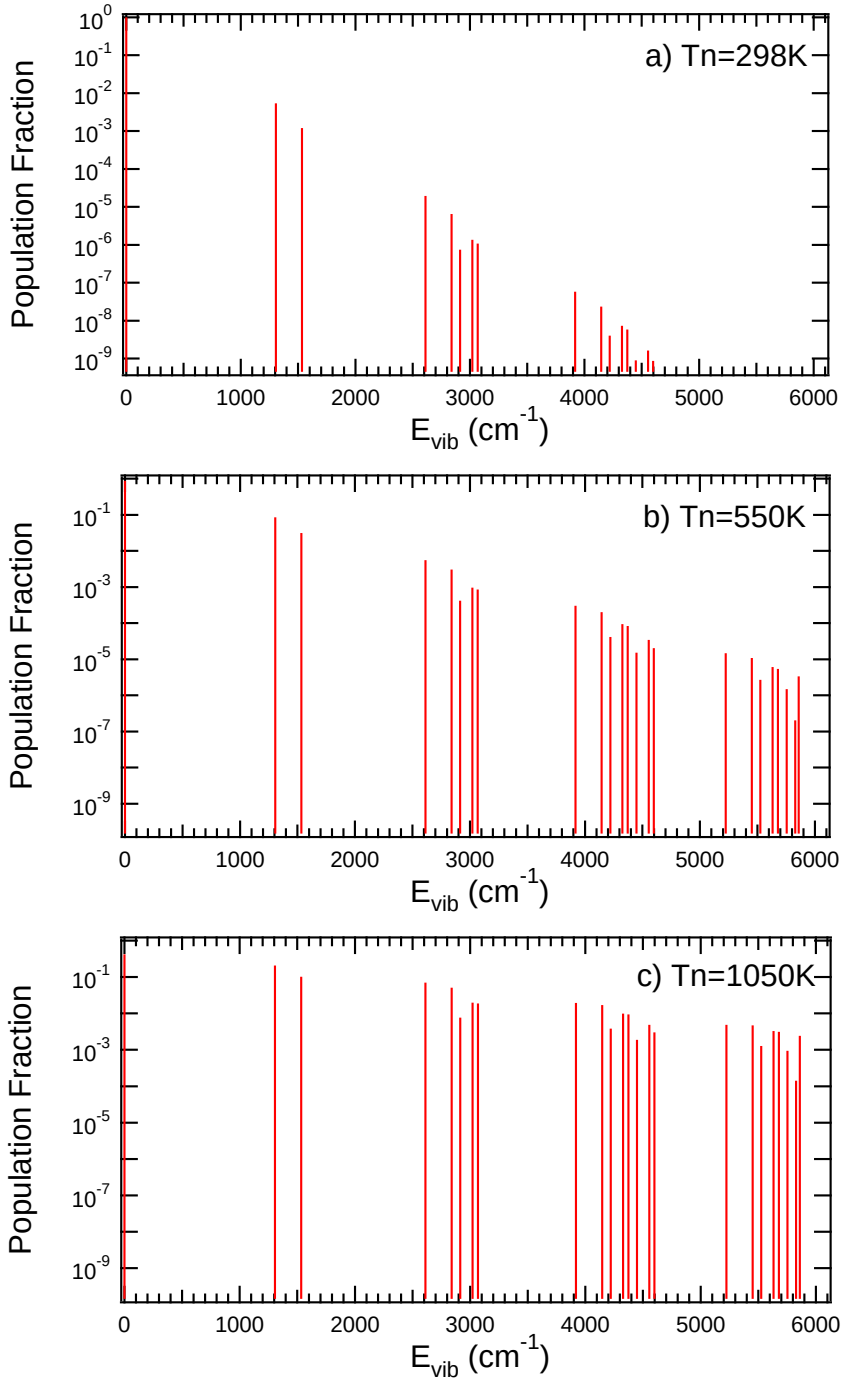

Figure 3.1 Thermal distributions of CH_4 vibrational states at a) T_N = 298K, b) T_N = 550 K, c) T_N = 1050 K

Section 3.3 - Quantifying reactivity of CH_4 on Ni and future work

Based on the ansatz of Michelson et al.,[8] we can use an error function to empirically fit the sticking probability data at certain nozzle temperature as Equation 3.10,

$$S_0(E_{trans}) = A\left[1 + erf\left(\frac{E_{trans} - M}{W}\right)\right] \qquad \textbf{Eq. 3.10}$$

where A is the asymptote, M is the midpoint and W is the width of the resulting 'S' curve. We can also use this empirical fit to predict the S_0 curve for a particular vibrational state as a function of E_{trans}. As mentioned earlier, vibrational states show a thermal (or near-thermal) distribution at a particular T_N. If we sum all S_0 curves from different vibrational states populated at a particular T_N, we can get a prediction for the S_0 curve of CH_4 reactivity at the selected T_N. In addition, experimental evidence[9,10,11,12] shows different vibrational modes have different efficacies to the overall reactivity. We applied different offsets ($v_1 > v_3 > v_4 > v_2$, as seen in Table 3.2) for different vibrational modes in predicting the S_0 curve. We list all parameters we used in current modeling including the different offsets for different vibrational modes in Table 3.2. Synthetic S_0 curves at different T_N are shown in Figure 3.2.

Table 3.2 Constants used in the current model

Name of Constant	Value
Energy of ν_1 (cm^{-1})	2914.2
Energy of ν_2 (cm^{-1})	1306.2
Energy of ν_3 (cm^{-1})	3020.3
Energy of ν_4 (cm^{-1})	1306.2
Asymptote of error function	0.5
Center of error function	16.264
Width of error function	97.488
Efficacy for ν_1 mode	1.40
Efficacy for ν_2 mode	0.40
Efficacy for ν_3 mode	1.25
Efficacy for ν_4 mode	0.72

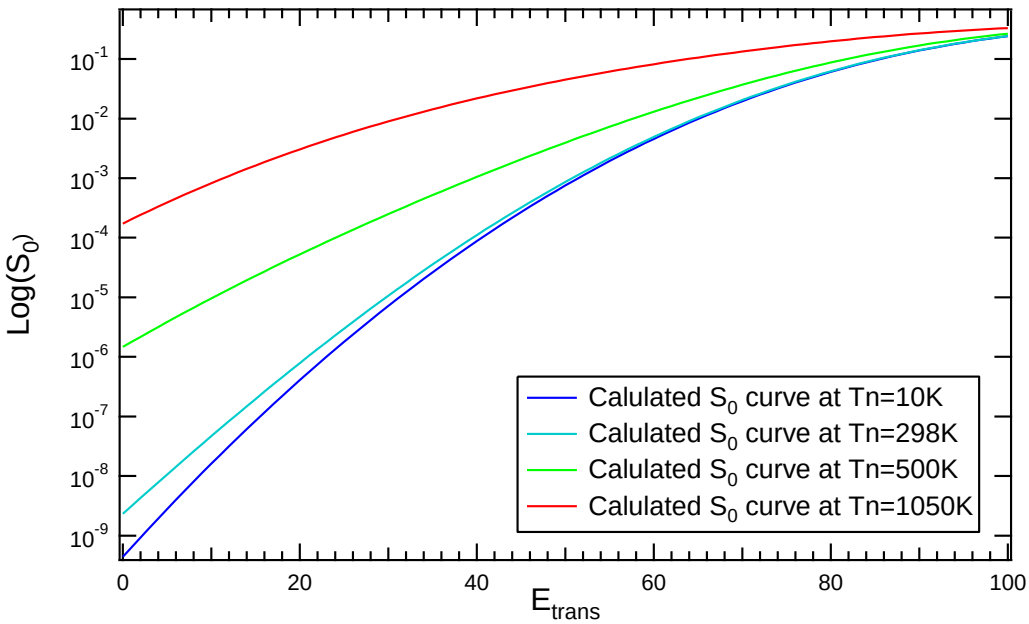

Figure 3.2 Calculated S_0 curves at different T_N

The ground-state (v=0) reactivity is an important quantity in the calculation of state-resolved reactivity as shown in Equation 3.11.

$$S_0^v = \frac{S_0^{LaserOn} - S_0^{LaserOff}}{f_{exc}} + S_0^{v=0} \qquad \textbf{Eq. 3.11}$$

In order to access high translational energy we usually need to increase T_N in experiments. In Figure 3.2, we can see dramatic changes of S_0 curves at different T_N since contributions from excited states that became more and more significant in the low E_{trans} region. In order to exclude the effects from contribution of exited states, we seek a method to estimate $S_0^{v=0}$, especially at high T_N, based on an understanding of how individual vibrational states contribute to CH_4 dissociation on Ni(111).

The overall S_0 at certain T_N ($S_0^{T_N}$) can be thought as the sum of S_0 from ground state (v=0) and S_0 from excited states (v>0) as shown in Equation 3.12,

$$S_0^{T_N} = \sum_{v\geq 0} f_v^{T_N} S_0^v = f_{v=0}^{T_N} S_0^{v=0} + \sum_{v>0} f_v^{T_N} S_0^v \qquad \textbf{Eq. 3.12}$$

where S_0^v represents sticking probabilities from vibrationally excited states at the particular T_N. Since at high E_{trans} many vibrationally excited states have a reactivity given by the asymptotic portion of their S_0 curve, it may be possible to approximate the reactivity of all excited states as a constant and approximate Equation 3.12 as Equation 3.13,

$$S_0^{T_N} \approx f_{v=0}^{T_N} S_0^{v=0} + f_{exc}^{T_N} S_0^v \qquad \textbf{Eq. 3.13}$$

which can also be expressed in following form,

Then, if we plot $S_0^{T_N} / f_{v=0}^{T_N}$ vs. $f_{exc}^{T_N}$ for data obtained at fixed E_{trans} but differing T_{nozzle}, as shown in Figure 3.3, an extrapolation to $f_{exc} = 0$ would yield $S_0^{v=0}$. To test our approximation, we turn to the sum-of-states model of Table 3.2 and Fig. 3.2. When we use simulated data based on that model, we find that for $E_k > 50$ kJ/mol the plots are very nearly linear, which suggests we can get $S_0^{v=0}$ at different E_{trans} from this approach. This procedure appears to provides an accurate approach to obtaining $S_0^{v=0}$ and eliminating effects from vibrationally excited states in the beam.

It is important to note that data shown in Figure 3.3 are calculated S_0 curves from this theoretical model. In order to obtain the real ground-state reactivity, it is necessary to measure a series of S_0 at different T_N in experiments. In order to plot $S_0^{T_N} / f_{v=0}^{T_N}$ as a function of $f_{exc}^{T_N}$, like Figure 3.3, we need to measure 4 to 5 S_0 at each T_N for an accurate linear fit. We need different beam seeding to provide different E_{trans} at selected T_N. Once we measured experimental S_0, not only we can approach a more accurate ground-state reactivity in our state-resolved measurements, but also we will be able to compare the S_0 prediction from this theoretical model to experimental data, which provides the opportunity to improve the model. Current work to address this issue is being performed in our lab for T_N = 1000K, 900K, 800K, and 700K, and we expect to see a publication in the near future.

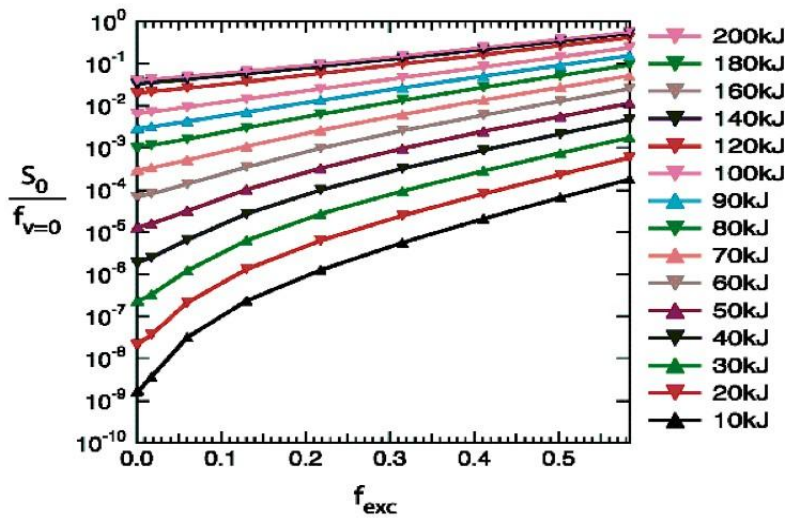

Figure 3.3 Synthetic data of S_0 as a function of f_{exc} at different E_{trans}

Reference

1. Bronnikov, D. K.; Kalinin, D. V.; Rusanov, V. D.; Filimonov, Y. G.; Selivanov, Y. G.; Hilico, J. C., Spectroscopy and non-equilibrium distribution of vibrationally excited methane in a supersonic jet. *Journal of Quantitative Spectroscopy & Radiative Transfer* **1998,** *60* (6), 1053-1068.

2. Lee, M. B.; Yang, Q. Y.; Ceyer, S. T., DYNAMICS OF THE ACTIVATED DISSOCIATIVE CHEMISORPTION OF CH4 AND IMPLICATION FOR THE PRESSURE GAP IN CATALYSIS - A MOLECULAR-BEAM HIGH-RESOLUTION ELECTRON-ENERGY LOSS STUDY. *Journal of Chemical Physics* **1987,** *87* (5), 2724-2741.

3. Smith, R. R. Rovibrational State-Resolved Studies of Methane Dissociation on Ni(111). Tufts University, Medford, 2003.

4. Lee, M. B.; Yang, Q. Y.; Tang, S. L.; Ceyer, S. T., ACTIVATED DISSOCIATIVE CHEMISORPTION OF CH4 ON NI(111) - OBSERVATION OF A METHYL RADICAL AND IMPLICATION FOR THE PRESSURE GAP IN CATALYSIS. *Journal of Chemical Physics* **1986,** *85* (3), 1693-1694.

5. Herzberg, G., *Molecular Spectra and Molecular Structure II: Infrared and Raman Spectra of Polyatomic Molecules*. Van Nostrand Reinhold: New York, 1945.

6. Dennison, D. M., The infra-red spectra of polyatomic molecules. Part II. *Reviews of Modern Physics* **1940,** *12* (3), 0175-0214.

7. Yardley, J. T., *Introduction to molecular energy transfer*. Academic Press: New York, 1980.

8. Michelsen, H. A.; Rettner, C. T.; Auerbach, D. J.; Zare, R. N., EFFECT OF ROTATION ON THE TRANSLATIONAL AND VIBRATIONAL-ENERGY DEPENDENCE OF THE DISSOCIATIVE ADSORPTION OF D(2) ON CU(111). *Journal of Chemical Physics* **1993,** *98* (10), 8294-8307.

9. Smith, R. R.; Killelea, D. R.; DelSesto, D. F.; Utz, A. L., Preference for vibrational over translational energy in a gas-surface reaction. *Science* **2004,** *304* (5673), 992-995.

10. Juurlink, L. B. F.; Smith, R. R.; Killelea, D. R.; Utz, A. L., Comparative study of C-H stretch and bend vibrations in methane activation on Ni(100) and Ni(111). *Physical Review Letters* **2005,** *94* (20).

11. Maroni, P.; Papageorgopoulos, D. C.; Sacchi, M.; Dang, T. T.; Beck, R. D.; Rizzo, T. R., State-resolved gas-surface reactivity of methane in the symmetric C-H stretch vibration on Ni(100). *Physical Review Letters* **2005,** *94* (24).

12. Chen, N.; Huang, Y.; Utz, A., State-resolved reactivity measurements of CH_4 (v_2+v_4) on Ni(111). *Submitted* **2013**.

Chapter IV – Modified King and Wells reactivity modulation

Section 4.1 – Introduction

As a central area of heterogeneous catalysis, reactions at the gas-surface interface are an important topic for study. There have been many methods established during the past decades to probe the reaction probability of gas-phase molecules incident on and adsorbed to surfaces. The King and Wells (K&W) method was originally designed by D. King and M. Wells in 1972 to measure the absorption probability of N_2 on a tungsten surface.[1] It is an efficient method for quantifying reactivity in reactions with high sticking probability (≥ 1%). In K&W experiments, people use MS to monitor the partial pressure change of the reactant while dosing, so no post-dose measurements and calibrations are required. Quantitatively, it can be expressed as Equation 4.1,

$$S_0 = \frac{P_2 - P_1}{P_2} = \frac{Drop}{Maximum - Baseline} \qquad \textbf{Eq. 4.1}$$

where P_1 and P_2 are indicated in Figure 4.1. Another advantage is that the method provides absolute reaction probability without need for calibration measurement.

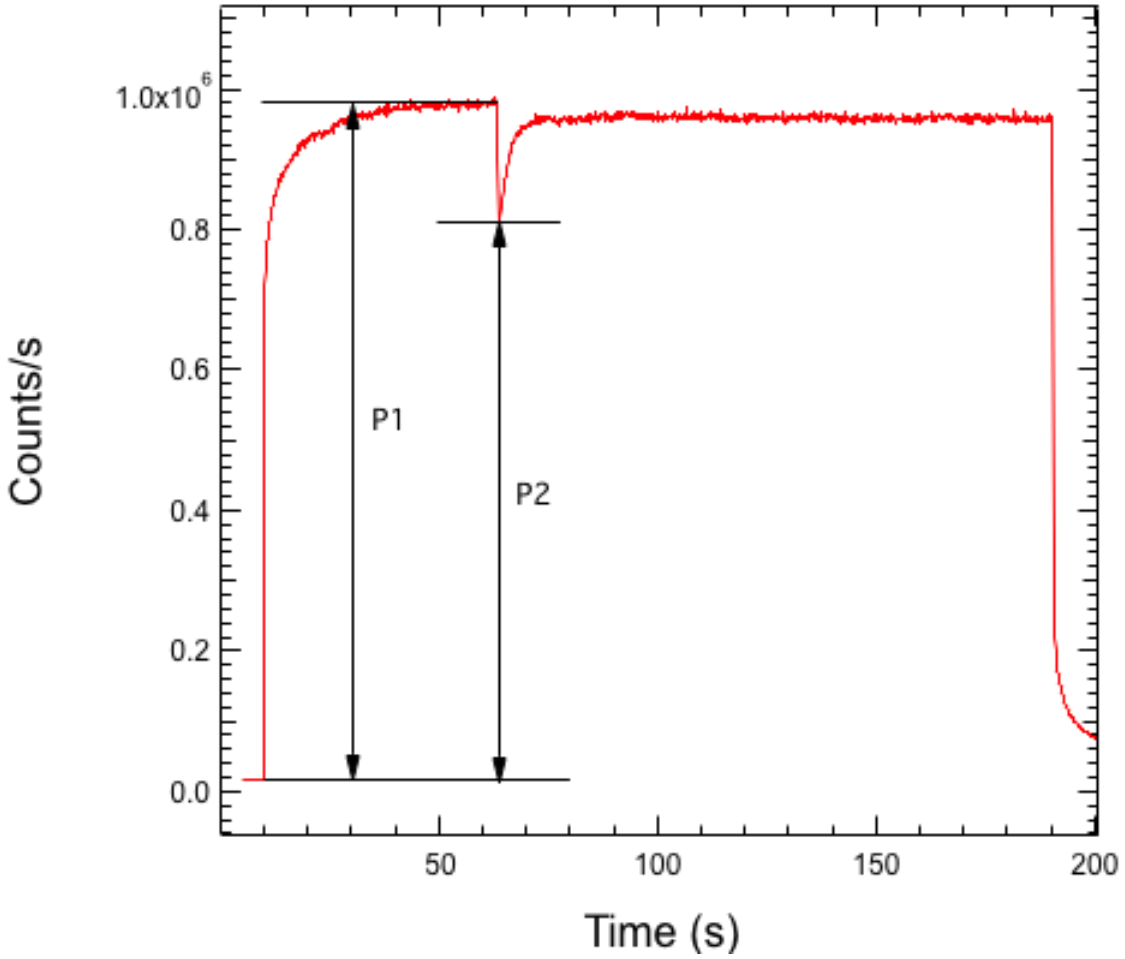

Figure 4.1 Sample spectrum of King and Wells measurement

The key measureable in state-resolved reactivity measurements is the difference in reaction probability with and without laser excitation, as shown in Equation 4.5. Measuring this difference directly, rather than independently measuring reactivity with and without laser excitation and calculating the difference between these quantities, is always desirable in measurements of state-resolved reactivity. Firstly, it will drastically reduce the experimental time. Secondly, errors are reduced in the calculation of state-resolved reactivity if the experimental condition for laser-on and laser-off measurements are exactly the same. However, it is not easy to achieve. It needs real-time detection since both laser-on and laser off measurements lead to the same surface-bound product. Temporally modulating the excitation laser and measuring resulting change in non-reactively scattered methane molecules provides a means of doing so. Here, we describe this method to measure the state-resolved reactivity in a single measurement, and we demonstrate it for measurements of state-resolved reactivity of CH_4 (ν_3) on Ni(111). We perform one set of measurements under conditions that also permit conventional AES-based measurements of product yield and reaction probability and compare the modulation method with previously published data. After validating the method, we obtain state-resolved reaction probabilities at a high surface temperature where the short lifetime of surface-bound carbon precludes conventional AES-based methods of detection.

This new scheme to detect state-resolved reactivity is based on the K&W method. We monitor the partial pressure change of CH_4 during the reaction and modulate laser excitation using a frequency-controlled shutter placed in the laser beam line. By doing so, laser-on and laser-off reactivity is measured in a square-wave form with the frequency set by a generator. The height of the square-wave modulation of methane partial pressure in the chamber gives the difference in reactivity with and without laser excitation, which is the key component required for calculating the state-resolved reactivity.

This detection scheme not only provides key advantages of K&W method, such as efficiency, real-time detection, and an absolute measure of reaction probability, but also extends measurements of state-resolved reactivity to a wider range. For example, some adsorbents are not stable on a high-temperature surface. They may dissociate and diffuse into the bulk of the crystal or desorb as different chemical species, where they cannot be 'seen' in post-dose measurements. Now the new K&W scheme makes it easier to measure the reactivity in such systems, and expands the range of experimental conditions accessible to state-resolved measurements.

In this chapter, the details of new K&W scheme will be addressed. We validate this new method by comparing its results with well-established post-dose measurements, which took much longer to acquire. In addition, we discuss problems encountered and plans for the future of this promising method.

Section 4.2 – Experimental details

We performed experiments in our differentially pumped beam-surface scattering apparatus, which has been introduced in Chapter II and elsewhere[2-5]. Here, we summarize key details and highlight the new detection scheme.

We used a beam with 1% CH_4 seeded in H_2 (both gases from Airgas, Inc. with a purity of 99.99% and 99.9999%, respectively). The beam expanded continuously and supersonically through a temperature-controlled nozzle into a high vacuum chamber. A continuous wave (CW), single frequency infrared (IR) laser intersected the molecular beam in the first stage and excited a fraction of CH_4 molecules to J=1 state of the anti-symmetric C-H stretching vibration (ν_3) via the R(1) transition at 3038.5 cm^{-1}. A shutter in the laser path chopped the laser at a typical frequency of 0.4 Hz, which produces laser modulation in square-wave form as shown in the top panel of Figure 4.2. We quantify the IR absorption of CH_4 molecules with a pyroelectric detector (PED) translated into the molecular beam path in the second stage, and the fraction of excited molecules (f_{exc}) measured is listed in Table 4.1, which will be explained in detail in Section 4.3.

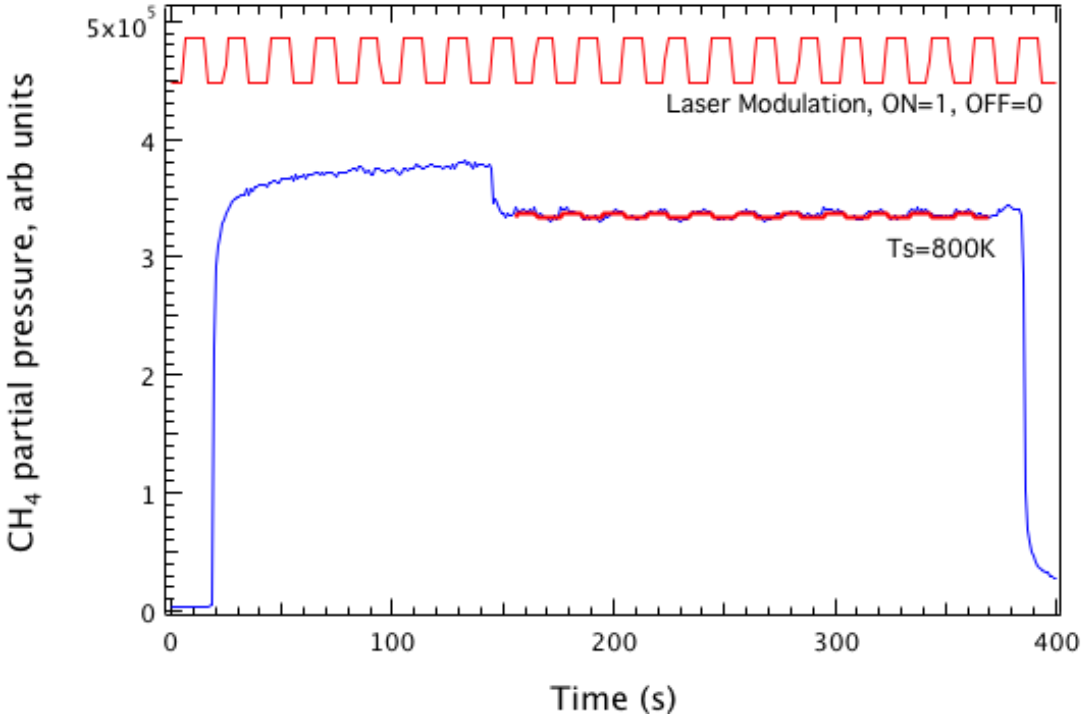

Figure 4.2 Mechanism of molecular beam reactivity modulation: K&W signal trace (m/z=15) has been modulated with laser on and off. The height of modulation represents the reactivity differences between laser on and laser off dose

Table 4.1 f_{exc} of CH_4 (ν_3) excitation at different nozzle temperatures

T_N	Beam	f_{exc} (%)
550K	1% CH_4/H_2	17.2±1.3
600K	1% CH_4/H_2	16.2±2.5
700K	1% CH_4/H_2	15.2±2.7
800K	1% CH_4/H_2	11.5±2.4

The triply differentially pumped molecular beam impinged on a Ni(111) crystal housed in an ultra-high vacuum (UHV) chamber. Methane's long IR radiative lifetime and collision-free condition in the 1% mixture beam ensured that the optically excited molecules impinged on the surface in their initially excited state. Vibrational energy redistribution did not occur until methane began to experience the gas-surface interaction potential, typically a few hundred femtoseconds prior to reaction or non-reactive scattering. At surface temperatures (T_s) higher than 475K, dissociated H atoms recombine and desorb promptly as H_2, while C atoms diffuse into bulk of the crystal at temperatures above 600K. With laser modulation, CH_4 molecules with and without laser excitation alternatively impinge the surface at the frequency of the shutter, which produces a high-low-high trace of CH_4 partial pressure monitored by MS, as shown in the lower trace in Figure 4.1. The height between different laser-on and laser-off levels in the MS trace represents the difference of CH_4 reactivity with and without laser excitation ($S_0^{Laseron} - S_0^{Laseroff}$), which is the key quantity required to calculate the state-resolved reactivity.

Section 4.3 - Excitation of CH_4 into ν_3

An important parameter when calculating the state-resolved reactivity is the excitation factor (f_{exc}). Based on its definition, we can use equation 4.2 to express this important quantity.

$$f_{exc} = f_{pop} \times f_2 \qquad \textbf{Eq 4.2}$$

where f_{pop} is the fraction of all molecules in the beam that are in the ground rovibrational state of the desired transition, and f_2 is the fraction of those molecules that are pumped to the desired excited state, as measured with the PED.

A methane molecule has three distinct rotational symmetries which are described as A, E and F. Due to nuclear spin statistics, not all rotational species are present in each rotational level, especially for low angular momentum (J) levels. In the vibrational ground state, symmetry species A can populate levels J = 0,3,4, symmetry species F can populate levels J = 1,2,3,4, and symmetry species E can populate levels J = 2,4.[6-8] We find that in our supersonic expansions at low nozzle temperatures, the rotational cooling is complete. This means that the rotationally high J states will cool to lower J states within same nuclear spin symmetry, as the selection rule for collisional cooling does not allow for changes in the nuclear spin state of the molecule. Therefore, all rotational A species will cool to J = 0, E species will cool to J = 2 and F species would cool to J = 1.[9] Based on nuclear spin degeneracies and statistics, the ratio of A, E, and F will be 5:2:9 respectively. Thus,

under supersonic expansions, complete cooling will result in 9/16 of the methane molecules residing in J = 1 level. The extent of rotational and vibrational cooling plus this nuclear spin factor determines f_{pop}, the fraction of molecules in the ground state of the desired transition. When cooling is complete, f_{pop} = 9/16 for the v=0, J=1 transition we pump.

In this experiment, we measure f_{exc} based on the absolute value from the PED (as introduced in Chapter II). The bolometer in the PED uses $LiTaO_3$, which is a pyroelectric crystalline solid capable of measuring small changes in temperature. The PED is attached to a linear feedthrough that allows precise positioning of the detector in the center of the molecular beam. When measuring the PED value, the laser is chopped at a frequency of 4 Hz, which allows the use of a lock-in amplifier to filter noise and measure the IR absorption as a change in the internal energy of the molecular beam. When the laser is off resonance, modulating the laser has no effect on the internal energy of the molecules impinging on the pyroelectric detector and no signal is detected. When the laser is on resonance, the internal energy of the beam increases due to absorption of IR light and the resulting increase in vibrational energy content of molecules in the beam. The magnitude of the pyroelectric detector signal is proportional to the number of molecules excited. At low incident laser power, optical absorption increases linearly with increasing laser intensity. As the laser power increases, the absorption (PED) signal approaches an asymptotic value associated with optical saturation..

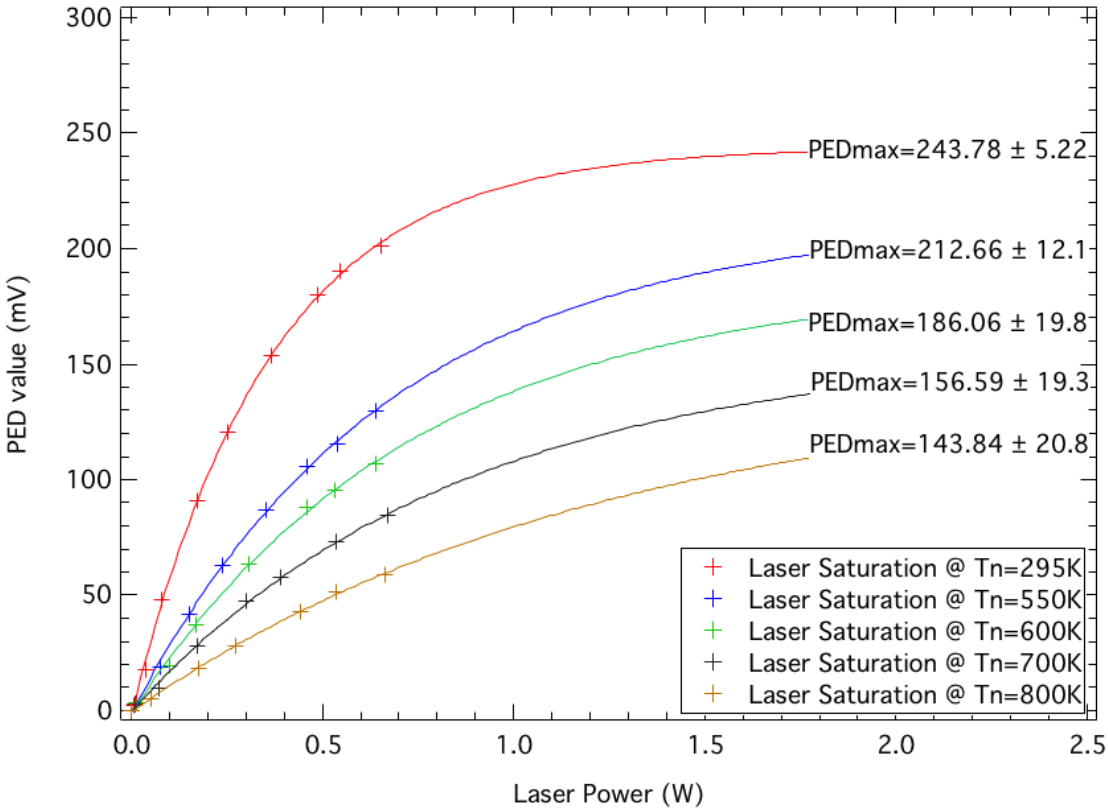

Figure 4.3 Laser saturation curve of 1% CH_4/H_2 beam at different nozzle temperatures.

Figure 4.3 shows laser saturation measurements for a 1% CH_4/H_2 beam at different nozzle temperatures. The value from PED, which indicates the fraction of CH_4 molecules in the desirable rovibrational ground state and the excitation fraction, changes with the nozzle temperature and the composition of molecular beam. The measurements of PED values with a series of laser power provide a valid way to probe f_{exc}. We can estimate f_{exc} using PED values (known as laser saturation measurements) as Equation 4.3.

$$f_{exc} = \frac{PED}{PED_{MAX}} \times \frac{9}{16} \times \frac{1}{2} \qquad \textbf{Eq. 4.3}$$

where PED_{MAX} is the asymptote from the fitting curve of sequential measurements over the range of experimentally accessible laser powers performed at a fixed nozzle temperature. The 9/16 term is the maximum population of CH_4 molecules in J = 1 if rotational cooling in the molecular beam was complete and the 1/2 term comes from $f_{2,\infty}$, which is the ratio of degeneracy of the upper state to the sum of the degeneracy of each state as expressed in Equation 4.4.

$$f_{2,\infty} = \frac{g_2}{g_1 + g_2} \qquad \textbf{Eq. 4.4}$$

For the ν_3 R(1) transition in methane, the effective degeneracy of the upper state is same as the initial state since only transitions with $\Delta M_J = 0$[1] are allowed in linearly polarized laser. Thus, $f_{2,\infty}$ equals 1/2. The f_{exc} at different nozzle temperatures are summarized in Table 4.1. Based on the well-established rovibrational knowledge of

[1] M_J is the projection of angular momentum vector, J, onto a fixed-space axis

CH_4, f_{exc} determined using PED values are proved to be a reliable measurement of ν_3 excitation fraction in CH_4.[10, 11]

Section - 4.4 Results and Discussion

In order to obtain state-resolved reactivity, the ensemble-averaged reactivity with and without laser excitation ($S_0^{LaserOn}$ and $S_0^{LaserOff}$, respectively) is measured. The sticking probability for a certain quantum state ($S_0^{\nu_3}$) is given by Equation 4.5.

$$S_0^{\nu_3} = \frac{\left(S_0^{LaserOn} - S_0^{LaserOff}\right)}{f_{exc}} + S_0^{\nu=0} \qquad \textbf{Eq. 4.5}$$

The sticking probability of the vibrational ground state ($S_0^{\nu=0}$) is often negligible due to the large enhancement in reactivity by laser excitation. Monitoring the partial pressure of CH_4 reflected from the surface while applying a square wave modulation to the laser permits a direct measurement of ($S_0^{Laseron} - S_0^{Laseroff}$). We fit the data in Figure 4.2 by an squarewave fitting program in Igor, which has been included in Appendix I.

Figure 4.4 shows the state-resolved reactivity of CH_4 (ν_3) on Ni(111) at T_s = 475K as a function of E_{trans} measured by the new scheme, as well as post-dose Auger electron spectroscopy (AES) measurements. The new K&W scheme and well-established post-dose S_0 measurements[12] show good consistency. More importantly, in contrast to weeks of experiments for a sticking curve via post-dose measurements, now only a few days are needed to obtain a similar sticking curve with the new K&W scheme.

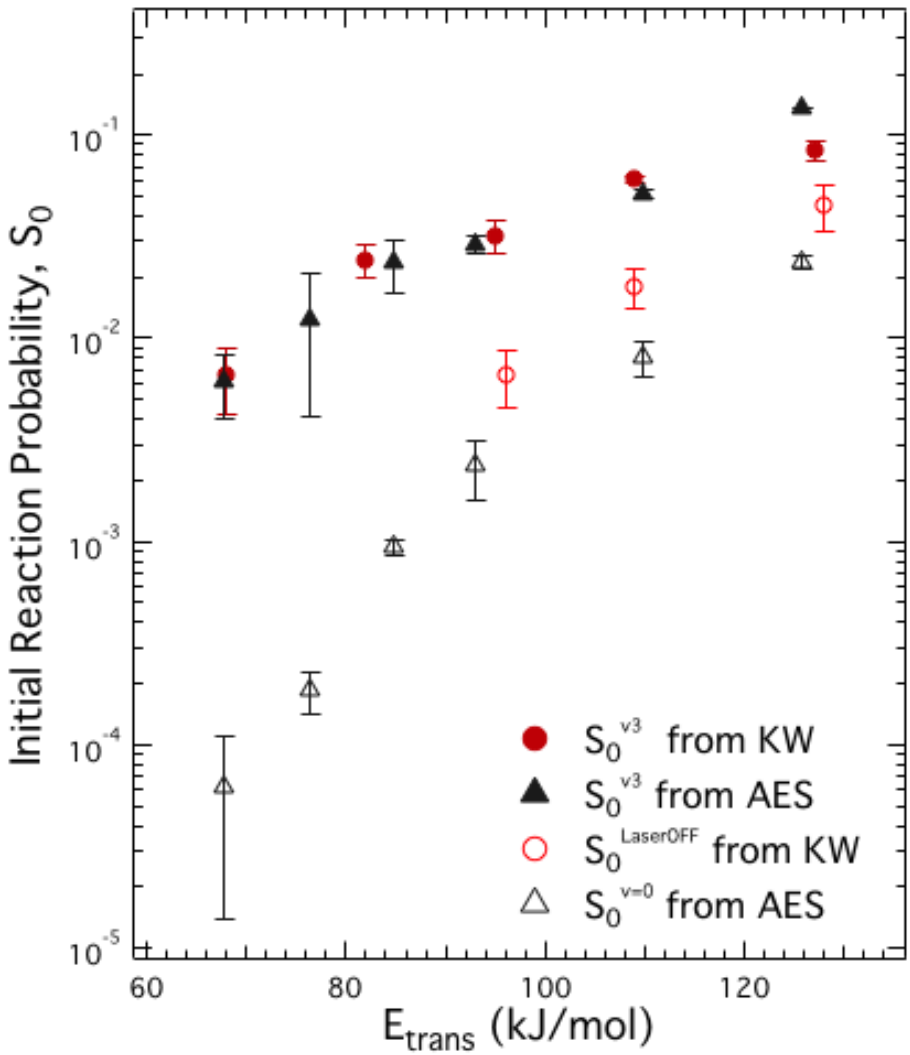

Figure 4.4 Comparison of S_0 from reflectivity measurement and traditional AES measurements[12]

Post-dose measurements quantify stable products resulting from the reaction studied. If products from the reaction are not stable enough to permit post-dose measurements, we are unable to obtain the sticking probability by traditional methods. As shown in Figure 4.5, our new scheme extends state-resolved measurements of CH_4 sticking probability on Ni(111) with surface temperatures as high as T_s = 800K, which could never be reached by post-dose measurements due to the diffusion of C into the bulk of the crystal. With the new K&W scheme, for the first time we are able to compare the state-resolved reactivity of CH_4 with elevated surface temperatures, which further confirms the trend of the surface atom motion effect to overall reactivity that was forecasted in both theoretical[13] and experimental[10] studies at lower surface temperatures.

In Figure 4.5, we find a 2-fold increase of S_0 at 800 K surface than that at 475 K surface when E_{trans} < 100 kJ/mol, whereas no increase for S_0 at a higher surface temperatures when E_{trans} > 100 kJ/mol. Campbell et al. found a significant surface temperature effect for CH_4 (ν_3) on Ni(111).[10] Now we can extend this trend to 800 K surface. At T_S = 800K, S_0 shows a different slop than the slop at T_S = 475K. It is consistent with theoretical models of surface temperature effects using electronic structure studies and quantum scattering by Nave et al..[14-19] The smaller slope of S_0 curve at T_S = 800K is due to abundant surface phonons, which reduce the effective barrier.

Moreover, the real-time information provided by the new K&W scheme can be used to monitor changes in reaction probability during the reaction. It reveals the coverage dependence of reactivity. When site-blocking effects are significant, this approach helps ensure that measurements are truly being made in the low-coverage limit. This new method also provides improved reproducibility of measured S_0. One of the major problems for post-dose S_0 measurement is that slight changes in experimental conditions from one experiment to the next can interfere with measurements when laser-on and laser-off measurements differ by a small amount. By continually recording the difference between these quantities, the effects of long-term drift can be minimized. In short, the reflectivity modulation measurements are less affected by changes of chamber condition from time to time, which is the main source of error in traditional post-dose methods.

Besides the unique advantages mentioned above, this method also has its limitations. First, as a method that quantifies reactivity as the difference between the incident and non-reactively scattered flux of molecules, it has a relatively high detection limit for sticking probabilities. It is hard to detect sticking probabilities lower than 0.5% via this scheme. Second, for lower surface temperatures where C diffuses into the bulk slower than CH_4 dissociates, the modulation feature is no longer in square-wave form. Instead, the adsorbed surface-bound C reaction products block surface sites and decrease the reaction probability as surface coverage increases, as shown in Figure 4.6. These data need to be fit to a model that includes the coverage-dependent effects of site blocking. Otherwise the difference

between laser-on and laser-off sticking probability will be underestimated. Finally, we noticed that cryopumping by the cold trap on the diffusion pump can damp rapid partial pressure changes and reduce the initial partial pressure drop in K&W measurements, which causes a smaller height of modulation and results in underestimating the state-resolved reactivity.

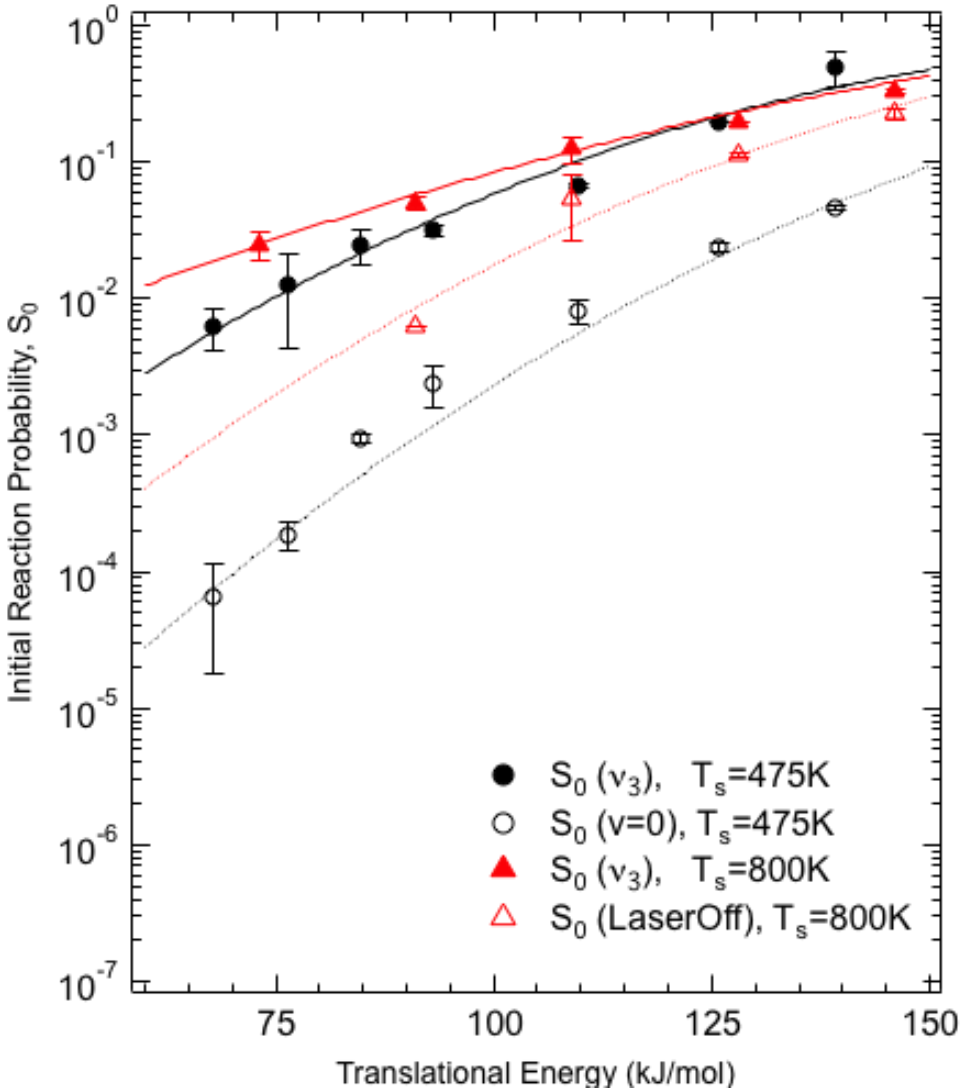

Figure 4.5 Reactivity of CH_4 (ν_3) dissociation on Ni(111) at T_s=800K, compared with reactivity of same reaction at T_s=475K

Section - 4.5 Conclusion and Future work

We described a real-time detection scheme for measuring state-resolved reactivity with significantly reduced experimental time and improved reproducibility. Its real-time detection permits us to extend state-resolved reactivity measurements to a wider range of experimental conditions, especially for reactions with unstable products that are impossible to measure by post-dose quantifications. With this new scheme, we can gain more insight into key features of energy flow during the methane activation on surfaces, and data to assess the generality of non-statistical behavior in gas-surface reactions.

As mentioned in Section 4.4, two factors have limited the widespread applicability of this approach, and addressing those factors will be a subject for future work. At lower surface temperatures, when the diffusion speed of carbon atoms is slower than the dissociation speed of $CH_4$the modulation feature shows a coverage-dependent decrease in reactivity that asymptotically approaches the signal for a non-reactive system. In such cases, our squarewave fitting on the modulation feature can significantly underestimate the state-resolved reactivity even if we fit only on the first couple of modulation features. In order to better account for this effect, we need a better modeling scheme that properly accounts for site blocking effects. We have begun using this model to fit the coverage dependence of measurements without laser modulation, and it works well, as shown in Figure 4.6

Reaction probability toggles between $S_0^{LaserOn}$ and $S_0^{LaserOff}$ with laser modulation, so the rate of C deposition changes as the laser is modulated. Properly accounting for site blocking in this situation requires a more sophisticated model, which will be developed in the future. We expect that using a turbomolecular pump on our main chamber during the K&W measurement will eliminate the effects of our liquid nitrogen trap and improve the time response of the molecular beam reflectivity traces.

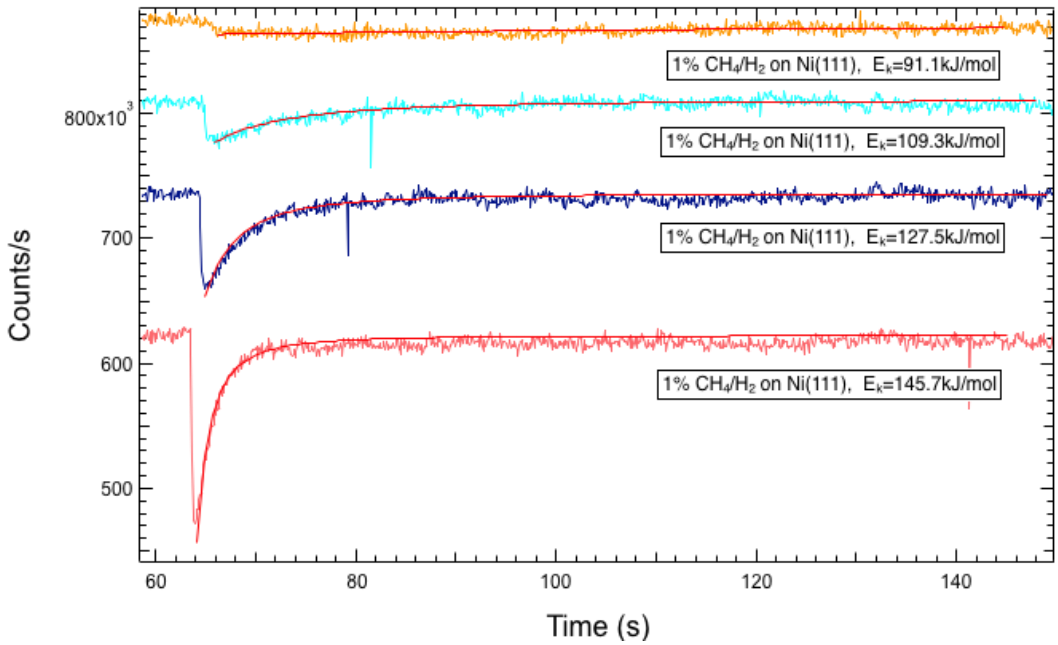

Figure 4.6 K&W spectra fittings by Langmuir site-blocking model.

Reference

1. King, D. A.; Wells, M. G., Molecular beam investigation of adsorption kinetics on bulk metal targets: Nitrogen on tungsten. *Surface Science* **1972,** *29* (2).

2. McCabe, P. R.; Juurlink, L. B. F.; Utz, A. L., A molecular beam apparatus for eigenstate-resolved studies of gas-surface reactivity. *Review of Scientific Instruments* **2000,** *71* (1), 42-53.

3. Juurlink, L. B. F.; Killelea, D. R.; Utz, A. L., State-resolved probes of methane dissociation dynamics. *Progress in Surface Science* **2009,** *84* (3-4), 69-134.

4. Killelea, D. R.; Campbell, V. L.; Shuman, N. S.; Utz, A. L., Bond-selective control of a heterogeneously catalyzed reaction. *Science* **2008,** *319* (5864), 790-793.

5. Killelea, D. R.; Campbell, V. L.; Shuman, N. S.; Smith, R. R.; Utz, A. L., Surface Temperature Dependence of Methane Activation on Ni(111). *Journal of Physical Chemistry C* **2009,** *113* (48), 20618-20622.

6. Wilson, E. B., Symmetry considerations concerning the splitting of vibration-rotation levels in polyatomic molecules. *Journal of Chemical Physics* **1935,** *3* (12), 818-821.

7. Wilson, E. B., The statistical weights of the rotational levels of polyatomic molecules, including methane, ammonia, benzene, cyclopropane and ethylene. *Journal of Chemical Physics* **1935,** *3* (5), 276-285.

8. Herzberg, G., *Molecular spectra and molecular structure*. 2nd ed.; Krieger Pub Co: 1991; Vol. 2, p 660.

9. McDowell, R. S., ROTATIONAL PARTITION-FUNCTIONS FOR SPHERICAL-TOP MOLECULES. *Journal of Quantitative Spectroscopy & Radiative Transfer* **1987,** *38* (5), 337-346.

10. Campbell, V.; Chen, N.; Utz, A. L., State Resolved Measurements of Surface Temperature Dependence in Methane Reactivity on Ni(111). *in prepapration*.

11. Campbell, V. L. State Resolved Measurements of Surface Temperature Dependence and Isotopically Selective Reactivity of Methane on Ni(111). Tufts University, Medford, 2011.

12. Smith, R. R.; Killelea, D. R.; DelSesto, D. F.; Utz, A. L., Preference for vibrational over translational energy in a gas-surface reaction. *Science* **2004,** *304* (5673), 992-995.

13. Henkelman, G.; Arnaldsson, A.; Jonsson, H., Theoretical calculations of CH4 and H-2 associative desorption from Ni(111): Could subsurface hydrogen play an important role? *Journal of Chemical Physics* **2006,** *124* (4).

14. Tiwari, A. K.; Nave, S.; Jackson, B., Methane Dissociation on Ni(111): A New Understanding of the Lattice Effect. *Physical Review Letters* **2009,** *103* (25).

15. Nave, S.; Jackson, B., Methane dissociation on Ni(111) and Pt(111): Energetic and dynamical studies. *Journal of Chemical Physics* **2009,** *130* (5).

16. Nave, S.; Jackson, B., Methane dissociation on Ni(111): The role of lattice reconstruction. *Physical Review Letters* **2007,** *98* (17).

17. Nave, S.; Jackson, B., Methane dissociation on Ni(111): The effects of lattice motion and relaxation on reactivity. *Journal of Chemical Physics* **2007,** *127* (22).

18. Tiwari, A. K.; Nave, S.; Jackson, B., The temperature dependence of methane dissociation on Ni(111) and Pt(111): Mixed quantum-classical studies of the lattice response. *Journal of Chemical Physics* **2010,** *132* (13).

19. Nave, S.; Tiwari, A. K.; Jackson, B., Methane dissociation and adsorption on Ni(111), Pt(111), Ni(100), Pt(100), and Pt(110)-(1x2): Energetic study. *Journal of Chemical Physics* **2010,** *132* (5).

Chapter V - State resolved CH_4 ($\nu_2+\nu_4$) reactivity on Ni(111)

Section 5.1 – Introduction

Supersonic molecular beams provide independent control over many factors affecting the reactivity in gas-surface reactions. For instance, people can access a wide range of well-defined translational energies (E_{trans}) in supersonic beams by varying molecular seed ratio and nozzle temperature (T_N). On the other hand, optical (vibrationally) excited molecules can play a central role in a gas-surface reaction. State-resolved reactivity measurements, a combination of supersonic molecular beam and state-selective optical excitation, can provide more details for dynamics of gas-surface reaction. They can reveal the mode-selective behavior of CH_4 dissociation on metal surfaces in which the identity of the vibrationally excited state, and not just the kinetic energy, dictates reactivity, and bond-selective behavior, where the nature of the vibrational excitation affects which bond breaks, and therefore the identity of reaction products.

Methane's dissociative chemisorption on metal surfaces is a benchmark system for this kind of study.[1-3] Understanding energy flow in this reaction has both

fundamental and practical impact as introduced in Chapter I. Earlier studies by Lee et al.[4] and Holmblad et al.[5] suggested the measured reactivity of CH_4 dissociation on Ni(111) and Ni(100) may be dominated by the reactivity from excited vibrational states when they demonstrated the strong effect of nozzle temperature on the overall reactivity. Recently, people reported several state-resolved reactivity measurements for CH_4 dissociation on Ni(111) and Ni(100).[6-8] These reports demonstrated that methane molecules prepared in excited vibrational states are more reactive than those in ground state. As a polyatomic molecule, methane has four distinct stretching and bending vibrations, which are named ν_1 (symmetric stretch) or ν_3 (anti-symmetric stretch) and ν_2 (doubly degenerate bend) or ν_4 (triply degenerate bend), respectively. Up to now, publications have reported state-resolved reactivity of CH_4 excited to ν_3, $2\nu_3$, and $3\nu_4$ vibrational states on Ni(111) in which most of them are stretching states. However, we still need direct evidence to further uncover the details in lower vibrational states and combinations of different vibrational modes. For example, a direct comparison between bending and stretching states in the same polyad (as introduced in previous chapters, CH_4 vibrational states group into polyads of similar vibrational energy) is still missing.

In this chapter, we are going to introduce our state-resolved reactivity measurements of methane (ν_2 + ν_4) on Ni(111) and quantify reaction probability (S_0) over a wide range of E_{trans}. In order to make a direct comparison between bending and stretching state in the same polyad, we compare our results with

published results of methane excited to anti-symmetric stretch (ν_3) and anti-symmetric bend ($3\nu_4$). The comparison confirms that the stretching vibration couples into the reaction coordinate more effectively than the bending vibration, and suggests that the doubly degenerate bending mode (ν_2) is less effective than the triply degenerate bend (ν_4) in promoting methane dissociative chemisorption on Ni(111).

Section 5.2 – Experimental details

5.2.1 Overview

The experimental apparatus has been described in Chapter II and elsewhere[3, 9]. Here, we only summarize key details for this project. Mixtures of CH_4 seeded in H_2 (1%, 3% and 5% from Airgas, Inc) expanded continuously and supersonically through a temperature-controlled nozzle and into a high vacuum chamber. The triply differentially pumped beam impinged on a Ni(111) crystal housed in an ultra-high vacuum (UHV) chamber. As explained in elsewhere[3], control experiments verified that our results were not influenced by the adsorption of background gases or impurities in the beam or main chamber. Surface temperatures (T_s = 475K or 550K) investigated here were well above the temperature at which physisorbed CH_4 molecules and chemisorbed H atoms desorb from the surface. Reactivity is measured in the limit of low surface coverage (<0.10 ML), so site-blocking by adsorbed C atoms is minimal and negligible.

Our approach to the state-resolved reactivity benefits from a precise control over reagent energy. Laser excitation prepares gas-phase methane in a single rotational and vibrational quantum state with precisely defined internal energy. The narrow E_{trans} distribution ($\Delta E_{trans}/E_{trans}$ < 5%) in molecular beam, which was verified by time-of-flight measurements (see Section 5.2.2), provided a tight control over translational energy. Methane molecules in the beam had a vibrational state distribution related to a Boltzmann distribution at the nozzle source temperature

and the vast majority were in the vibrational ground state.[10] Direct infrared absorption measurements of molecules in the beam showed that rotational cooling was nearly complete for nozzle temperatures below 570 K. At higher nozzle temperatures, we used IR absorption to measure the extent of rotational cooling and accounted for incomplete cooling in our calculation of f_{exc}, the fraction of molecules excited by the laser. Frequency-stabilized infrared (IR) light from a continuous wave, narrow band laser intersected the molecular beam and excited (from 6 to 10%) CH_4 to a single internal quantum state, J = 2 of the $\nu_2 + \nu_4$ vibration, via the R(1) transition at 2868.72 cm^{-1}. A pyroelectric detector translated into the molecular beam quantified IR absorption for both room temperature and heated nozzle expansions. Methane has a long IR radiative lifetime, so molecules prepared in a rovibrational eigenstate of the gas-phase molecule impinged on the 475 K Ni(111) surface in their initially prepared state. In the other words, intramolecular vibrational redistribution (IVR) did not occur until methane began to experience the gas-surface interaction potential, which typically occurred a few hundred femtoseconds prior to reaction or non-reactive scattering. The UHV chamber contained standard surface-science instruments including a quadruple mass spectrometer for time-of-flight beam characterization and temperature programmed desorption (TPD) detection, Auger electron spectroscopy and argon ion sputtering for surface characterization and cleaning. Radiative heating provided better than ± 1 K control over the surface temperature.

We measured reaction probability with ($S_0^{Laseron}$) and without ($S_0^{Laseroff}$) laser excitation by exposing a beam of known flux to the surface for a fixed time. Then we quantified the surface bound C reaction products using oxygen titration, introduced in Chapter II and elsewhere[11]. Mass spectrometry monitored the partial pressure of desorbing CO while the 550 K surface was held in a 1.4×10^{-8} Torr background pressure of O_2. The monolayer (ML) coverage (between 6 and 9% ML) of carbon on the surface was calibrated with saturated ethylene (4% C_2H_4 in Ar) doses, which leads to a well defined and self-limiting saturation coverage (43% ML) of carbon on Ni(111) [5].

Our measurements of the sticking probability with and without laser excitation allow us to calculate a state-resolved reactivity for the particular laser-excited state $\nu_2 + \nu_4$. Equation 5.1 relates the state-resolved reactivity ($S_0^{\nu_2+\nu_4}$), to the reactivity with laser ($S_0^{Laseron}$), without laser ($S_0^{Laseroff}$), the fraction of molecules excited (f_{exc}), which we measure directly, and the vibrational ground state reactivity ($S_0^{V=0}$) [3, 12]

$$S_0^{\nu_2+\nu_4} = \frac{S_0^{Laseron} - S_0^{Laseroff}}{f_{exc}} + S_0^{V=0} \qquad \textbf{Eq. 5.1}$$

When E_{trans} is relatively low, $S_0^{V=0}$ contributes negligibly to $S_0^{\nu_2+\nu_4}$ and can be neglected.

5.2.2 Time-of-flight (TOF) Measurements

We use TOF measurements to characterize the distribution of velocities in our supersonic molecular beam and precisely measure E_{trans} for the S_0 curve. The setup has been described elsewhere.[13] The path length is 50.0 cm for molecules flying in a straight line from the chopper wheel, which spun at 300Hz, to QMS ionizer. A multichannel scaler with 2 μs dwell time records TOF spectra (1500 channels per single scan, and 20,000 added scans). We use the SBVH for our TOF experiments since it can limit the beam size to fit entirely into the QMS ionizer. To extract the average velocity and velocity spread in the molecular beam, we use a non-linear least-squares fitting to the TOF data, which has the correct form for a velocity distribution from a supersonic expansion and corrects for electronic delays associated with our timing electronics. A delay of 14.5 μs was verified by performing TOF experiments with and without an extension part in main chamber. The difference in arrival time with and without the extension, which elongates the neutral flight path, provides an independent measure of flight time that is independent of electronic delay. Figure 5.1 shows TOF spectra for all nozzle temperatures and molecule seeding used in this project, and Table 5.1 summarizes E_{trans} calculated from these TOF measurements.

Table 5.1 Calculation of TOF measurements

Beam	T_N	Speed (m/s)	E_{trans} (kJ/mol)
5% CH_4/H_2	290	2271.74	41.3
5% CH_4/H_2	350	2488.10	49.5
3% CH_4/H_2	400	2824.32	63.8
3% CH_4/H_2	500	3166.67	80.2
3% CH_4/H_2	570	3370.97	90.9
1% CH_4/H_2	550	3603.45	103.9

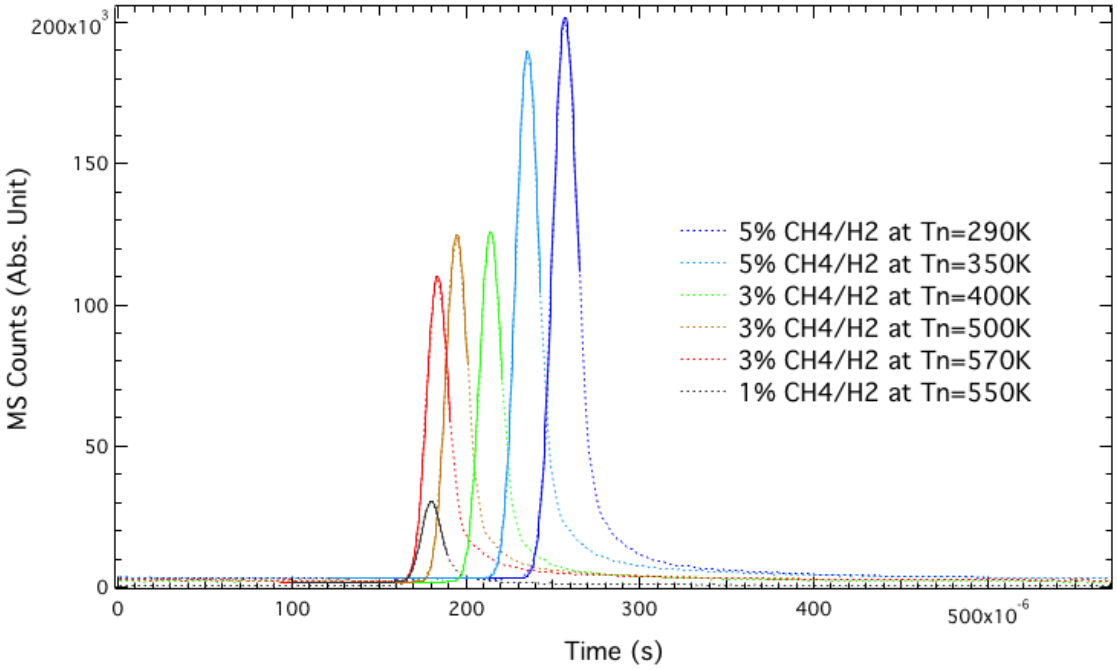

Figure 5.1 TOF spectra at different nozzle temperatures and beam concentrations of methane in the hydrogen carrier gas.

5.2.3 Spatial Deposition of Carbon

The O_2 titration method, which we used to probe methane's sticking probability in this project, determines carbon coverage by correlating the integrated area under the CO desorption feature to ML of C. Therefore, we need to avoid non-uniform deposition of laser-excited molecules on the Ni(111) surface. As a basic condition of using Equation 5.1 to calculate the state-resolved reactivity, laser excited molecules should have a same dosing profile on the surface as molecules in laser-off doses. Prior studies show that the combination of our narrow-linewidth laser source and inhomogeneous Doppler broadening of the infrared absorption transition in the molecular beam can result in spatially localized deposition on the surface.[14] Based on these concerns, we employ AES to map the carbon profile on the Ni(111) surface after laser-on and laser-off doses with same dosing condition. Fortunately, the much larger power provided by the new Aculight laser system makes it possible to extend the laser enhanced areal density across the entire molecular beam imaged on the crystal for the laser on experiments. We do this by adjusting the multipass mirror alignment to produce a fan pattern of laser-molecular beam crossings, so that each Doppler subset of molecules in the beam is resonant with the laser. The AES mapped carbon spatial deposition for both laser-on and laser-off experiments can be found in Figure 5.2.

For a uniformly excited CH_4 beam, the carbon spatial distribution is expected to have a top hat horizontal distribution. As can be observed in Figure 5.2 there appears to be a slightly different shape to that expected. This is due to the convolution of the finite-sized electron beam spot (ca. 1 mm) and the image of carbon deposited near the edges of the MBVH footprint as discussed elsewhere.[15] Given this effect, the data in Fig. 5.2 show that carbon deposition is uniform across the dosed area for laser on doses, as it is for laser off doses.

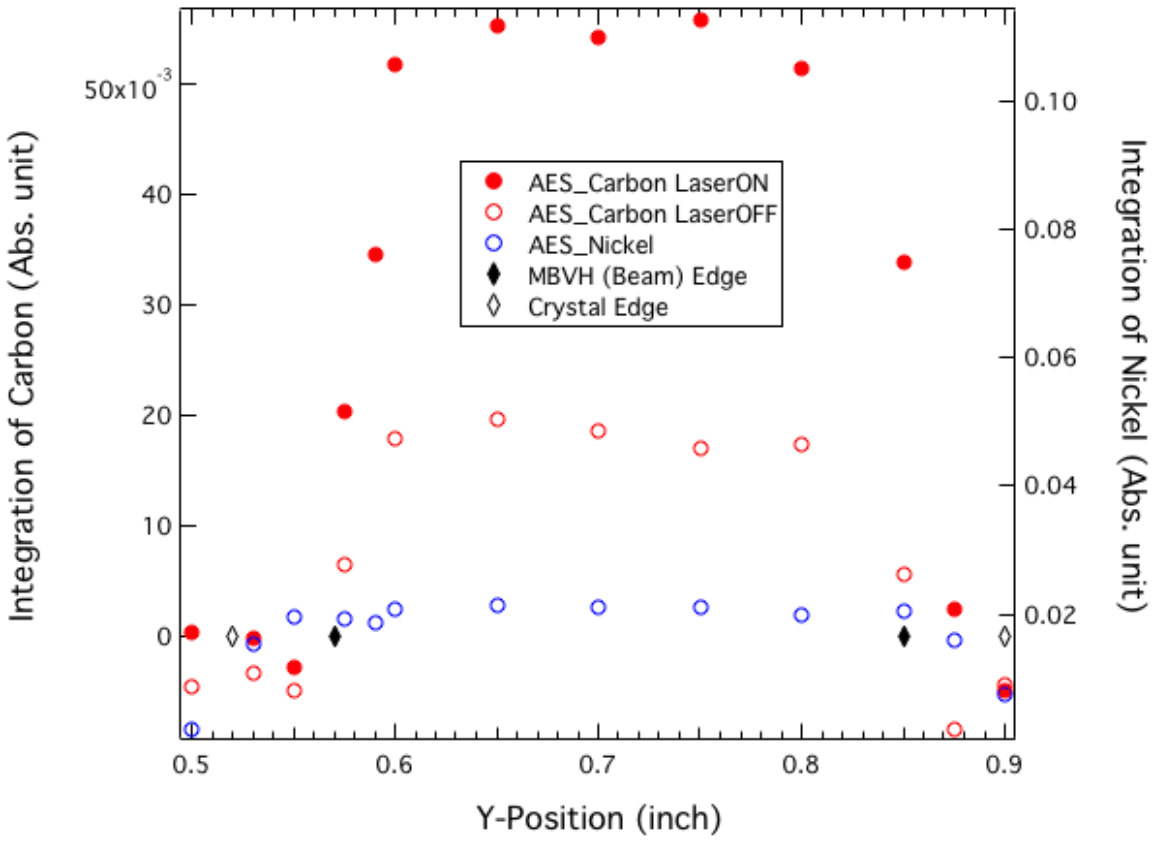

Figure 5.2 AES mapping of carbon on crystal with and without laser excitation.

5.2.4 Excitation of CH_4 into $\nu_2+\nu_4$

Once carbon deposition is quantified, f_{exc} is the remaining key quantity required to calculate state-resolved reactivity. Equation 5.2 relates f_{exc} to two quantities that we measure in our experiments, [9, 13, 16]

$$f_{exc} = f_{pop} \times f_2 \qquad \textbf{Eq 5.2}$$

where f_{pop} represents the fraction of CH_4 molecules in the rovibrational ground state for the infrared pumping transition, and f_2 is the fraction of those molecules excited to the excited state. The f_{pop} term is the product of the fraction of molecules in the desired initial rotational state (f_{rot}) and vibrational state (f_{vib}).

$$f_{pop} = f_{rot} \times f_{vib} \qquad \textbf{Eq. 5.3}$$

For f_{vib}, we need to calculate the population of molecules in vibrational ground state (v=0). As we explained in Section 3.3, the vibrational states in methane fall into groups, or polyads. The polyad number equals to the sum of the number of quanta of bending states (v_b) and twice the number of stretching states (v_s) as in Equation 5.4,

$$P = (2N_s + N_b) \qquad \textbf{Eq. 5.4}$$

Large gaps between polyads inhibit inter-polyad collisional cooling during supersonic expansion, but intra-polyad cooling is possible.[10] Thus, the lowest energy states in a polyad, which are usually combinations or overtones of bending vibrations, tend to be more highly populated than the higher energy states in a polyad. The total vibrational energy (E_{vib}) and the ground vibrational state population are nearly same as would be calculated from a Boltzmann distribution at

T_N since vibrational states in a polyad have similar energy.[13, 16] Due to collisional cooling among states of the same polyad, it may not be very accurate to use statistical calculations to predict the populations of individual states, but Boltzmann calculations predict integrated populations of each polyad well, as has been verified by direct IR absorption studies of a methane supersonic expansion.[10]

We use statistical mechanics to calculate the thermal distribution of vibrational states in our expansion.[16] We calculate the vibrational energy of each state as a sum of the energy of each fundamental mode multiplied by the quantum number (N_{vi}) for that mode as Equation 5.5 assuming no coupling of modes and the energies are in harmonic portion of the intramolecular potential.

$$E_i = (N_{\nu_1} \times E_{\nu_1}) + (N_{\nu_2} \times E_{\nu_2}) + (N_{\nu_3} \times E_{\nu_3}) + (N_{\nu_4} \times E_{\nu_4}) \qquad \textbf{Eq. 5.5}$$

The total E_{vib} is the sum of the population-weighted energies of each individual states up to 16,000 cm^{-1}, where has no significant contributions to E_{vib}. We have confirmed that higher energy states have negligible contribution and do not contribute significantly to the overall vibrational energy of the beam.

$$E_{vib} = \sum_{i=0}^{16{,}000cm^{-1}} \frac{n_i}{Q_{vib}} E_i \qquad \textbf{Eq. 5.6}$$

where the Boltzmann factor $n_i = g_i \times \exp\left(-\frac{E_i}{kT_N}\right)$, the degeneracy of the ith vibration is g_i, and Q_{vib} is the vibrational partition function, which is the product of the partition functions for each fundamental mode.

$$Q_{vib} = Q_{\nu_1} \times Q_{\nu_2} \times Q_{\nu_3} \times Q_{\nu_4} \qquad \textbf{Eq. 5.7}$$

where Q_{vi} is calculated as

$$Q_{v_i} = \frac{1}{\left(1 - \exp\left(-\frac{E_i}{kT_N}\right)\right)^{g_{i,v=1}}} \qquad \textbf{Eq. 5.8}$$

The ratio of n_i and Q_{vib} gives the fractional population of a given state. The total wavefunction is the product of the wavefunctions of the four fundamental modes, so the degeneracy for each state, g_i, is given by Equation 5.9.

$$g_i = g_{v_1} \times g_{v_2} \times g_{v_3} \times g_{v_4} \qquad \textbf{Eq. 5.9}$$

We summarize wavenumbers for each fundamental mode and their degeneracy in Table 5.2. Now we can calculate f_{vib} for the vibrational ground state based on the analysis above.

Table 5.2 Fundamental vibrational-modes for CH_4

Mode	Band Center (cm^{-1})	Symmetry	Degeneracy, g_v
Symmetric Stretch (ν_1)	2914	A_1	1
Doubly degenerate bend (ν_2)	1524	E	$\left(N_{\nu_2}+1\right)$
Anti-Symmetric Stretch (ν_3)	3020	F_2	$\frac{1}{2}\left(N_{\nu_3}+1\right)\left(N_{\nu_3}+2\right)$
Triply degenerate bend (ν_4)	1306	F_2	$\frac{1}{2}\left(N_{\nu_4}+1\right)\left(N_{\nu_4}+2\right)$

As mentioned in Section 4.3, methane has three distinct nuclear spin symmetries, A, E, and F. Selection rules prohibit interchanges between different symmetries.[17] Thus, only following interchanges are possible,

$$A \Leftrightarrow A;\ \ E \Leftrightarrow E;\ \ F \Leftrightarrow F \qquad \textbf{Eq. 5.10}$$

These three distinct rotational levels make the calculation of f_{rot} more complicated than f_{vib}, so we cannot use the statistical mechanics used in f_{vib} calculation. We have to calculate the rotational partition function (Q_{rot}) and the Boltzmann factors (n_i) to predict the populations of individual states. Q_{rot} is defined in Equation 5.11.

$$Q_{rot} = \sum_{J=0}^{50} g_J \exp\left(-\frac{hcE_J}{kT_{rot}}\right) \qquad \textbf{Eq. 5.11}$$

T_{rot} represents rotational temperature, which characterizes the rotational state distribution in the supersonic expansion. Juurlink[13] and Smith[16] measured and calculated T_{rot} for a series of H_2 seeded and pure CH_4 beams at different T_N. Equation 5.12 shows an empirical relationship found by Smith[16] between fraction of CH_4 in the molecular beam (F_{CH4}) and T_{rot} for beams seeded with H_2.

$$T_{rot} = 16.34 \times F_{CH_4} + 10.49 \qquad \textbf{Eq. 5.12}$$

Back to Equation 5.11, E_J is the energy of rotational level J, and g_J is degeneracy of that level. Including centrifugal distortion of a rotating molecule, E_J is calculated via Equation 5.13.

$$E_J = B_0 J(J+1) - D_0 J^2 (J+1) \qquad \textbf{Eq. 5.13}$$

where B_0 is the rotational constant, D_0 is the centrifugal distortion constant for the vibrational ground state. As the three distinct nuclear spin symmetries, g_J needs to involve the effect of nuclear spin statistics as shown in Equation 5.14.

$$g_J = \varepsilon_J(2J+1) \qquad \textbf{Eq. 5.14}$$

where $\varepsilon_J = \sum_{\Gamma} \varepsilon_{\Gamma} n_{\Gamma}$, and ε_{Γ} is the nuclear spin statistical weight, n_{Γ} is the number of levels of a certain symmetry. CH_4 has a nuclei spin (I) of ½, so the statistical weights for A:E:F is 5:2:3. As all symmetry species are non-interchangeable, we can use separate partition function for each symmetry species and get the total Q_{rot} by summing them together.

$$Q_{\Gamma} = \sum_{J=0}^{50} \varepsilon_{\Gamma} n_{\Gamma} J(2J+1) \exp\left(-\frac{hcE_J}{kT_{rot}}\right) \qquad \textbf{Eq. 5.15}$$

$$Q_{rot} = \sum_{\Gamma} Q_{\Gamma} = Q_A + Q_E + Q_F \qquad \textbf{Eq. 5.16}$$

We can now calculate f_{rot} in the desired initial state for each J and symmetry species as a function of T_{rot}. Combining f_{vib} and f_{rot} gives us f_{pop} of the initial state.

Finally, we use an experimental method to find how many molecules we can actually pump out from the initial state. The f_2 term in Equation 5.2 represents the fraction of molecules that are actually pumped to the selected excitation state. It is an expression of how well the photons intersecting the molecular beam saturate the selected transition. It has an exponential dependence on the radiation density, ρ, and can be expressed as Equation 5.17.

$$f_2 = \frac{g_2}{g_1 + g_2}\left\{1 - \exp\left[-\rho \frac{A_{21}}{8\pi h\nu^2}\left(\frac{g_1 + g_2}{g_1}\right)t\right]\right\} \qquad \textbf{Eq. 5.17}$$

where g_1 and g_2 represent degeneracies of the ground and excited state of the desired transition, respectively; A_{21} is the Einstein coefficient; v is the frequency of the transition; t is the transit time, a ratio of the diameter of the laser beam and the velocity of molecules. ρ, defined by Equation 5.18, is dependent on laser power, the diameter of the laser beam, and the line width of the laser.

$$\rho = \frac{4P_l}{\pi c d^2 \Delta v} \qquad \textbf{Eq. 5.18}$$

Based on its definition, we can also express f_2 as Equation 5.19 if we use $f_{2,\infty}$ to present f_2 when t becomes large and f_{sat} to express the saturation fraction, the extent to which we saturate the desired transition.

$$f_2 = f_{2,\infty} \times f_{sat} \qquad \textbf{Eq. 5.19}$$

We measure the absorption of photons in the molecular beam (PED value) as a function of laser power (and hence ρ) to determine the f_{sat}. We attenuate laser power with a rotational waveplate and measure the PED values at each laser power. We then model the exponential function and asymptote using Equation 5.20.

$$y = y_{MAX}\left(1 - \exp(-A_1(P - A_2))\right) \qquad \textbf{Eq. 5.20}$$

where y represents PED value and P represents for laser power. A_1 and A_2 in Equation 5.20 are adjustable fitting parameters, and y_{MAX} is the asymptote of the laser saturation curves. Then we can calculate f_{sat} via Equation 5.21.

$$f_{sat} = \frac{y}{y_{MAX}} \qquad \textbf{Eq. 5.21}$$

The last term to achieve f_{exc} is $f_{2,\infty}$. As mentioned in Section 4.3, our laser is linearly polarized, so only transitions with $\Delta M_J = 0$ are allowed.[18] This restriction sets the same degeneracy for the upper and lower state ($g_1 = g_2$). Thus $f_{2,\infty}$ is expressed in Equation 5.22.

$$f_{2,\infty} = \frac{g_2}{g_1 + g_2} = \frac{g_1}{g_1 + g_1} = 1/2 \qquad \textbf{Eq. 5.22}$$

With approaches discussed above, we can now calculate f_2 with a single adjustable parameter (η) as shown in Equation 5.23.

$$f_2 = f_{2,\infty}\left[1 - \exp(-\eta t)\right] \qquad \textbf{Eq. 5.23}$$

In this stage, we have all terms needed to calculate f_{exc} for desired transition at certain beam conditions.

Besides the long traditional approaching to f_{exc} introduced earlier, we can now use our new laser system, which has much more power than the old color-center system, to scan all possible transitions of certain symmetry species. We use this method to determine the f_{exc} used in our measurements of $\nu_2 + \nu_4$ state-resolved reactivity. With HITRAN database,[19] we are able to find all possible $\nu_2 + \nu_4$ transitions with the same symmetry (F) as the R(1) transition of 2868.72 cm^{-1} used in our reactivity measurements. Since all beam conditions[1] used here have a nozzle temperature below 570 K, in which the rotational cooling in the beam is nearly complete, populations of rotational levels with $J \geq 5$ can be neglected. We list all $\nu_2 + \nu_4$ transition in F symmetry and R transition with $J < 5$ in Table 5.3. We scanned all

[1] Beam composition and nozzle temperature used

these transitions and recorded absorbance with PED signal for all beam conditions used in our measurements. We then measure the height of Gauss fittings of absorbance. The ratio between the value of height at 2868.72 cm^{-1} and the sum of all heights measured at the beam condition gives the population information. When times the maximum fraction of F symmetry (9/16) species in a supersonic CH_4 beam, it can provide the population fraction of ground state (f_{pop}). Therefore, we can calculate f_{exc} via Equation 5.24.

$$f_{exc} = \frac{1}{2} \times f_{pop} \times f_{sat} \qquad \textbf{Eq. 5.24}$$

where f_{sat} represents the laser saturation fraction measured in Figure 5.3. Data of f_{exc} are summarized in Table 5.4.

Table 5.3 $\nu_2 + \nu_4$ transitions with F rotational symmetry and R transition for J < 5 states from *HITRAN* database[19]

Frequency (cm^{-1})	Transition Type	Symmetry	Einstein A-coefficient (s^{-1})
2868.72	**R(1)**	$F_1 \rightarrow F_2$	**3.54E-01**
2867.11	R(2)	$F_2 \rightarrow F_1$	3.87E-01
2875.65	R(3)	$F_1 \rightarrow F_2$	3.00E-01
2877.17	R(3)	$F_2 \rightarrow F_1$	3.39E-01
2886.12	R(4)	$F_1 \rightarrow F_2$	2.73E-01
2888.56	R(4)	$F_2 \rightarrow F_1$	3.41E-01

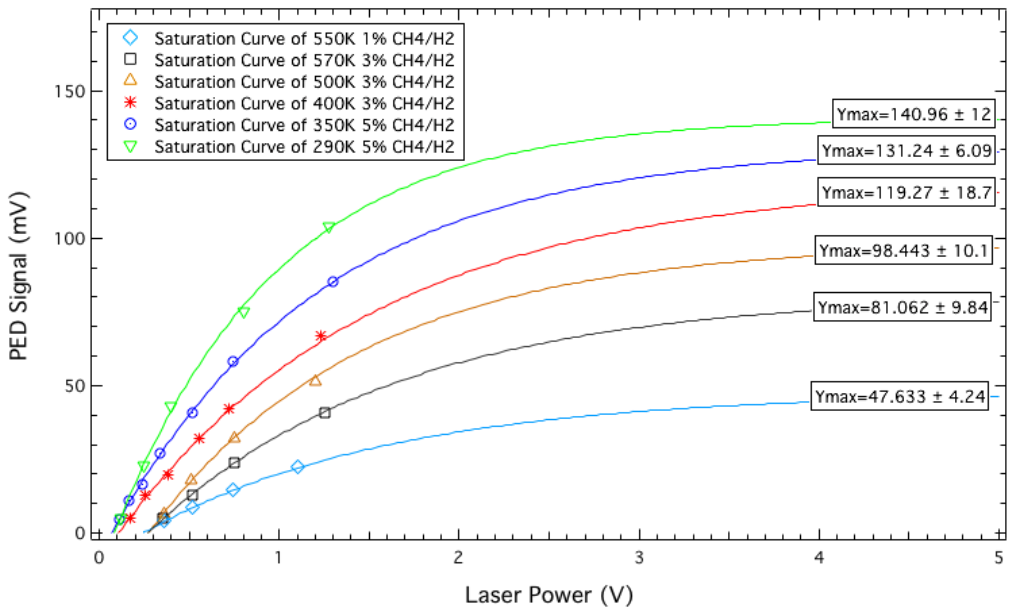

Figure 5.3 Laser saturation curves of molecular beams with different nozzle temperatures and beam seeding measured for R(1) excitation of $\nu_2 + \nu_4$ at 2868.72 cm^{-1}

Table 5.4 f_{exc} calculated from all possible transitions under J < 5

Beam	**T_N (K)**	**E_{trans} (kJ/mol)**	**f_{sat}**	**f_{pop}**	**f_{exc}**
5% CH_4/H_2	290	41.3	0.738	0.308	0.114
5% CH_4/H_2	350	49.5	0.648	0.287	0.093
3% CH_4/H_2	400	63.8	0.562	0.287	0.081
3% CH_4/H_2	500	80.2	0.523	0.252	0.066
3% CH_4/H_2	570	90.9	0.487	0.219	0.053
1% CH_4/H_2	550	103.9	0.473	0.249	0.059

Section 5.3 – Results and Discussion

We have summarized our results of $\nu_2 + \nu_4$ excited CH_4 dissociation on Ni(111) in Table 5.5. As mentioned in Section 5.1, calculations of the transition state for methane dissociation on nickel and other transition metals show significant distortions from methane's gas phase geometry. These distortions result in a "late" barrier for reaction and introduce a bias in which certain vibrational excitations in the gas-phase reagent may enjoy enhanced transition state access.[20-23] Both theoretical calculations based on density functional theory (DFT)[24, 25] and experimental data[26-28] suggest and show mode-selective reactivity in which different vibrational modes promote S_0 differently.

Measured dissociative chemisorption efficacies for methane's symmetric (ν_1)[27] and antisymmetric (ν_3)[12] C-H stretching vibrations on Ni(100) show that the symmetric ν_1 state has a significantly higher efficacy. This observation is consistent both with a vibrationally adiabatic model of reactivity[29] that has been invoked to explain mode-selectivity in bimolecular gas-phase methane reactions[30, 31] and with quantum wavepacket scattering calculations.[27, 29, 32, 33] In general, these calculations point to a relative ranking of vibrational efficacy for dissociative chemisorption of $\nu_1 > \nu_3 > \nu_2 \approx \nu_4$. A more recent reaction path Hamiltonian calculation from Jackson and coworkers[24] provides further insight into the origin of mode-selective behavior. If vibrationally excited molecules can undergo a transition to a lower-lying (or the

vibrational ground state) during a gas-surface encounter, energy freed by vibrational relaxation can convert into motion along the reaction path, which results in a large reactivity enhancement. The gas-phase vibrational symmetries of the doubly degenerate ν_2 (E) and the triply degenerate ν_4 (F_2) bending vibrations differ in their ability to couple to lower-energy vibrations, and therefore have different efficacies for promoting dissociative chemisorption. In fact, ν_2 practically behaves as a spectator to dissociative chemisorption on Ni(100).

To date, measured reaction probabilities for the ν_1 and ν_3 vibrational fundamentals (v=1 levels) and the second overtone of ν_4, $3\nu_4$, are consistent with these trends, but the data presented here are the first measurements for a mode containing significant ν_2 vibrational character and incident on a Ni surface. If we were to assume that ν_2 has the same efficacy for promoting reaction as does ν_4, we would expect ΔE_{trans} for $\nu_2 + \nu_4$ to be 74% of the 34 kJ/mol observed for the $3\nu_4$ state, or 25 kJ/mol, based on relative vibrational energies. The solid line in Figure 5.4 shows the S_0 curve we would expect if $\nu_2 + \nu_4$ and $3\nu_4$ shared the same efficacy. The $\nu_2 + \nu_4$ data clearly are not consistent with the efficacies for the two bending states being equal. Instead, Figure 5.5 shows ΔE_{trans} for $\nu_2 + \nu_4$ is only 15 kJ/mol, which is 60%, or just over half of the ΔE_{trans} predicted on the basis of the $3\nu_4$ overtone. While it is not clear that the ΔE_{trans} shifts for vibrations in an overtone or combination state are always additive, it is likely that ΔE_{trans} for the ν_4 fundamental is at least 1/3 that of the $3\nu_4$ overtone, or about 11 kJ/mol. That is because each additional quantum in a given

vibrational coordinate will likely provide incrementally less additional transition state access.[12, 34, 35] Therefore, if we assume the ΔE_{trans} shifts for the ν_2 and ν_4 coordinates to be additive, we would conclude that 18kJ/mol of E_{vib} in ν_2 contributes 4 kJ/mol or less to the ΔE_{trans} = 15 kJ/mol observed for $\nu_2 + \nu_4$. That leads to an inferred efficacy for ν_2 of $\eta_{vib}^{\nu_2} \leq 0.22$, the lowest observed for any vibrational mode in methane's dissociative chemisorption and more than a factor of six less that that reported for the ν_3 antisymmetric C-H stretch. The particularly low efficacy for ν_2 is consistent with the predictions of Jackson's reaction path calculations.

Our ability to quantify S_0 for $\nu_2 + \nu_4$ allows us to consider another aspect of energy flow during methane's dissociative chemisorption. Methane's vibrational states group in polyads of similar total energy. This structure arises from the near 2:1 resonance between the bend and stretch vibrational frequencies. In general, the energy gap between polyads is much greater than that between states in a given polyad. In studies of collisional energy transfer, intrapolyad energy transfer is much more efficient than interpolyad relaxation due to propensities that favor relatively small changes in E_{vib}. The reactivity data presented here are the first for a bending state that belongs to the pentad polyad in CH_4. The pentad also contains the previously studied ν_1 and ν_3 C-H stretching fundamentals, along with the $2\nu_2$ and $2\nu_4$ bending overtones. The fact that the efficacy for $\nu_2 + \nu_4$ is much less than that for the ν_3 C-H stretch state shows that the gas-surface collision is not sufficient to

significantly scramble excitation between stretching and bending states in the same polyad.

Table 5.5 State-resolved reactivity of CH_4 ($\nu_2 + \nu_4$) on Ni(111)

Beam	**T_N (K)**	**E_{trans} (kJ/mol)**	**f_{exc}**	**$S_0^{\nu2+\nu4}$**	**2σ of $S_0^{\nu2+\nu4}$**
5% CH_4/H_2	290	41.3	0.114	1.78E-05	1.00E-05
5% CH_4/H_2	350	49.5	0.093	3.03E-05	1.71E-05
3% CH_4/H_2	400	63.8	0.081	1.49E-04	6.48E-05
3% CH_4/H_2	500	80.2	0.066	1.97E-03	7.96E-04
3% CH_4/H_2	570	90.9	0.053	3.76E-03	1.40E-03
1% CH_4/H_2	550	103.9	0.059	1.10E-02	4.50E-03

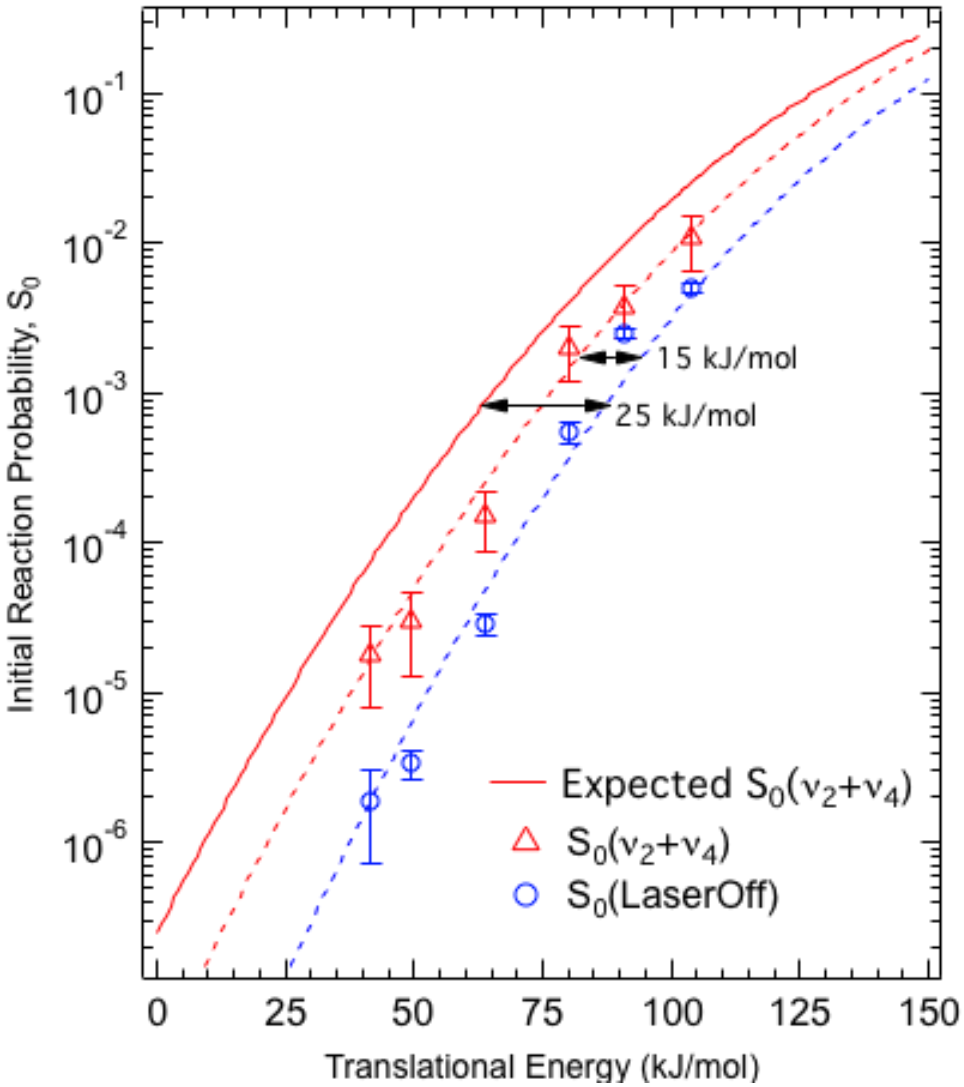

Figure 5.4 Sticking curves for ($\nu_2 + \nu_4$) excited methane (triangles) and non-laser exited methane no Ni(111) (circles). Expected S_0 curve is estimated based on the assumption of the same efficacy between ($\nu_2 + \nu_4$) and $3\nu_4$

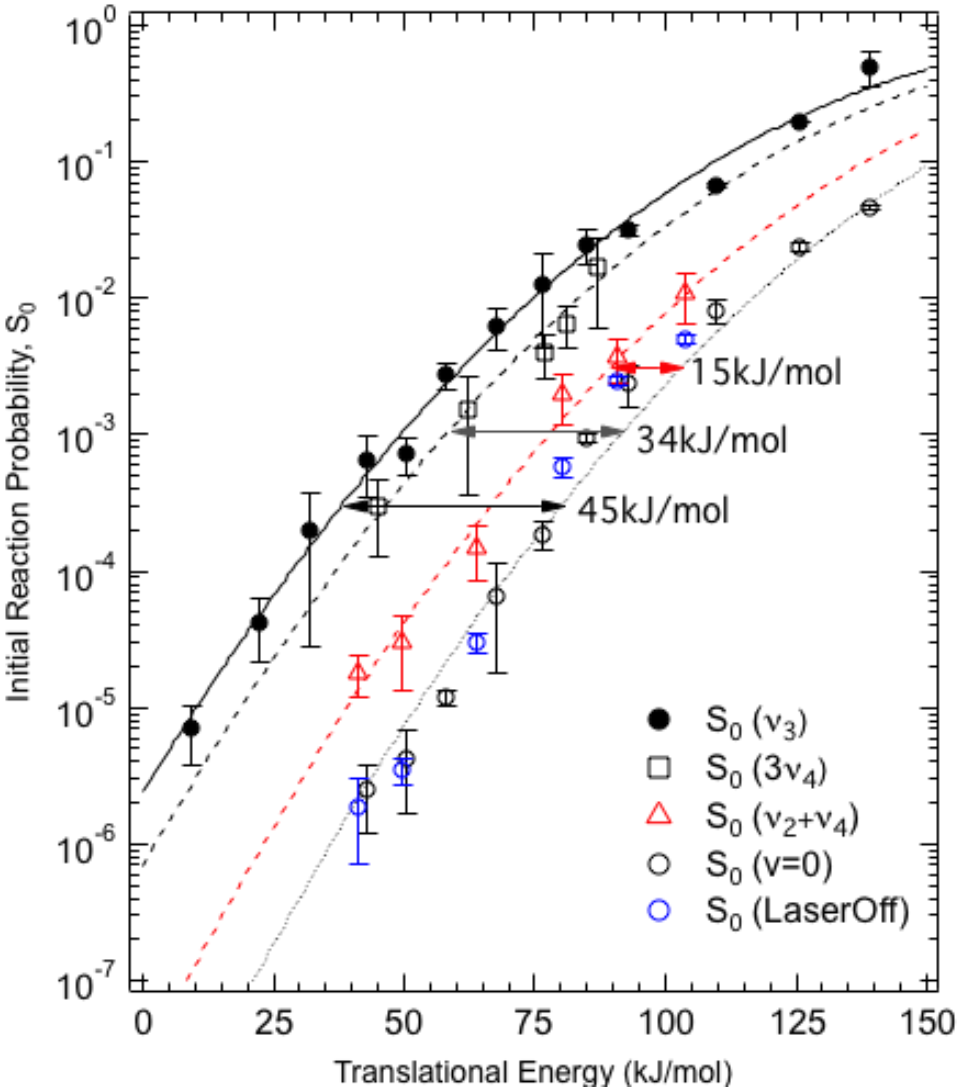

Figure 5.5 Sticking curves for ν_3, $3\nu_4$, $\nu_2 + \nu_4$ excited and ground state (v=0) CH_4 on Ni(111).[2]

[2] ν_3 and v=0 data from ref. 6, $3\nu_4$ data from ref. 25.

Section 5.4 – Conclusion and Future Work

Data reported here deepen our understanding of vibrational activation in CH_4 dissociation on a nickel surface. We have measured the state-resolved reaction probability for methane molecules excited to the $\nu_2 + \nu_4$ combination vibration and incident on a Ni(111) surface with translational energies ranging from 45 to 100 kJ/mol. Relative to the vibrational ground state, $\nu_2 + \nu_4$ decreases the E_{trans} threshold for reaction by 15 kJ/mol, corresponding to a vibrational efficacy of $\eta_{vib}^{\nu_2+\nu_4}$ of 0.44, which is significantly less that that of the ν_3 antisymmetric C-H stretch or the $3\nu_4$ overtone of the triply degenerate bending state. We estimate the efficacy of the ν_2 quantum in the vibration to be much less than that of all other vibrational fundamentals in methane based on our prior measurements of the $3\nu_4$ state on this surface. The wide range of vibrational efficacies observed for methane dissociation on Ni(111) suggest that purely statistical theories are unreliable predictors of reactivity at the quantum-state resolved level. Instead, it is likely that the dynamics of vibrational energy flow during the brief gas-surface encounter are the key to understanding the origin and generality of vibrational mode- and bond selective reactivity on metal surfaces. Finally, the large difference in efficacy for the ν_3 and $\nu_2 + \nu_4$ states, both of which belong to the same polyad, suggest that energy transfer between bending and stretching vibrations in the same polyad are not fast enough to influence reactivity.

In order to better understand the role of ν_4 and ν_2 bending mode in the overall reactivity, we expect that an S_0 curve of state-resolved reactivity of CH_4 ($2\nu_4$) on Ni(111) would be very useful. It in the same polyad as $\nu_2 + \nu_4$ state and it can provide direct comparison between ν_4 and ν_2 bending mode. Moreover, along with the state-resolved reactivity of CH_4 ($3\nu_4$) on Ni(111), it may further uncover the mechanism of combination of vibrational quanta and modes. It will be a meaningful project to further explore the dynamic details of CH_4 dissociation on Ni surfaces.

Reference

1. Beck, R. D.; Utz, A. L., Quantum-State Resolved Gas/Surface Reaction Dynamics Experiments. In *Springer Series on Surface Science*, Springer-Verlag Berlin Heidelberg: 2013.

2. Utz, A. L., Mode selective chemistry at surfaces. *Current Opinion in Solid State & Materials Science* **2009,** *13* (1-2), 4-12.

3. Juurlink, L. B. F.; Killelea, D. R.; Utz, A. L., State-resolved probes of methane dissociation dynamics. *Progress in Surface Science* **2009,** *84* (3-4), 69-134.

4. Lee, M. B.; Yang, Q. Y.; Ceyer, S. T., DYNAMICS OF THE ACTIVATED DISSOCIATIVE CHEMISORPTION OF CH4 AND IMPLICATION FOR THE PRESSURE GAP IN CATALYSIS - A MOLECULAR-BEAM HIGH-RESOLUTION ELECTRON-ENERGY LOSS STUDY. *Journal of Chemical Physics* **1987,** *87* (5), 2724-2741.

5. Holmblad, P. M.; Wambach, J.; Chorkendorff, I., MOLECULAR-BEAM STUDY OF DISSOCIATIVE STICKING OF METHANE ON NI(100). *Journal of Chemical Physics* **1995,** *102* (20), 8255-8263.

6. Smith, R. R.; Killelea, D. R.; DelSesto, D. F.; Utz, A. L., Preference for vibrational over translational energy in a gas-surface reaction. *Science* **2004,** *304* (5673), 992-995.

7. Juurlink, L. B. F.; Smith, R. R.; Killelea, D. R.; Utz, A. L., *Phys. Rev. Lett.* **2005,** *94*, 208303-208306.

8. Bisson, R.; Sacchi, M.; Dang, T. T.; Yoder, B.; Maroni, P.; Beck, R. D., State-resolved reactivity of CH4(2 nu(3)) on Pt(111) and Ni(111): Effects of barrier height and transition state location. *Journal of Physical Chemistry A* **2007,** *111* (49), 12679-12683.

9. Killelea, D. R.; Campbell, V. L.; Shuman, N. S.; Utz, A. L., Bond-selective control of a heterogeneously catalyzed reaction. *Science* **2008,** *319* (5864), 790-793.

10. Bronnikov, D. K.; Kalinin, D. V.; Rusanov, V. D.; Filimonov, Y. G.; Selivanov, Y. G.; Hilico, J. C., Spectroscopy and non-equilibrium distribution of vibrationally excited methane in a supersonic jet. *Journal of Quantitative Spectroscopy & Radiative Transfer* **1998,** *60* (6), 1053-1068.

11. Egeberg, R. C.; Ullmann, S.; Alstrup, I.; Mullins, C. B.; Chorkendoff, I., Dissociation of CH4 on Ni(111) and Ru(0001). *Surface Science* **2002,** *497* (1-3), 183-193.

12. Juurlink, L. B. F.; McCabe, P. R.; Smith, R. R.; DiCologero, C. L.; Utz, A. L., Eigenstate-resolved studies of gas-surface reactivity: CH4 (nu(3)) dissociation on Ni(100). *Physical Review Letters* **1999,** *83* (4), 868-871.

13. Juurlink, L. B. F. Eigenstate-Resolved Measurements of Methane Dissociation on Ni(100). Tufts University, Medford, 2000.

14. Juurlink, L. B. F.; Smith, R. R.; Utz, A. L., Controlling surface chemistry with light: Spatially resolved deposition of rovibrational-state-selected molecules. *Journal of Physical Chemistry B* **2000,** *104* (14), 3327-3336.

15. Campbell, V. L. State Resolved Measurements of Surface Temperature Dependence and Isotopically Selective Reactivity of Methane on Ni(111). Tufts University, Medford, 2011.

16. Smith, R. R. Rovibrational State-Resolved Studies of Methane Dissociation on Ni(111). Tufts University, Medford, 2003.

17. Herzberg, G., *Molecular spectra and molecular structure*. 2nd ed.; Krieger Publishing Co.: Malabar, 1991; Vol. 2, p 636.

18. Zare, R. N., OPTICAL PREPARATION OF ALIGNED REAGENTS. *Berichte Der Bunsen-Gesellschaft-Physical Chemistry Chemical Physics* **1982,** *86* (5), 422-425.

19. Rothman, L. S.; Gordon, I. E.; Barbe, A.; Benner, D. C.; Bernath, P. E.; Birk, M.; Boudon, V.; Brown, L. R.; Campargue, A.; Champion, J. P.; Chance, K.; Coudert, L. H.; Dana, V.; Devi, V. M.; Fally, S.; Flaud, J. M.; Gamache, R. R.; Goldman, A.; Jacquemart, D.; Kleiner, I.; Lacome, N.; Lafferty, W. J.; Mandin, J. Y.; Massie, S. T.; Mikhailenko, S. N.; Miller, C. E.; Moazzen-Ahmadi, N.; Naumenko, O. V.; Nikitin, A. V.; Orphal, J.; Perevalov, V. I.; Perrin, A.; Predoi-Cross, A.; Rinsland, C. P.; Rotger, M.; Simeckova, M.; Smith, M. A. H.; Sung, K.; Tashkun, S. A.; Tennyson, J.; Toth, R. A.; Vandaele, A. C.;

Vander Auwera, J., The HITRAN 2008 molecular spectroscopic database. *Journal of Quantitative Spectroscopy & Radiative Transfer* **2009,** *110* (9-10), 533-572.

20. Yang, H.; Whitten, J. L., DISSOCIATIVE CHEMISORPTION OF CH4 ON NI(111). *Journal of Chemical Physics* **1992,** *96* (7), 5529-5537.

21. Jansen, A. P. J.; Burghgraef, H., MCTDH study of CH4 dissociation on Ni(111). *Surface Science* **1995,** *344* (1-2), 149-158.

22. Luntz, A. C., CH4 DISSOCIATION ON NI(100) - COMPARISON OF A DIRECT DYNAMICAL MODEL TO MOLECULAR-BEAM EXPERIMENTS. *Journal of Chemical Physics* **1995,** *102* (20), 8264-8269.

23. Kratzer, P.; Hammer, B.; Norskov, J. K., A theoretical study of CH4 dissociation on pure and gold-alloyed Ni(111) surfaces. *Journal of Chemical Physics* **1996,** *105* (13), 5595-5604.

24. Nave, S.; Jackson, B., Methane dissociation on Ni(111): The effects of lattice motion and relaxation on reactivity. *J. Chem. Phys.* **2007,** *127* (22), 224702-224712.

25. Henkelman, G.; Arnaldsson, A.; Jonsson, H., Theoretical calculations of CH4 and H-2 associative desorption from Ni(111): Could subsurface hydrogen play an important role? *Journal of Chemical Physics* **2006,** *124* (4).

26. Beck, R. D.; Maroni, P.; Papageorgopoulos, D. C.; Dang, T. T.; Schmid, M. P.; Rizzo, T. R., *Science* **2003,** *302*, 98-100.

27. Maroni, P.; Papageorgopoulos, D. C.; Sacchi, M.; Dang, T. T.; Beck, R. D.; Rizzo, T. R., State-resolved gas-surface reactivity of methane in the symmetric C-H stretch vibration on Ni(100). *Physical Review Letters* **2005,** *94* (24).

28. Juurlink, L. B. F.; Smith, R. R.; Killelea, D. R.; Utz, A. L., Comparative study of C-H stretch and bend vibrations in methane activation on Ni(100) and Ni(111). *Physical Review Letters* **2005,** *94* (20).

29. Halonen, L.; Bernasek, S. L.; Nesbitt, D. J., Reactivity of vibrationally excited methane on nickel surfaces. *Journal of Chemical Physics* **2001,** *115* (12), 5611-5619.

30. Crim, F. F., Chemical reaction dynamics. *Proceedings of the National Academy of Sciences of the United States of America* **2008,** *105* (35), 12647-12648.

31. Bechtel, H. A.; Camden, J. P.; Brown, D. J. A.; Zare, R. N., Comparing the dynamical effects of symmetric and antisymmetric stretch excitation of methane in the Cl + CH4 reaction. *J. Chem. Phys.* **2004,** *120*, 5096–5103.

32. Milot, R.; Jansen, A. P. J., Bond breaking in vibrationally excited methane on transition-metal catalysts. *Physical Review B* **2000,** *61* (23), 15657-15660.

33. Milot, R.; Jansen, A. P. J., Ten-dimensional wave packet simulations of methane scattering. *Journal of Chemical Physics* **1998,** *109* (5), 1966-1975.

34. Michelsen, H. A.; Rettner, C. T.; Auerbach, D. J.; Zare, R. N., EFFECT OF ROTATION ON THE TRANSLATIONAL AND VIBRATIONAL-ENERGY DEPENDENCE

OF THE DISSOCIATIVE ADSORPTION OF D(2) ON CU(111). *J. Chem. Phys.* **1993,** *98* (10), 8294-8307.

35. Schmid, M. P.; Maroni, P.; Beck, R. D.; Rizzo, T. R., Surface reactivity of highly vibrationally excited molecules prepared by pulsed laser excitation: CH4 (2 nu(3)) on Ni(100). *J. Chem. Phys.* **2002,** *117* (19), 8603-8606.

Chapter VI Bond- and mode-selectivity of CH_2D_2 on Ni(111)

Section 6.1- Introduction

Controlling the products and yields of chemical reactions is always the goal of chemists. Experiments in this thesis use the selective deposition of energy into reactants and rely on restrictions on energy redistribution in the reactive system to achieve such control. In ideal cases, bond-selective chemistry can create products not normally accessible by cleavage of a selected bond in a molecule.[1] With the development of high-power, narrow-bandwidth lasers, albeit is now possible to selectively activate specific bonds in a molecule that would not react without laser excitation.[2] In this way, we can achieve fine control of reactions where the reaction site is selected by the chemist, not just by nature.

Studies of gas-phase reactions provide an easy way to understand the relationship between optical excitation and reactivity. In such situations, people don't need to worry about the energy exchange with solvent molecules. People can prepare long-lived excited reagents and measure the reactivity of the state-selected molecules. By doing so, the effects of vibrational excitation and collision energy on reactivity have

been demonstrated. Atom abstraction reactions are particularly amenable for such studies. For example, experiments of hydrogen abstraction from H_2O or CH_4 isotopomers by Cl or H have demonstrated that the vibrationally excited reactant can control the identity and energy distribution of products from the reaction. The first example of optical excited bond-selective chemistry is provided by Sinha et al. with the abstraction of H/D from DOH by an incident H atom.[3] Singly deuterated water, DOH, has vibrational states whose motion is localized in either the O–H or the OD bond.[4] In Sinha's experiment, gas-phase DOH molecules were excited to $|04\rangle$ state, in which four O–H stretch quanta are localized in the O-H bond. Then they used H atoms to collide with the excited DOH molecules. Laser induced fluorescence (LIF) detection of the hydroxyl fragment showed that only H was abstracted from the O–H excited DOH molecules producing H_2 and OD hydroxyls Vibrational excitation remained localized in O-H bond and there was no internal vibrational-energy redistribution (IVR) happened between the O–D and O-H bonds on the time scale of reaction. Further experiment by Metz et al. showed that vibrational excitation of the O–D bond results in OD bond cleavage, which produces O–H products.[5] These experiments demonstrated that products could be controlled by selective excitation of a bond in reactants and suggested a way for further exploration of the effects of vibrational excitation on reactivity.

Water is one of the simplest polyatomic molecules. Methane provides a more complicated vibrational structure as well as a less localized vibrational excitation,

which may result an incomplete projection of vibrational energy on the reaction coordinate. Thus, it's better to use vibrational modes, rather than localized C–H stretch oscillators to represent the excitation of methane. Methane is used as a prototype to study the effect of different vibrational modes on reactivity and bond-selective chemistry.[6-9] For example, Simpson *et al.* reported that reaction rate for H abstraction by Cl atoms colliding with CH_4 prepared in the antisymmetric C–H stretching (ν_3) state increased 30-fold relative to the rate for CH_4 molecules in the vibrational ground state. In contrast, Kim et al. reported CH_4 in the ($\nu_2 + \nu_4$) bending state is only ~15% as reactive as CH_4 in the ν_3 state when reacted with Cl atoms.[10] Both states have similar vibrational energy but different enhancements on reactivity, which indicates their vibrational energies project differently on reaction coordinate.

Bechtel et al. measured the vibrational state of products of Cl atoms with CH_2D_2 prepared in C-H stretching state. They reported that the product state distribution was decided by the initial vibrational state of CH_2D_2.[11] In their experiments, CH_2D_2 molecules were excited into two overtone C-H stretch states with similar vibrational energy but different nuclear motions, the $|20\rangle$ and the $|11\rangle$ state. The $|20\rangle$ state has two stretch quanta localized in one C-H bond, whereas each C-H bond contains one stretch quantum in the $|11\rangle$ state. Their results showed that the reaction of Cl with the $|20\rangle$ excited CH_2D_2 yields the H atom abstraction product CHD_2 in the vibrational ground state, whereas the $|11\rangle$ excited CH_2D_2 yields CHD_2 with one quantum of C-H

stretch excited. Thus, C-H excitation in the non-reactive bond behaved like a spectator to reaction. This experiment demonstrated that minimal IVR of CH_2D_2 happened during the time scale of the reaction, and suggested vibrational excitation contributes in a bond-specific way to promoting the methane reaction.

The above examples show how vibrational excitation affects the outcome for an isolated gas-phase reaction. Recent progress on state-selected methane dissociation on nickel surfaces shows that gas-surface reactions, which have many possible quenching and relaxation channels, can have similar results as these gas-phase studies. The first example of vibrational mode-specific behavior in a gas-surface reaction was reported by Beck et al. by studying CH_2D_2 dissociation on Ni(100).[12] In analogy to the CH_2D_2 + Cl gas-phase reaction, Beck et al. excited CH_2D_2 molecules to the $|20\rangle$ and $|11\rangle$ states, and measured their relative reaction probability for dissociation and chemisorption on the surface. Their results are also same - the $|20\rangle$ state, whose vibrational energy is more localized, was significantly more reactive than the $|11\rangle$ state though both states have identical total energy, therefore demonstrating mode-selective reactivity. Does the other result of the gas-phase studies, bond selective chemistry, hold true for a gas-surface reaction? Killelea et al. studied the bond-selective chemistry of CHD_3 dissociation on Ni(111). They excited CHD_3 to ν_1 C-H stretch state, which results an exclusively C-H cleavage in contrast to a mixture of C-H and C-D cleavage without laser excitation. This result indicates the vibrational energy remains localized in the excited bond on the reaction timescale.

Another example is reported by Chen et al., who probed the branching ratio of CHD_3, CH_2D_2, and CH_3D on Pt(111) with reflection absorption infrared spectroscopy (RAIRS). Their result also indicated the vibration energy is localized and bond-selectivity resulted by laser excitation.

The results summarized here as well as the efficacies of different vibrational modes summarized in Table 1.1 show that vibrational excitation can drastically affect the outcome of chemical reaction. Earlier reports showed a mode selective preference for CH_4 dissociation on Ni(100). Juurlink et al. observed an efficacy of 1.0 for CH_4 in anti-symmetric stretch (ν_3) excitation on Ni(100).[13] Maroni et al. found an efficacy of 1.4 for CH_4 in symmetric stretch (ν_1) excitation on the same surface.[14] The reason caused this distinct difference on efficacies is still uncertain. Besides having a different vibrational symmetry, symmetric stretch (ν_1) of CH_4 doesn't have a dipole moment change in its vibration, whereas dose anti-symmetric stretch (ν_3). In order to test whether symmetry alone is determining factor, we will explore two vibrational excitations of CH_2D_2, ν_1 (symmetric stretch) and ν_6 (anti-symmetric stretch), which both have changes of dipole moments in their vibrations. The comparison between their enhancements to the reactivity of CH_2D_2 dissociation on Ni(111) will provide clues to better understanding the vibrational symmetry effect in methane dissociation.

Section 6.2 - Approach to Anti-symmetric Stretch of CH_2D_2 (ν_6)

As a less abundant isotopologue of CH_4 in nature, infrared transitions for CH_2D_2 are not included in the current HITRAN Database. As a result, we rely on the literature and on published spectroscopic constants to identify the wavenumber and quantum numbers for the transitions we desire. Deroche et al. tabulated all IR transitions near 3000 cm^{-1} for CH_2D_2 following excitation of v=0 to the ν_1 symmetric C-H stretching vibration,[15] but only spectroscopic constants are provided for transitions to the ν_6 antisymmetric C-H stretch vibration. Thus we need to calculate the wavenumbers of transitions resulting in ν_6 excitation.

First, let us take a close look at a CH_2D_2 molecule. CH_2D_2 is the only asymmetric top molecule among the isotopologues of CH_4. It belongs to the symmetry point group C_{2v} with one C_2 axis and two mutually perpendicular symmetry planes σ_{xy} and σ_{xz} as shown in Figure 6.1. Two hydrogen nuclei lie on the σ_{xy} plane and two deuterium nuclei are on σ_{xz} plane. The X axis represents the C_2 axis. As an asymmetric top, CH_2D_2 has three unique moments of inertia, I_a, I_b, and I_c, with $I_a < I_b < I_c$. Consequently, I_a is parallel to the Z axis, I_b is collinear to X axis, and I_c is parallel to the Y axis.

In the symmetric rotor limit, the projection of the total angular momentum along the molecule-fixed symmetry axis ($K = K_a$ for prolate top) is a good quantum

number, but in the asymmetric rotor, it's no longer a good quantum number. So we use Equation 6.1 (for diagonal elements) and Equation 6.2 (for off-diagonal elements) to build a matrix to represent the rovibrational eigenstates in the basis of a prolate symmetric rotor.

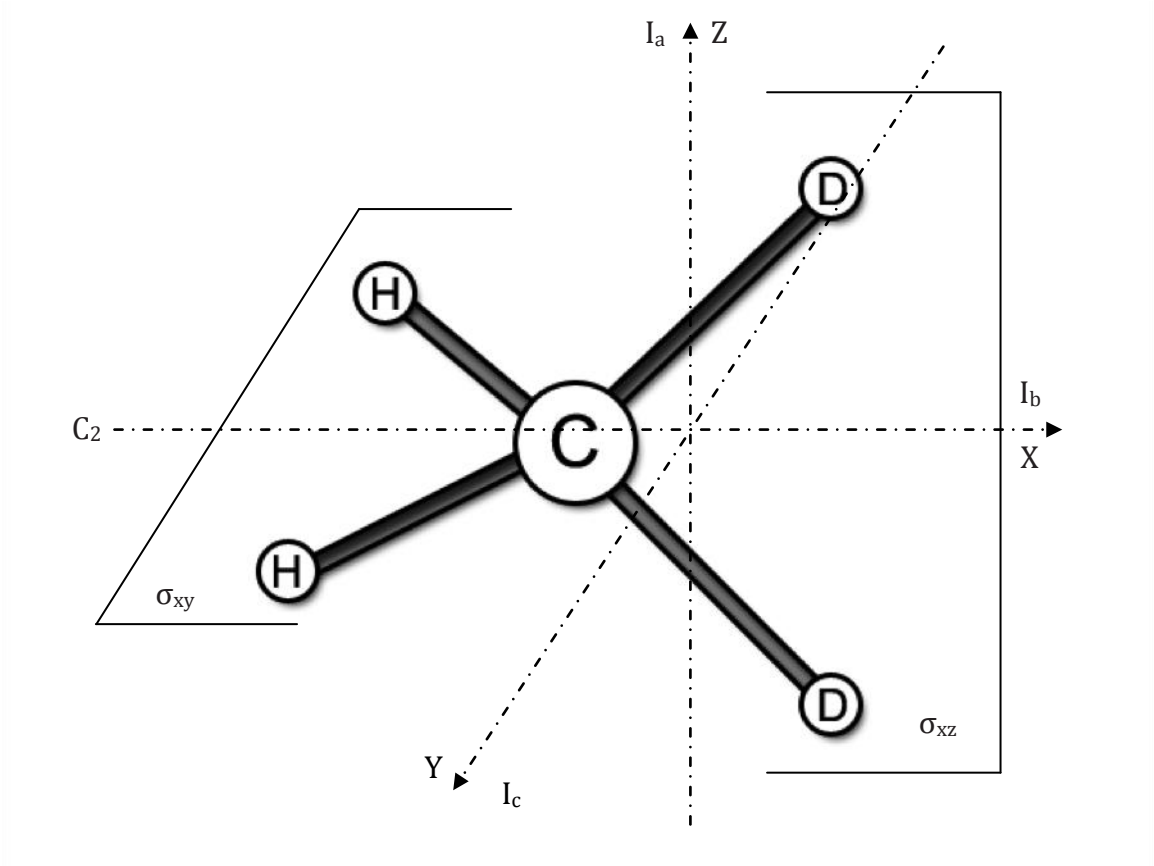

Figure 6.1 Geometry of the CH_2D_2 molecule. The origin of the coordinate system is the center of mass in the molecule.

$$\langle v,J,K|H|v,J,K\rangle = \frac{1}{2}(B_V + C_V)(J(J+1) - K^2) + A_V K^2 - D_V^J J^2 (J+1)^2 - D_V^{JK} J(J+1)K^2 - D_V^K K^4$$

Eq. 6.1

$$\langle v,J,K\pm 2|H|v,J,K\rangle = \frac{1}{4}(B_V - C_V)\left[(J^2 - (K\pm 1)^2)((J+1)^2 - (K\pm 1)^2)\right]^{1/2} - \delta_J J(J+1) - \delta_K K^2$$

Eq. 6.2

In above equations, V, J, K are the vibrational, rotational, and prolate top quantum numbers (K=Ka), A_v, B_v, C_v are the effective rotational constants about the molecule-fixed a, b, and c inertial axes of the molecule. The D_V^J, D_V^{JK}, D_V^K are symmetric rotor centrifugal distortion constants. δ_J and δ_K are the quartic distortion coefficients. All parameters used in the calculation are summarized in Table 6.1. Diagonalization of this matrix yields the rotational energy eigenvalues and eigenvectors of the asymmetric rotor levels expressed as function of the symmetric rotor basis.[1] We build a matrix for each J (J ≤ 15), and calculate a set of eigenvalues for each value of J. A correlation diagram for the asymmetric rotor state energy levels associated with J=3 is shown in Figure 6.2, and a sample matrix for J = 3 is shown in Table 6.2. As indicated in Figure 6.2, the asymmetric parameter for CH_2D_2 is calculated as -0.27 via Equation 6.3,

$$\kappa = \frac{2B - A - C}{A - C}$$

Eq. 6.3

where A, B, C are the rotational constants of the molecule.

[1] We do not include sextic distortion coefficients here since they are negligible for the low-J and K levels we access in our molecular beam studies.

Table 6.1 Rotational constants for CH_2D_2.[2]

Constants	ν_1 (cm^{-1})	ν_6 (cm^{-1})
A	4.265293	4.281663
B	3.488743	3.488911
C	3.047177	3.036024
D_j	0.000035	0.000049
D_{jk}	0.000014	-0.000023
D_k	0.000048	0.000071
H_k	0.000000	0.000000
δ_J	0.000010	0.000010
δ_K	-0.000012	-0.000022

[2] Data from ref. 13

Table 6.2 Matrix constructed using Equation 6.1 and 6.2 for J = 3

K (J=3)	3	2	1	0	-1	-2	-3
3	48.3121	0.0000	0.8769	0.0000	0.0000	0.0000	0.0000
2	0.0000	43.2193	0.0000	1.2402	0.0000	0.0000	0.0000
1	0.8771	0.0000	40.1620	0.0000	1.3586	0.0000	0.0000
0	0.0000	1.2402	0.0000	39.1426	0.0000	1.2402	0.0000
-1	0.0000	0.0000	1.3586	0.0000	40.1620	0.0000	0.8771
-2	0.0000	0.0000	0.0000	1.2402	0.0000	43.2193	0.0000
-3	0.0000	0.0000	0.0000	0.0000	0.8769	0.0000	48.3121

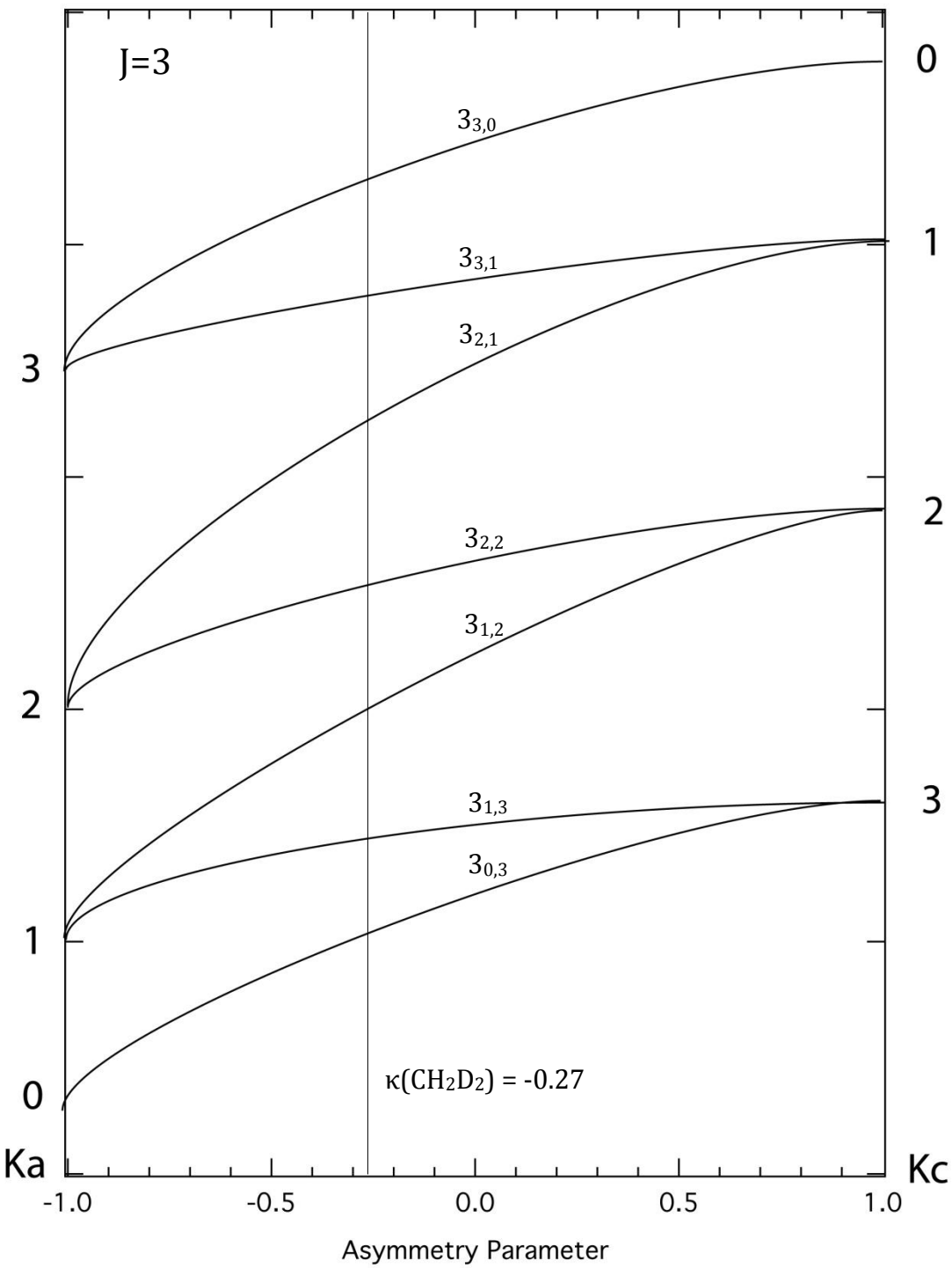

Figure 6.2 Correlation diagram for the asymmetric rotor state energy levels for J ≤ 3

Matrix diagonalization provides the eigenvalues, or energies, for the asymmetric rotor states in the molecule. To calculate infrared transition wavenumbers, we identify the energy eigenvalue for the desired upper state (the eigenvalue of the corresponding state from matrix with coefficients for the vibrationally excited state) and subtract the ground vibrational state wavenumber (eigenvalue of the corresponding state from matrix with coefficients of ground state). Finally, we add the vibrational wavenumber, v_0 (from the reference paper). Doing so allows us to create a table containing the wavenumber all calculated transitions we desire.

Based on the eigenvalues from matrices, we can estimate Boltzmann factors for each eigenstate. The rotational partition function is given by Equation 6.4,

$$N_r = \sum_{0}^{15} g_J \times \exp\left(\frac{-hcE_J}{k_B T_{rot}}\right) \qquad \textbf{Eq. 6.4}$$

where E_J is the energy (eigenvalues of matrixes, in cm^{-1}) and g_J is the statistic weight of each rotational level J. It's given by Equation 6.5[16],

$$g_J = \varepsilon_J \times (2J+1) \qquad \textbf{Eq. 6.5}$$

where ε_J is the total nuclear spin weight. At high temperatures, this statistical weight approaches via Equation 6.6,

$$g_j = (2J+1)^2 \qquad \textbf{Eq. 6.6}$$

However, under the condition of supersonic expansion, where the molecules are cooled to rotational temperature on the order of ten's of degrees, we must account

for the nuclear spin degeneracy in order to calculate accurate rotational populations.

The nuclear spin degeneracy for each rotational level is determined through the symmetry species contained within each level according to Equation 6.7 [17]

$$\varepsilon_J = \sum \varepsilon_\tau n_\tau \qquad \textbf{Eq. 6.7}$$

where n_τ is the number of levels and ε_τ is their nuclear spin weight[3]. The Boltzmann factors for each rotational level up to J=15 are calculated according to Equation 6.8,

$$n_r = g_J \times \exp\left(\frac{-hcE_J}{k_B T_{rot}}\right) \qquad \textbf{Eq. 6.8}$$

where E_J is determined for each level from the eigenvalue of matrix calculations. Table 6.3 shows that the rotational partition function calculated in this work agrees well with with previous published results.[18] We also calculate transition wavenumbers for ν_6 excitation of CH_2D_2, and list transitions originating in the low *J* states in Table 6.4., where primes denote the rotational quantum numbers for the excited vibrational state and *J*, K_a, and K_c denote the rotational levels of v=0. The selection rules for ν_1 and ν_6 transitions are summarized in Table 6.5.

[3] According to ref 16, ε_Γ=15 for symmetric spin and 21 for anti-symmetric spin.

Table 6.3 Comparison of the rotational partition function (Q_r) calculated in current work and published results

Rotational Temperature (K)	**Calculated Q_r**	**Observed Q_r from ref.18**
10	97.35	97.44
20	259.08	259.73
30	466.07	467.26
40	710.09	711.92
50	986.23	988.76
60	1291.10	1294.43
70	1622.25	1626.44
80	1977.75	1982.86
90	2356.03	2362.13
100	2755.81	2762.97

Table 6.4 Calculated frequencies of ν_6 transitions of CH_2D_2

J'	k_a'	k_c'	J	k_a	k_c	Calculated frequency (cm^{-1})
1	1	0	0	0	0	3020.0328
1	1	1	1	0	1	3013.0242
2	1	1	1	0	1	3026.9783
1	0	1	1	1	1	3011.4346
2	2	1	1	1	1	3028.5591
0	0	0	1	1	0	3004.4541
2	0	2	1	1	0	3023.8815
2	2	0	1	1	0	3028.2490
1	1	0	2	0	2	3000.5134
2	1	2	2	0	2	3012.6561
3	1	2	2	0	2	3034.1523
3	3	0	2	0	2	3041.1666
2	0	2	2	1	2	3011.6826
2	2	0	2	1	2	3016.0501
3	2	2	2	1	2	3035.4745
1	0	1	2	1	1	2997.4125
2	2	1	2	1	1	3014.5370
3	0	3	2	1	1	3029.3797
3	2	1	2	1	1	3034.7578
1	1	1	2	2	1	2995.8154
2	1	1	2	2	1	3009.7695
3	1	3	2	2	1	3027.2211
3	3	1	2	2	1	3036.8902
1	1	0	2	2	0	2996.1214
2	1	2	2	2	0	3008.2641
3	1	2	2	2	0	3029.7603
3	3	0	2	2	0	3036.7746

Table 6.5 Selection rules of ν_1 and ν_6 transitions of CH_2D_2 [15, 16]

Vibrations type	Band type	Selection rules on symmetry	Selection rules for the most intense transitions
ν_1	B-type	$e-e \leftrightarrow o-o$ $o-e \leftrightarrow e-o$	$\Delta J = 0, \pm 1; \Delta K_a = \pm 1; \Delta K_c = \pm 1;$
ν_6	C-type	$e-e \leftrightarrow o-e$ $e-o \leftrightarrow o-o$	$K_c = 0 : \Delta J = \pm 1; \Delta K_a = \pm 1; \Delta K_c = 0;$ $K_c \neq 0 : \Delta J = 0, \pm 1; \Delta K_a = \pm 1; \Delta K_c = 0;$

Section 6.3 - Experimental details

6.3.1 Experimental Setup

Our goal is to explore the role that the vibrational symmetry of a C-H stretching vibration plays in activating CH_2D_2 dissociation on Ni(111). With this goal, we perform state-resolved chemisorption measurements with CH_2D_2 prepared in the ν_1 (symmetric stretch) and ν_6 (anti-symmetric stretch) states. The experimental apparatus has been introduced in Chapter II and elsewhere.[19] The UHV chamber contained standard surface-science instruments including a quadruple mass spectrometer for time-of-flight beam characterization and temperature programmed desorption (TPD) detection, Auger electron spectroscopy and argon ion sputtering for surface characterization and cleaning. Radiative heating provided better than ± 1 K control over the surface temperature. The Ni(111) surface is cleaned and preloaded with bulk D atoms prior to CH_2D_2 doses as described in Section 2.6. Surface D atoms are removed by the CIRD process with an energetic Xe/He beam. After surface preparation, 1.3% of CH_2D_2 seeded in He (99.99% CH_2D_2 gas from Cambridge Isotope Laboratories, Inc) expanded continuously and supersonically through a temperature-controlled nozzle and into a high vacuum chamber. The triply differentially pumped beam impinged on the Ni(111) crystal housed in an ultra-high vacuum (UHV) chamber.The surface temperature during CH_2D_2 dosing is kept as 95 K. At that temperature, the nascent methyl group and H/D atoms from CH_2D_2 dissociation can stay on the surface without decomposition

for post-dose detection. Reactivity is measured in the limit of low surface coverage (<0.05ML), so site-blocking effects are negligible.

As mentioned earlier, our state-resolved reactivity measurements provide precise control over reagent energy. Laser excitation prepares gas-phase CH_2D_2 in a single rotational and vibrational quantum state with precisely defined internal energy. The narrow E_{trans} distribution ($\Delta E_{trans}/E_{trans} < 5\%$) in molecular beam, which was verified by time-of-flight measurements (see Section 6.3.2), provided a tight control over translational energy. Direct infrared absorption measurements of molecules in the beam showed that rotational cooling was nearly complete for nozzle temperatures below 550 K. Frequency-stabilized infrared (IR) light from a continuous wave, narrow band laser intersected the molecular beam and excited CH_2D_2 to a single internal quantum state, J = 2 of the ν_1 or ν_6 vibration, via the P(1) transition at 2868.7 or 3013.4 cm^{-1}, respectively. In order to minimize the potential for error resulting from different thermal populations in the v=0 rotational level, the two transitions we chose originated in the same rotational level of the v=0 state. The PED translated into the molecular beam quantified IR absorption for both room temperature and heated nozzle expansions. Long IR radiative lifetimes ensured that CH_2D_2 prepared in the selected rovibrational eigenstate impinged on the Ni(111) surface in its initially prepared state.

We measured reaction probability with ($S_0^{LaserOn}$) and without ($S_0^{LaserOff}$) laser excitation by exposing a beam of known flux to the surface for a fixed time. Then we quantitatively probed the surface bound fragments from CH_2D_2 dissociation using our bulk D titration method and TPD as introduced in Chapter II and elsewhere.[19] We monitored six components (m/z=19, 18, 17, 16, 15 and 4) during the TPD process while the surface is heated at a rate of 2 K/s. The monolayer (ML) coverage of carbon on the surface was calibrated in the following way. We first measured a saturation curve for CH_4 doses as shown in Figure 6.3. The curve is made by a series of bulk H titration experiments with different dosing time of 5% CH_4 seeded in He at T_N = 625K. The yield of titration products begins to saturate at long dose time, and we use that saturation coverage to calibrate the integrated area of the methane TPD feature. This procedure parallels that outlined by Killelea et al., who correlated AES and bulk H titration measurements to establish the saturation coverage for this system.

The calibration experiment produces solely CH_3 radicals. Titration with bulk H forms CH_4 (m/z=16), so 100% of the reaction products desorb as CH_4, whose MS cracking pattern appears in Table 6.6 The product for CH_2D_2 dissociation following C-H bond cleavage and D atom titration is CHD_3 (m/z=19). We account for the different MS cracking patterns of CH_4 and CHD_3 using the experimentally measured cracking patterns for our MS and tabulated in Table 6.6. These cracking patterns were measured by leaking the select gas into the chamber via a leak valve and then

analyzed by MS. In this way, we relate the integrated counts of the CHD_3 TPD peak to the relative number on the CH_4 saturation curve which has a saturation coverage of 0.25 ML on Ni(111) at 95 K.[20]

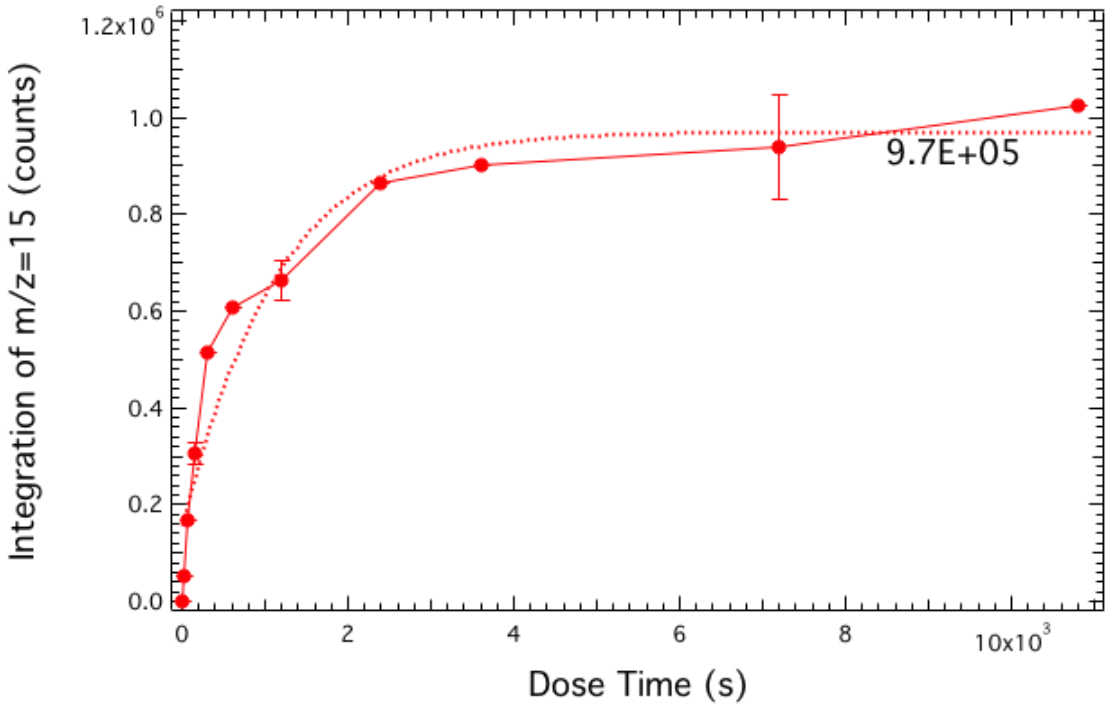

Figure 6.3 Carbon saturation curve from CH_4 doses (5% CH_4/He, T_N = 625K)

Table 6.6 Cracking patterns for CHD_3, CH_2D_2 and CH_4

m/z	CHD_3		CH_2D_2		CH_4		
	Abs %	**Relative %**	**Abs %**	**Relative %**	**Abs %**	**Relative %**	**From ref[21]**
12	<1	0	<1	0	1.1	2.3	2.1
13	<1	0	<1	0	3.3	6.9	7.7
14	<1	0	<1	0	8.0	16.7	16.0
15	3.3	7.2	5.5	11.8	39.8	83.3	84.0
16	6.3	13.9	16.4	34.9	47.8	100.0	100.0
17	25.3	55.6	30.9	65.7	N/A	N/A	N/A
18	19.6	43.0	47.1	100.0	N/A	N/A	N/A
19	45.5	100.0	N/A	N/A	N/A	N/A	N/A

6.3.2 Time-of-flight Measurements

We use TOF to characterize the distribution of velocities in our supersonic molecular beam and precisely measure E_{trans} for sticking curves.[21] The path length is 50.0 cm for molecules flying in a straight line from chopper wheel, which spun at 300Hz, to the QMS ionizer. A multichannel scaler with 2 μs dwell time records TOF spectra (1500 channels per single scan, and 20,000 added scans). We use the SBVH for our TOF experiments since it limits the beam size to fit entirely into the QMS ionizer. To extract the average velocity and velocity spread in the molecular beam, we use a non-linear least-squares fitting to the TOF data, which has the correct form for a velocity distribution from a supersonic expansion and corrections for electronic delays. TOF measurements made with and without a chamber extension provide arrival times for two different flight distances. The difference in arrival times for the two flight path lengths provide a measure of beam velocity that is independent of electronic delay. We use these results to establish the velocity distribution for a particular expansion. We then verify that the electronic delay we use to correct for the delay between our start pulse and the time at which the center of the chopper slot passes through the center of the beam allows us to obtain self-consistent tof characterizations when measuring arrival times with our mass spec in its usual position. We find that a 15.0 μs delay applied to the measurements described here. Figure 6.4 shows TOF spectra for all nozzle temperatures used in this project, and Table 6.7 summarizes E_{trans} calculated from these TOF measurements.

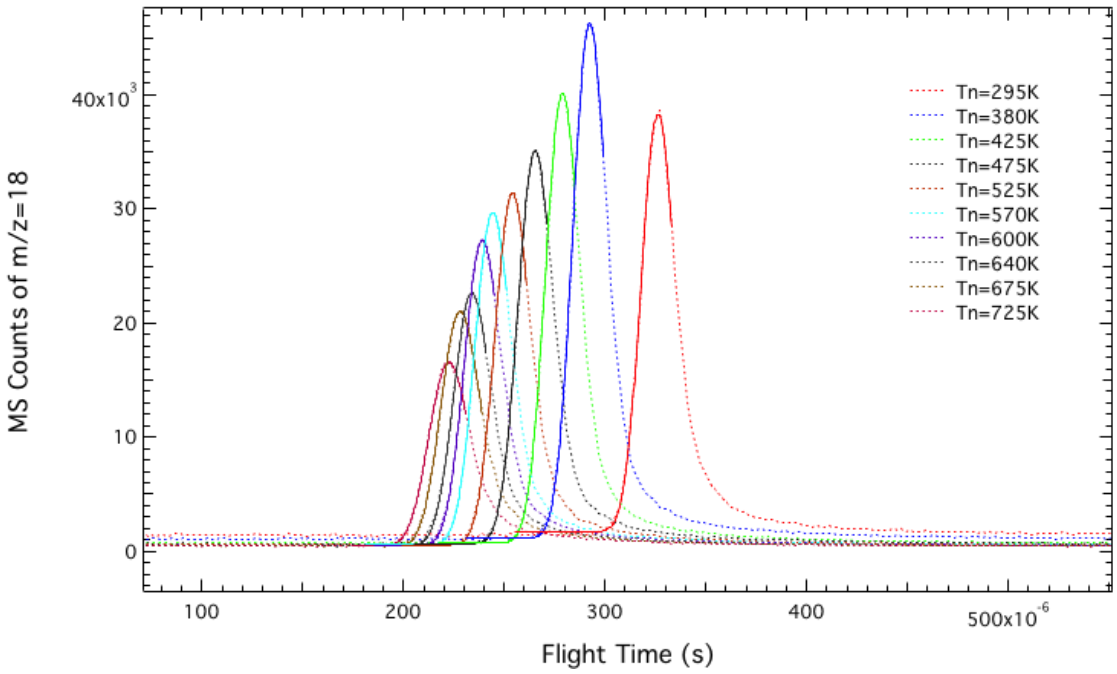

Figue 6.4 TOF spectra for 1.3% CH_2D_2 / He beams at different nozzle temperatures

Table 6.7 E_{trans} from TOF measurements

Gas Mixture	T_N (K)	Speed (m/s)	E_{trans} (kJ/mol)
1.3% CH_2D_2/He	293	1710	26.3
1.3% CH_2D_2/He	380	1934	33.6
1.3% CH_2D_2/He	425	2039	37.4
1.3% CH_2D_2/He	475	2158	41.9
1.3% CH_2D_2/He	525	2267	46.2
1.3% CH_2D_2/He	570	2371	50.6
1.3% CH_2D_2/He	600	2430	53.1
1.3% CH_2D_2/He	640	2490	55.8
1.3% CH_2D_2/He	675	2562	59.1
1.3% CH_2D_2/He	725	2635	62.5

6.3.4 Laser Excitation of CH_2D_2

The transition we used for ν_1 and ν_6 excitation of CH_2D_2 has been summarized in Table 6.8. In order to compare state-resolved reactivity from the two excitations, ν_1 and ν_6, we have to prove they have same spatial deposition profile following laser excitation, which means the excitation must be uniform and the same-size in both excitations.[4] We use multiple doses with different SBVH positions to verify the excitation profile in the molecular beam. The SBVH allows a dosing area of 6.6 mm^2 on crystal, and our normal dosing area with MBVH is 38.5 mm^2 on crystal. We choose three different positions for the SBVH within the diameter of MBVH and check their laser-on carbon coverage with O_2 titrations. If doses with all three SBVH positions produced same results at certain excitation, then excitation is uniform and both excitations have the same profile. The diagram is shown in Figure 6.5 and we show the isothermal desorption of CO obtained during O_2 titrations in Figure 6.6. As we expected, the laser profile is uniform for both ν_1 and ν_6 excitations.

It is always important to measure f_{exc} in state-resolved reactivity measurements. For CH_2D_2, there is no completed database available to use in order to find all possible transitions. We select ν_1 and ν_6 transitions with a same initial state, which provides the identical f_{pop} for both f_{exc}. Thus, we can use f_2, which can be measured by laser saturation experiments[5], instead of f_{exc} in comparison of ν_1 and ν_6 reactivities based

[4] Refer to Section 5.2.3

[5] Refer to Section 4.3

on the definition of f_{exc}[6]. We calculated state-resolved reactivities of CH_2D_2 in Figure 6.9 by Equation 6.9.

$$S_0^{v_i} = \frac{S_0^{LaserOn} - S_0^{LaserOff}}{f_{sat}} \qquad \textbf{Eq. 6.9}$$

where f_{sat} is the ratio of maximum PED value observed and the asymptote from laser saturation curve at current beam condition as shown in Figure 6.7.

For the state-resolved reactivity comparison between CH_2D_2 and CH_4, we couldn't simplify the f_{exc}. In order to find the absolute f_{exc}, we need to find the population fraction of desired initial state under select nozzle temperature, f_{pop}. Here, we use thermal distribution to estimate f_{pop} by the Boltzmann factor of the desired initial state. As mentioned in Section 5.2.4, the rotational temperature can be estimated by an empirical relationship of $T_{rot}/T_N \approx 0.0265$.[22] For example, calculated Boltzmann factors for rovibrational states with $J \leq 5$ at T_{rot} = 15K are shown in Table 6.9. The symmetry factor ($f_{symmetry}$) in the table is given by Equation 6.10.

$$f_{symmetry} = (-1)^{K_c} \qquad \textbf{Eq. 6.10}$$

We then calculate the population fraction of Boltzmann factor of the select initial state, which gives f_{pop}, via Equation 6.4 to Equation 6.8. Therefore, we can calculate the absolute f_{exc} by Equation 5.2, where f_2 is from with laser saturation curve measurements as introduced in Section 4.3 as well as Section 5.2.4. We summarize the f_{exc} and $S_0^{v_6}$ for different beam conditions in Table 6.10.

[6] See Equation 5.2

Table 6.8 ν_1 and ν_6 transitions used in CH_2D_2 excitation

Mode	Description	Transition (cm^{-1})	J'_{KaKc}	J_{KaKc}	Symmetry
ν_1	CH_2 Symmetric stretching	2974.21	1_{01}	1_{10}	A_1
ν_6	CH_2 Anti-symmetric stretching	3023.88	2_{02}	1_{10}	B_1

Table 6.9 Thermal statistics of CH_2D_2 rovibration states ($J \leq 4$) at T_{rot} =15 K

J	K_a	K_c	$f_{symmetry}$[7]	ε_J	g_j	n_j	f_{pop}
0	0	0	1	15	15	1.50E+01	8.65E-02
1	0	1	-1	21	63	3.37E+01	1.94E-01
1	1	1	-1	21	63	3.12E+01	1.80E-01
1	1	0	1	15	45	2.14E+01	1.23E-01
2	0	2	1	15	75	1.16E+01	6.71E-02
2	1	2	1	15	75	1.11E+01	6.40E-02
2	1	1	-1	21	105	1.36E+01	7.87E-02
2	2	1	-1	21	105	1.09E+01	6.26E-02
2	2	0	1	15	75	7.65E+00	4.41E-02
3	0	3	-1	21	147	3.67E+00	2.11E-02
3	1	3	-1	21	147	3.59E+00	2.07E-02
3	1	2	1	15	105	1.98E+00	1.14E-02
3	2	2	1	15	105	1.66E+00	9.59E-03
3	2	1	-1	21	147	2.19E+00	1.26E-02
3	3	1	-1	21	147	1.42E+00	8.17E-03
3	3	0	1	15	105	1.01E+00	5.82E-03
4	0	4	1	15	135	3.03E-01	1.75E-03
4	1	4	1	15	135	3.01E-01	1.73E-03
4	1	3	-1	21	189	2.78E-01	1.60E-03
4	2	3	-1	21	189	2.48E-01	1.43E-03
4	2	2	1	15	135	1.51E-01	8.73E-04
4	3	2	1	15	135	1.04E-01	6.02E-04
4	3	1	-1	21	189	1.43E-01	8.26E-04
4	4	1	-1	21	189	7.51E-02	4.33E-04
4	4	0	1	15	135	5.36E-02	3.09E-04

[7] -1 represents for anti-symmetric, and 1 represents for symmetric

Table 6.10 Estimated f_{exc} of CH_2D_2 anti-symmetric stretch (ν_6)

Beam	$\mathbf{T_N}$	$\mathbf{T_{rot}}$	f_{pop}	f_{sat}	f_{exc}	$S_0^{\nu_6}$
1.3% CH_2D_2/He	380	26.6	0.150	0.745	0.112	1.15E-5±3.10E-6
1.3% CH_2D_2/He	425	32.3	0.144	0.723	0.104	4.76E-5±1.54E-5
1.3% CH_2D_2/He	475	36.1	0.137	0.599	0.082	1.54E-4±4.10E-5
1.3% CH_2D_2/He	525	39.9	0.130	0.481	0.063	4.61E-4±1.65E-4
1.3% CH_2D_2/He	570	43.3	0.123	0.384	0.047	1.04E-3±4.40E-4
1.3% CH_2D_2/He	725	55.1	0.102	0.372	0.038	2.50E-3±8.90E-4

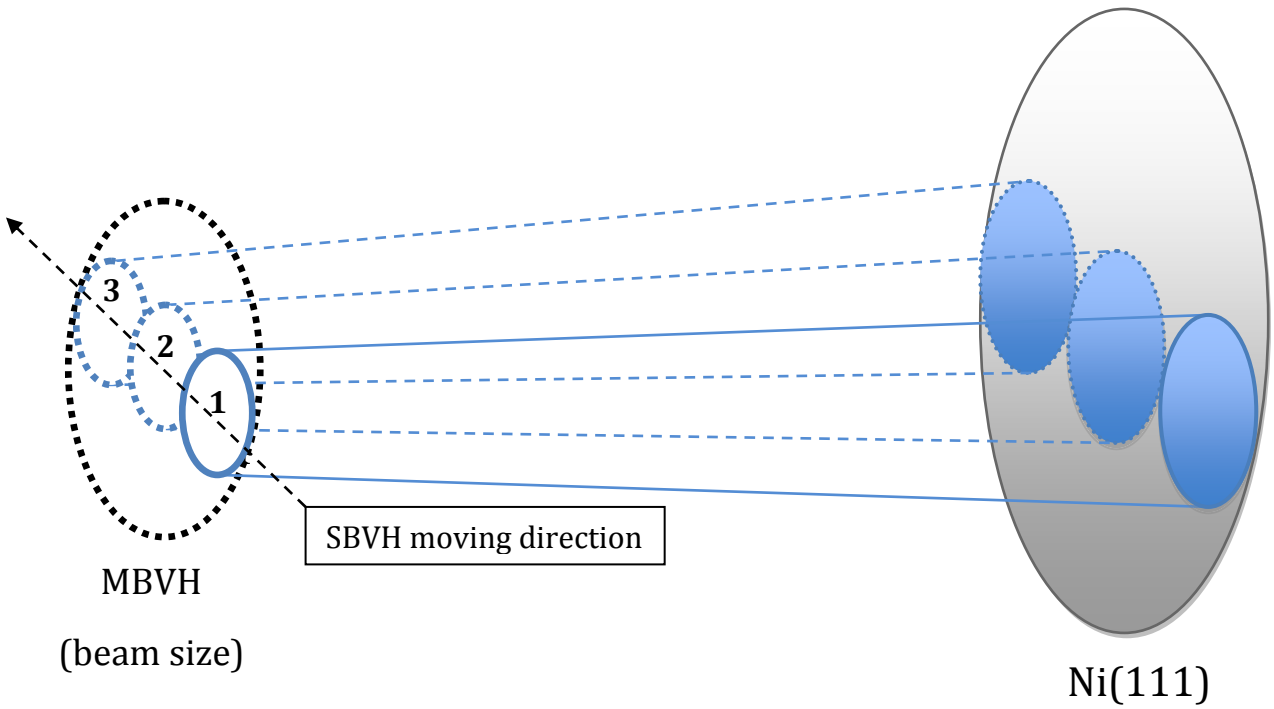

Figure 6.5 Diagram of SBVH doses at different position. Blue areas represent the dosing area through SBVH. We use MBVH in our state-resolved measurements, so it represents the size of molecular beam. Position 1 represents 0.36" on the scale of the 1-D manipulator that positions the sliding beam valve, 2 for 0.41", and 3 for 0.46".

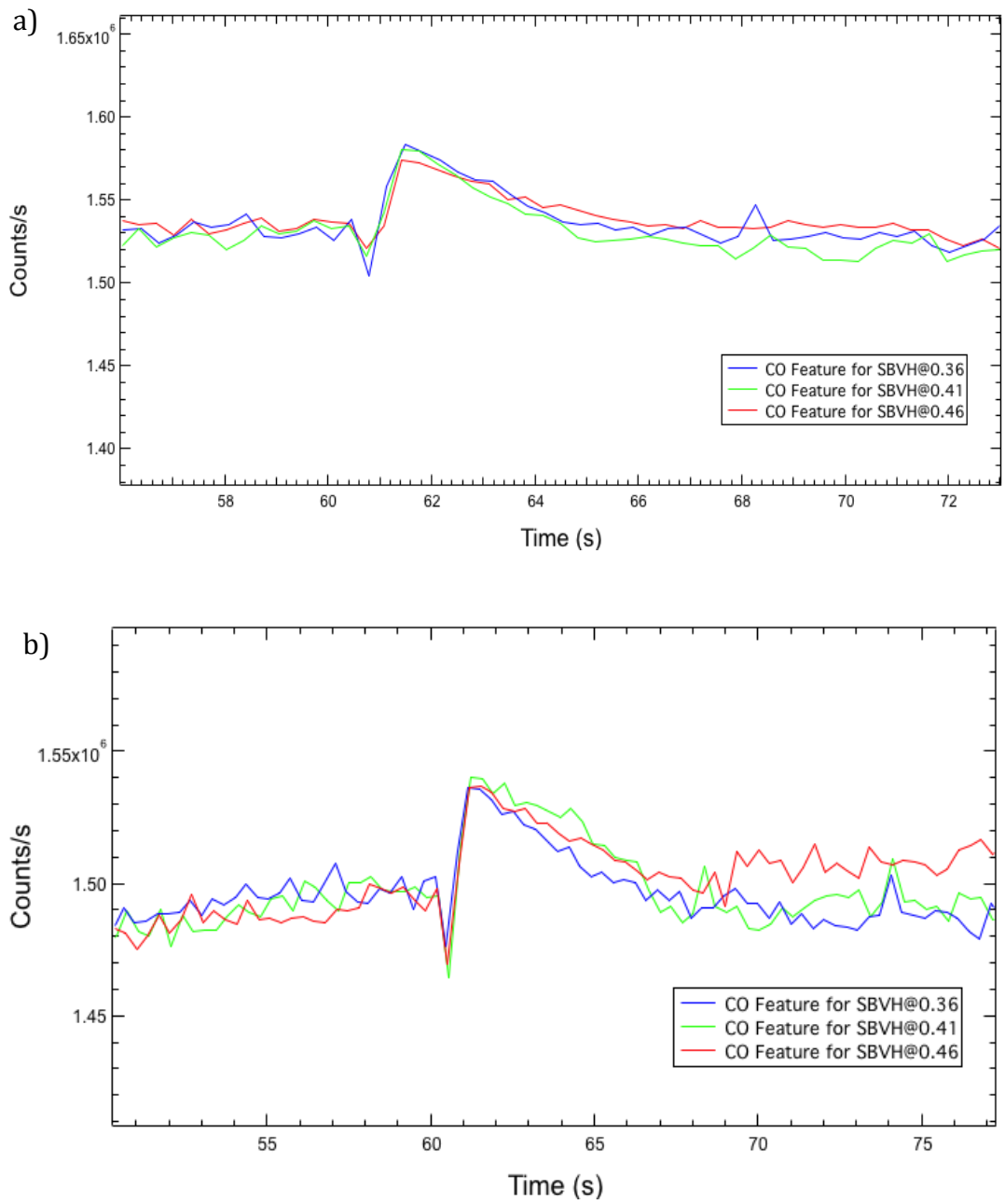

Figure 6.6 O_2 titration spectra for 1.3% CH_2D_2/He at T_N = 570 K, T_S = 550 K, and t = 1200 sec: a) ν_1 excited CH_2D_2 with different SBVH positions; b) ν_6 excited CH_2D_2 with different SBVH positions.

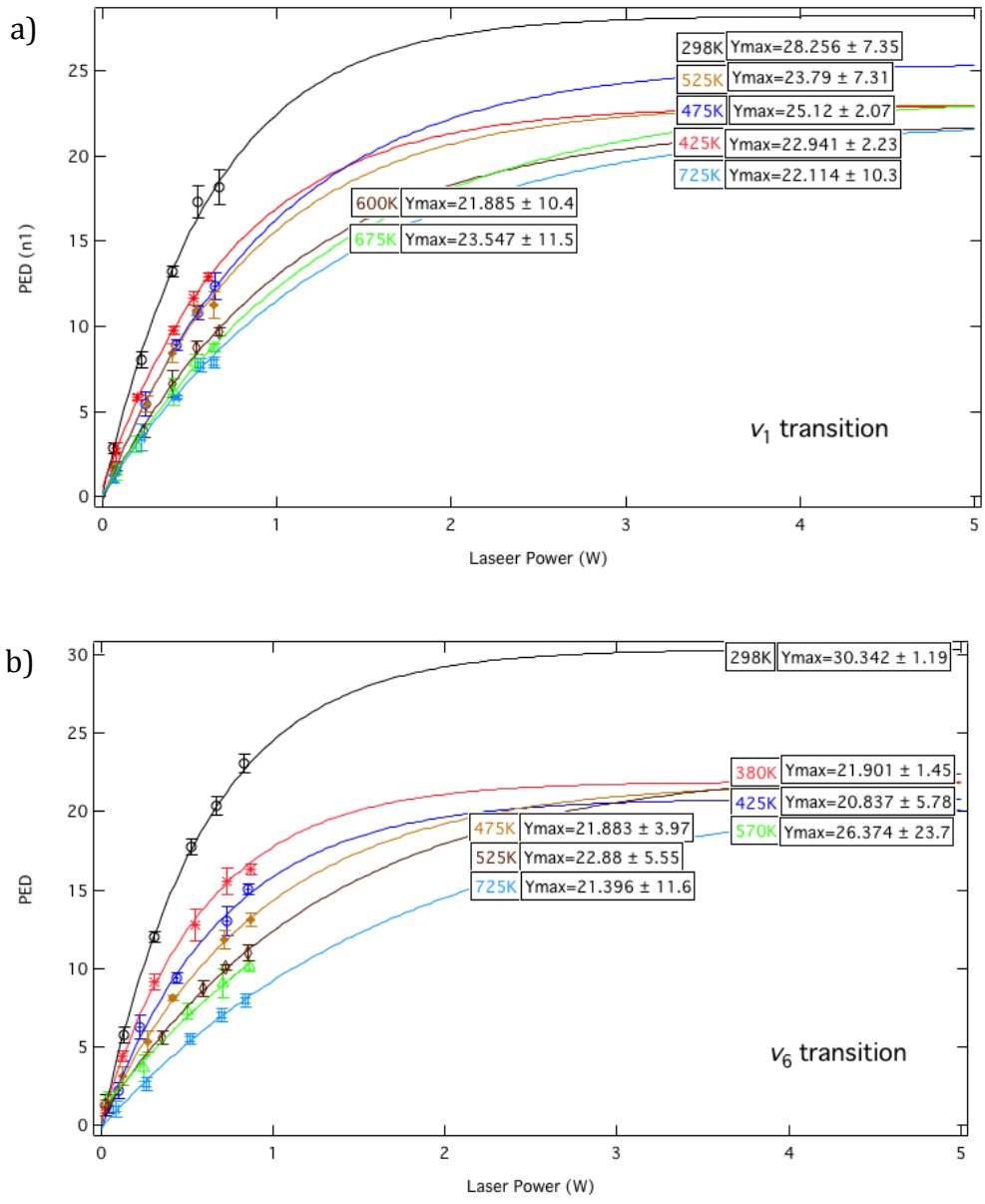

Figure 6.7 Laser saturation curves at different T_N for

a) ν_1 excitation at 2974.21 cm^{-1}; b) ν_6 excitation at 3023.88 cm^{-1}.

Section 6.4 - Results and Discussion

Our measurements of the sticking probability with and without laser excitation allow us to calculate a state-resolved reactivity for the particular laser-excited state ν_1 or ν_6. Equation 6.12 relates the state-resolved reactivity (S_0^V), to the reactivity with laser excitation ($S_0^{Laserow}$), without laser laser excitation ($S_0^{Laseroff}$), the fraction of molecules excited (f_{exc}), which we measure directly, and the vibrational ground state reactivity ($S_0^{V=0}$) [13, 23]

$$S_0^V = \frac{S_0^{Laseron} - S_0^{Laseroff}}{f_{exc}} + S_0^{V=0} \qquad \textbf{Eq. 6.12}$$

When E_{trans} and T_s are relatively low, $S_0^{V=0}$ contributes negligibly to S_0^V and can be neglected. $S_0^{Laseroff}$ is an upper limit on $S_0^{V=0}$, so when it is much smaller than $S_0^{Laserow}$, it can be neglected too.

Our bulk D titrations show a strong bond selectivity for CH_2D_2 dissociation with either ν_1 or ν_6 C-H excitations. The integrated product yield for C-H and C-D bond cleavage channels is more than 20:1 as shown in Figure 6.8. The preference for C-H cleavage following excitation of a C-H stretching vibration is also shown in CH_2D_2 dissociation on Ni(100)[12] and CHD_3 dissociation on Ni(111)[19]. In both cases, the exclusive cleavage of C-H bond is believed due to the localized quanta on C-H bond and lack of IVR during the reaction time scale. The similar bond selectivity in the dissociation of v=1 excited CH_2D_2 on Ni(111) suggested the single quanta

vibrational energy is also localized on C-H bond and no IVR happened at the initial of process. This bond-selectivity also suggests ν_1 or ν_6 C-H excitation is weakly or non-coupled with other modes in CH_2D_2. We summarized all sticking probabilities measured for both ν_1 and ν_6 excitations in Table 6.9 and plotted S_0 vs. E_{trans} in Figure 6.9. From Figure 6.9 we can find that the selective dissociation probability for the symmetric stretch vibration (ν_1) and anti-symmetric stretch vibration (ν_6) are identical within experimental error.

This result is somewhat unexpected. Reports of state-resolved reactivities for the symmetric (ν_1) and anti-symmetric C-H stretching states (ν_3) of CH_4 on Ni(100) show ν_1 to be significantly more reactive than the ν_3 state.[13, 14] These results were interpreted as being consistent with a vibrationally adiabatic picture[24] where the symmetric C-H stretching state, being the lowest frequency C-H stretch in the gas phase, has preferential access to the softened C-H bond that participates in reaction. In this model, the triply degenerate ν_3 state correlates adiabatically with excitation in the methyl fragment. In the experiments described here, the ν_1 state would once again be expected to be more reactive within this adiabatic model, but we find that its reactivity is identical to that of the antisymmetric ν_6 C-H stretching state.

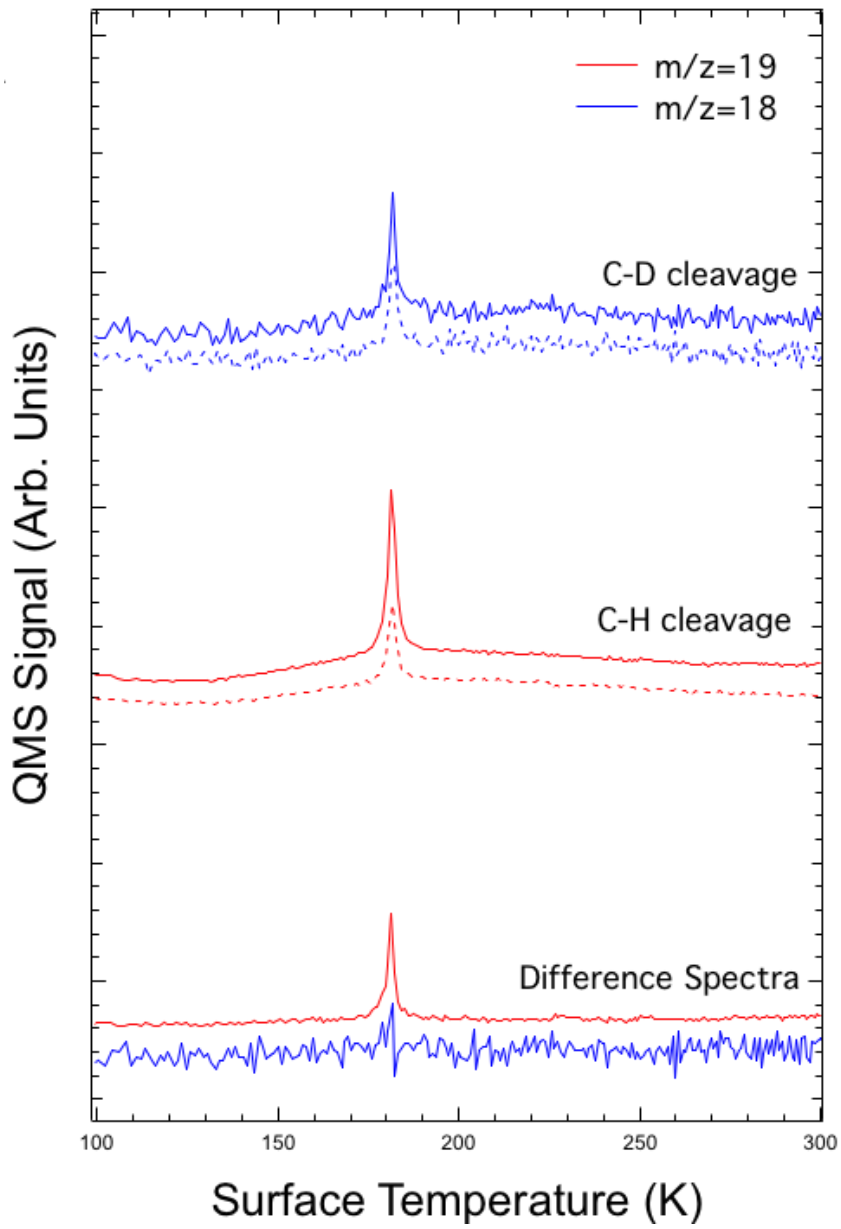

Figure 6.8 Bond selectivity of CH_2D_2 dissociation on Ni(111) with laser excitation

For CH_4 on Ni(100), both studies were performed on 475 K surfaces, which have extensive surface atom motion promoting the reactivity. Our CH_2D_2 doses were performed on 95 K surface, which minimizes the thermal excitation of the surface. In order to better explore the effect of surface temperature, and to obtain an E_{trans} threshold energy for the ν_1 and ν_6 states of CH_2D_2, we performed our experiments at this low temperature. We can compare our results to S_0 data for CH_4 (ν_3) dissociation on a Ni(111) surface at 475 K[25] and at 90 K. In Figure 6.10, we can see the S_0 of CH_4 (ν_3) at 90K surface has an identical sticking probability as our CH_2D_2 in both stretch modes. In addition, the 'turn-off' point, or threshold E_{trans} for reaction where S_0 drops suddenly, is exactly the same for all three excitations. This suggests all three C-H excitations couple similarly to the reaction coordinate and that surface atom motion plays a very important role. The E_{trans} threshold for reaction represents the effective barrier for C-H breaking on a Ni(111) surface with minimal thermal excitation of the surface atoms.

Beck et al. studied the dissociative chemisorption of two overtone (v=2) C-H stretching states of CH_2D_2 on Ni(100. Their results showed that the anti-symmetric overtone stretching state ($2\nu_6$) is more reactive than the combined stretching mode of $\nu_1 + \nu_6$ state. The mechanism is believed to be same as the gas-phase reaction we mentioned in Section 6.1 where Cl reacted with CH_2D_2 in the same two vibrational states. At the v=2 level of excitation (and above), anharmonicity causes the C-H stretching eigenstates to more closely resemble localized bond excitations. The $|20\rangle$

and $|11\rangle$ states differ significantly in their vibrational character, because the $|20\rangle$ state has 2 quanta of C-H stretch localized in a single C-H bond of CH_2D_2, whereas the $|11\rangle$ state as a single quantum of excitation localized in each of the two C-H bond. In both cases, the preference for reactivity is due to a more localized vibration on a single C-H bond. At the v=1 level of excitation, the C-H stretching states more closely resemble normal mode excitations where the vibrational energy is distributed between both bonds for both ν_1 and ν_6, but the two states differ in the relative phase of motion of the two C-H bonds. In both gas-phase and surface studies of C-H stretching states with one quantum of excitation, vibrational symmetry, and its effect on coupling to the reaction coordinate, has been commonly invoked to explain reactivity differences. Since symmetric stretch and anti-symmetric stretch show no difference in promoting reactivity in our measurements, it may suggest that other factors, such as the presence of a transition dipole moment in the ν_6 state, may also play a role. The answer to this question will best be addressed by quantum calculations that accurately identify and assess the role of vibrational coupling in the entrance channel to the reaction, such as those reported by Jackson and Nave for CH_4 dissociation on NI(111).[26]

Table 6.11 State-resolved reactivity of CH_2D_2 dissociation on Ni(111) (T_S = 95K)

Beam	Excitation	T_N (K)	E_{trans} (kJ/mol)	f_{sat}	S_0^{ν} - *relative*
3% CH_2D_2/He	ν_1	450	38.5	0.530	4.28E-6 ± 2.68E-7
3% CH_2D_2/He	ν_1	500	42.7	0.480	1.92E-5 ± 2.70E-6
3% CH_2D_2/He	ν_1	550	47.3	0.470	4.48E-5 ± 1.03E-5
3% CH_2D_2/He	ν_1	600	51.3	0.443	6.86E-5 ± 2.39E-5
1.3% CH_2D_2/He	ν_1	675	61.0	0.371	2.10E-4 ± 4.55E-5
3% CH_2D_2/He	ν_1	725	65.4	0.357	1.78E-4 ± 7.99E-5
1.3% CH_2D_2/He	ν_6	380	34.7	0.745	1.73E-6 ± 4.64E-7
1.3% CH_2D_2/He	ν_6	425	38.3	0.723	6.85E-6 ± 1.16E-6
1.3% CH_2D_2/He	ν_6	475	42.7	0.599	2.10E-5 ± 5.64E-6
1.3% CH_2D_2/He	ν_6	525	47.3	0.481	6.03E-5 ± 2.16E-6
1.3% CH_2D_2/He	ν_6	570	51.3	0.384	1.27E-4 ± 2.72E-5
1.3% CH_2D_2/He	ν_6	725	65.4	0.372	2.55E-4 ± 8.22E-5

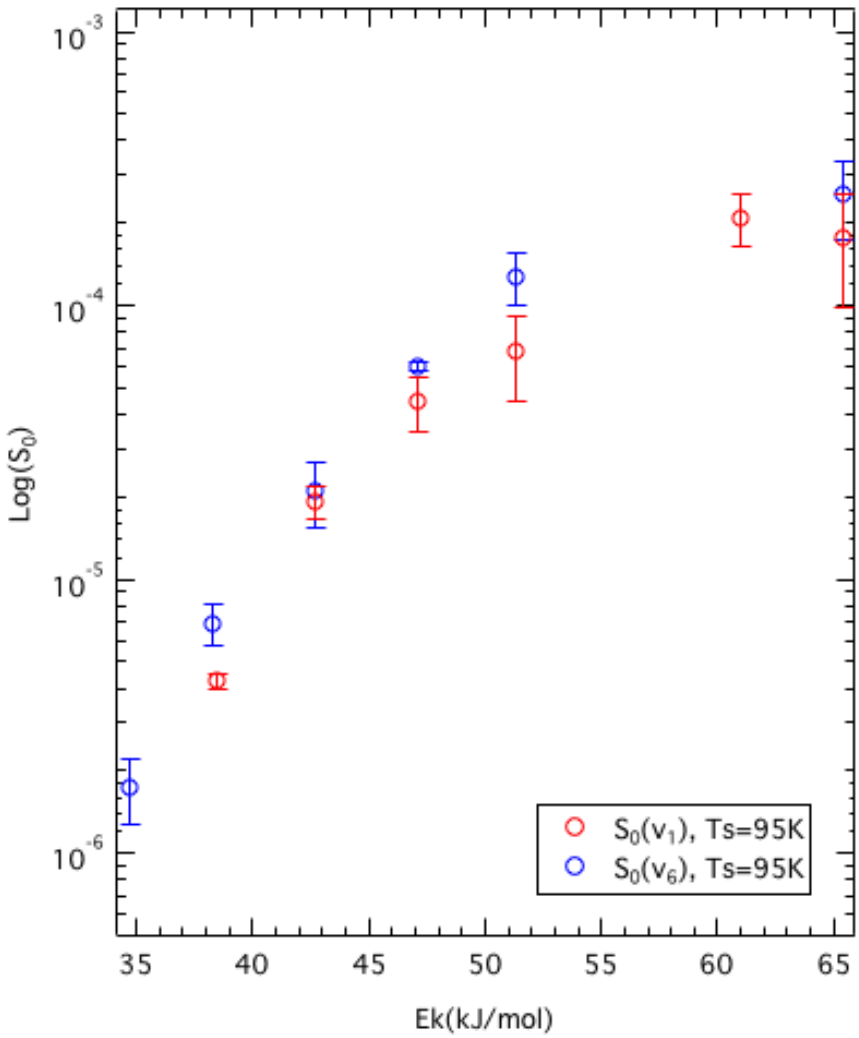

Figure 6.9 S_0 of CH_2D_2 selective dissociation on Ni(111) with ν_1 and ν_6 excitations.

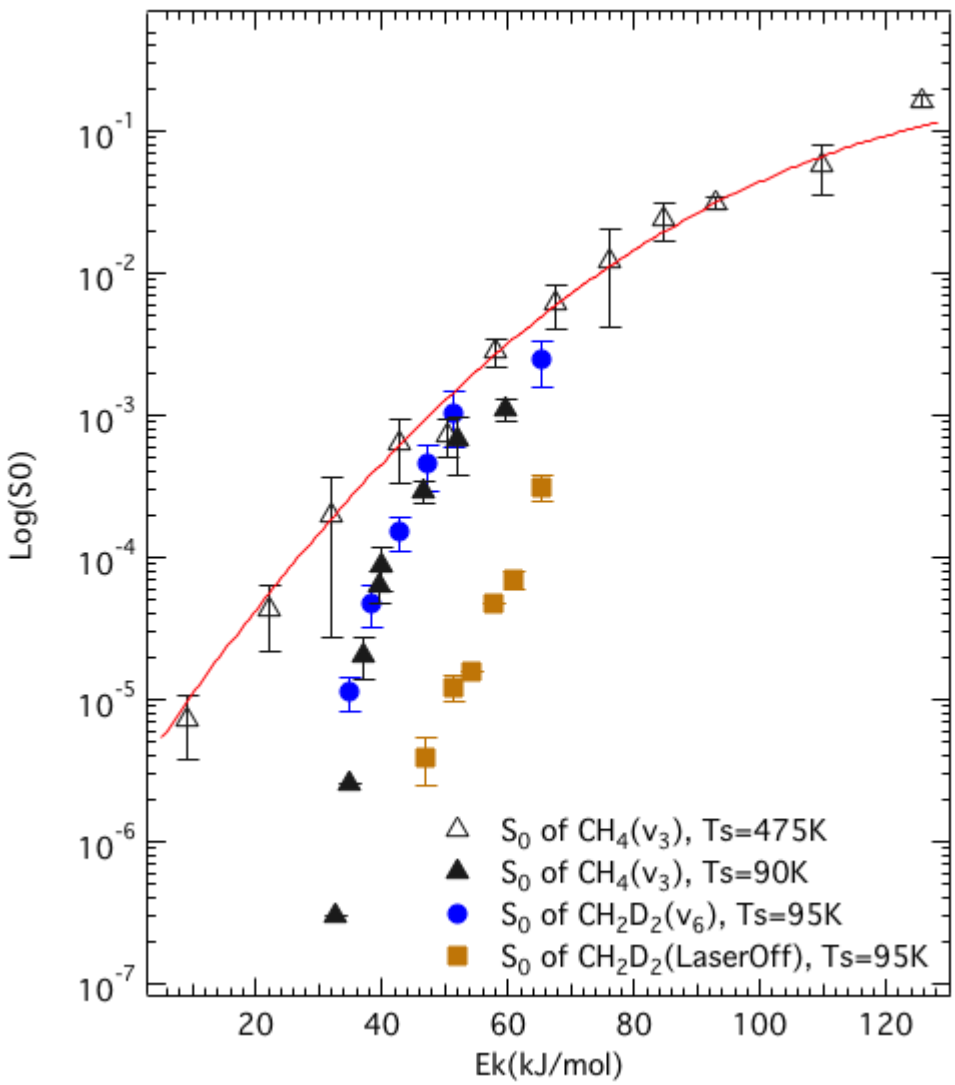

Figure 6.10 Comparison of state-resolved reactivity of CH_2D_2 (ν_6) and CH_4 (ν_3) dissociation on Ni(111) at different surface temperature.[8]

[8] CH_4 data come from ref. 23 and 24.

Section 6.5 – Conclusion and Future Direction

In this chapter, we have demonstrated bond-selective control in a heterogeneous catalytic reaction. We use an IR laser to excite CH_2D_2 molecules to v=1 of the ν_1 symmetric C–H stretching state and ν_6 anti-symmetric C–H stretching state. Excited CH_2D_2 molecules react exclusively by C–H bond cleavage, and almost no enhancement to C–D cleavage, which indicates minimal energy flow between C-H and C-D stretching motion on the reaction timescale. The bond selectivity also suggests the ν_1 and ν_6 C-H excitations of CH_2D_2 are weakly or non-coupled to other modes in the molecule. On the other hand, the bond-selective control also benefits from the short interaction time of a direct gas-surface reaction, which prevents energy 'leaking' out from the molecule with prepared vibrational states.

We compared state-resolved reactivity of CH_2D_2 with two excitations of different symmetry types. Our results show that the surface temperature is a dominant effect to reaction on a low-temperature surface. In such a condition, modes and symmetry effects appear to be minimal. Compared to CH_2D_2 experiments with overtone excitation ν_1 and ν_6 C-H vibrations do behave as normal mode excitations, and have identical efficacies for promoting reaction. The absence of a clear reactivity difference between symmetric and antisymmetric C-H stretching states suggests that vibrational symmetry alone does not explain mode selectivity differences observed for C-H stretching states of methane. However, there is still a long way to make a clear conclusion regarding the role of vibrational symmetry and mode

selectivity. Detailed computational studies and future state-resolved experiments that quantify CH_3D or CHD_3 dissociation on Ni(111) will help advance our understanding of this important problem. With these data and our current CH_2D_2 results, we can uncover more details in symmetry and mode effects.

Reference

1. Killelea, D. R. Bond-Selective Control of a Gas-Surface Reaction. Tufts University, Medford, 2007.

2. Kimel, S.; Speiser, S., LASERS AND CHEMISTRY. *Chemical Reviews* **1977,** *77* (4), 437-472.

3. Sinha, A.; Hsiao, M. C.; Crim, F. F., Bond-Selected Bimolecular Chemistry - H+HOD(4νOH)-->OD+H2. *Journal of Chemical Physics* **1990,** *92* (10), 6333-6335.

4. Crim, F. F., Vibrational state control of bimolecular reactions: Discovering and directing the chemistry. *Accounts of Chemical Research* **1999,** *32* (10), 877-884.

5. Metz, R. B.; Thoemke, J. D.; Pfeiffer, J. M.; Crim, F. F., Selectively Breaking Either Bond in the Bimolecular Reaction of Hod with Hydrogen-Atoms. *Journal of Chemical Physics* **1993,** *99* (3), 1744-1751.

6. Camden, J. P.; Bechtel, H. A.; Brown, D. J. A.; Zare, R. N., Comparing reactions of H and Cl with C-H stretch-excited CHD3. *Journal of Chemical Physics* **2006,** *124* (3).

7. Simpson, W. R.; Rakitzis, T. P.; Kandel, S. A.; Orr-Ewing, A. J.; Zare, R. N., Reaction of Cl With Vibrationally Excited Ch4 and Chd3 - State- to-State Differential Cross-Sections and Steric Effects For the HCl Product. *Journal of Chemical Physics* **1995,** *103* (17), 7313-7335.

8. Yoon, S.; Holiday, R. J.; Crim, F. F., Vibrationally controlled chemistry: Mode- and bond-selected reaction of CH3D with CI. *Journal of Physical Chemistry B* **2005,** *109* (17), 8388-8392.

9. Holiday, R. J.; Kwon, C. H.; Annesley, C. J.; Crim, F. F., Mode- and bond-selective reaction of Cl(P-2(3/2)) with CH3D: C-H stretch overtone excitation near 6000 cm(-1). *Journal of Chemical Physics* **2006,** *125* (13).

10. Kim, Z. H.; Bechtel, H. A.; Camden, J. P.; Zare, R. N., Effect of bending and torsional mode excitation on the reaction Cl+CH4 -> HCl+CH3. *Journal of Chemical Physics* **2005,** *122* (8).

11. Bechtel, H. A.; Kim, Z. H.; Camden, J. P.; Zare, R. N., Bond and mode selectivity in the reaction of atomic chlorine with vibrationally excited CH2D2. *Journal of Chemical Physics* **2004,** *120* (2), 791-799.

12. Beck, R. D.; Maroni, P.; Papageorgopoulos, D. C.; Dang, T. T.; Schmid, M. P.; Rizzo, T. R., Vibrational mode-specific reaction of methane on a nickel surface. *Science* **2003,** *302* (5642), 98-100.

13. Juurlink, L. B. F.; McCabe, P. R.; Smith, R. R.; DiCologero, C. L.; Utz, A. L., Eigenstate-resolved studies of gas-surface reactivity: CH4 (nu(3)) dissociation on Ni(100). *Physical Review Letters* **1999,** *83* (4), 868-871.

14. Maroni, P.; Papageorgopoulos, D. C.; Sacchi, M.; Dang, T. T.; Beck, R. D.; Rizzo, T. R., State-resolved gas-surface reactivity of methane in the symmetric C-H stretch vibration on Ni(100). *Physical Review Letters* **2005,** *94* (24).

15. Deroche, J. C.; Guelachvili, G., HIGH-RESOLUTION INFRARED-SPECTRUM OF CH2D2 - V1 AND V6 FUNDAMENTAL BANDS NEAR 3000 CM-1. *Journal of Molecular Spectroscopy* **1975,** *56* (1), 76-87.

16. Herzberg, G., *Molecular Spectra and Molecular Structure II: Infrared and Raman Spectra of Polyatomic Molecules*. Van Nostrand Reinhold: New York, 1945.

17. McDowell, R. S., Rotational Partition-Functions for Sperical-Top Molecules. *J. Quant. SPectrosc. Radiat. Transf.* **1987,** *38* (5), 337.

18. Robiette, A. G.; Dangnhu, M., ROTATIONAL PARTITION-FUNCTIONS OF METHANE AND ITS ISOTOPIC-SPECIES. *Journal of Quantitative Spectroscopy & Radiative Transfer* **1979,** *22* (5), 499-501.

19. Killelea, D. R.; Campbell, V. L.; Shuman, N. S.; Utz, A. L., Bond-selective control of a heterogeneously catalyzed reaction. *Science* **2008,** *319* (5864), 790-793.

20. Killelea, D. R.; Campbell, V. L.; Shuman, N. S.; Smith, R. R.; Utz, A. L., Surface Temperature Dependence of Methane Activation on Ni(111). *Journal of Physical Chemistry C* **2009,** *113* (48), 20618-20622.

21. Juurlink, L. B. F. Eigenstate-Resolved Measurements of Methane Dissociation on Ni(100). Tufts University, Medford, 2000.

22. Smith, R. R. Rovibrational State-Resolved Studies of Methane Dissociation on Ni(111). Tufts University, Medford, 2003.

23. Juurlink, L. B. F.; Killelea, D. R.; Utz, A. L., State-resolved probes of methane dissociation dynamics. *Progress in Surface Science* **2009,** *84* (3-4), 69-134.

24. Halonen, L.; Bernasek, S. L.; Nesbitt, D. J., Reactivity of vibrationally excited methane on nickel surfaces. *Journal of Chemical Physics* **2001,** *115* (12), 5611-5619.

25. Smith, R. R.; Killelea, D. R.; DelSesto, D. F.; Utz, A. L., Preference for vibrational over translational energy in a gas-surface reaction. *Science* **2004,** *304* (5673), 992-995.

26. Jackson, B.; Nave, S., The dissociative chemisorption of methane on Ni(100): Reaction path description of mode-selective chemistry. *Journal of Chemical Physics* **2011,** *135* (11).

Appendix I - Igor Pro Function for Squarewave Fitting of K&W Modulation

```
Function Modulation (w,x)
Wave w; variable x
Variable datapoint,xvalue, gatevalue
Wave model = GateWave
xvalue = x2pnt(model,x)
if (model[xvalue]<-0.05)
                gatevalue = 1
        else
                gatevalue = 0
        endif
 datapoint = w[0] + (w[1]*x) + (w[2]*gatevalue)
 return datapoint
 End

| Variables:
| w_0: Y value at the starting cursor
| w_1: Time constant
| w_2: Modulation height
```